Spring 2021

Nickel – Iron Catalysts for Low Temperature Dry Reforming of Methane

Gagandeep Dhillon
University of New Hampshire, Durham

Follow this and additional works at: https://scholars.unh.edu/dissertation

Nickel – Iron Catalysts for Low Temperature Dry Reforming of Methane

By

Gagandeep Singh Dhillon

B.E. Chemical Engineering, M.S. University of Baroda, India, 2016

M.S. Chemical Engineering, University of New Hampshire, Durham, USA, 2018

DISSERTATION

Submitted to the University of New Hampshire

in Partial Fulfillment of

the Requirements for the Degree of

Doctor of Philosophy

in

Chemical Engineering

May, 2021

This dissertation has been examined and approved in partial fulfillment of the requirements for

the degree of Doctor of Philosophy in Chemical Engineering by:

Disseratation director: Dr. Nan Yi, Assistant Professor of Chemical Engineering

Dr. P.T. Vasudevan, Professor of Chemical Engineering

Dr. Xiaowei Teng, Professor and Chair of Chemical Engineering

Dr. Nivedita Gupta, Professor of Chemical Engineering

Dr. Gonghu Li, Professor of Chemistry

On March 24th 2021

Approval signatures are on file with the University of New Hampshire Graduate School.

Dedication

I dedicate my PhD dissertation to my respected mother.

Acknowledgements

First of all, I bow and thank to my "Celestial Lord God" for blessing with lot of opportunities and help he has given me. I would like to express my profound appreciation and gratitude to Dr. Nan Yi, who has provided me guidance and support over the past 3 years as my PhD advisor. Sincere thanks to the UNH Graduate School and the Department of Chemical Engineering for providing financial support through teaching assistantship and Summer Teaching Assistant Fellowship (STAF) during my PhD program. I would like to thank Dr. P.T. Vasudevan, Dr. Russell Carr and Dr. Nivedita Gupta for their constant mentoring and motivation throughout my grad school journey at the University of New Hampshire.

I would also like to thank my other dissertation committee members – Dr. Xiaowei Teng and Dr. Gonghu Li for their major contributions in teaching catalysis coursework. I would like to thank my colleagues Guoquiang Cao, Zhen Tian and other members from Yi's Lab for their assistance. I sincerely appreciate help from University Instrumentation Center – Mr. John Wildermann for his help on XPS analysis. I would like to sincerely appreciate Darcy Fournier for her constant help and support in operating and troubleshooting instruments.

Lastly, I would again like to acknowledge my respected parents and sister for always showering their blessings and constant mental support to me. Once again, thanks to everyone.

TABLE OF CONTENTS

LIST OF FIGURES

ABSTRACT

Dry reforming of methane (DRM) offers benefit of consuming two important greenhouse gases (CH_4 and CO_2) in a single reaction to produce syngas. Ni-based catalysts have been studied for DRM. However, monometallic Ni catalysts deactivate mainly because of coking. We were motivated to include earth-abundant promoter metals to suppress coke formation and studied a series of bimetallic nickel-iron catalysts supported over TiO_2 and TiO_2-CeO_2 at 550˚C and atmospheric pressure. This dissertation mainly focuses on various approaches to synthesize Ni-Fe catalysts and examines the effect of oxide support modification over optimum Ni-Fe/TiO_2 catalyst. In this context, Ni-Fe catalysts supported over TiO_2 were prepared by mainly two approaches – incipient wetness impregnation and co-precipitation methods. The total metal loading of Ni+Fe was maintained at 10 wt% while different ratios of Ni/Fe were investigated. We further explored the effect of oxide support modification by substituting 20 wt% TiO_2 with CeO_2 over a Ni-Fe/TiO_2 catalyst showing high activity and simultaneous minimum coke formation. Bimetallic Ni-Fe catalysts were characterized by various techniques including Temperature Programmed Reactions (TPRs), X-ray Photoelectron Spectroscopy (XPS), Thermogravimetry Analysis-Differential Thermogravimetry (TGA-DTG), Raman Spectroscopy and *In-situ* DRIFTS analysis. Conclusively, we found that addition of Fe is beneficial to inhibit coke deposition owing to its redox properties during low temperature DRM, while addition of CeO_2 adds to coke inhibition property of Ni-Fe/TiO_2 catalysts. However, Ni/Fe ratio of 3:1 is essential for better activity performance and simultaneous resistance to coke formation.

Chapter 1

Introduction

1.1 Sources of Methane

Fossil fuels contribute to majority of the energy needs across the globe [1] because fossil fuels could be utilized directly or indirectly for energy generation and chemicals production. Fossil fuels would continue to satisfy energy demands for next 3–4 decades [2]. Meanwhile depletion of fossil fuels urges the need to investigate alternative to it. Natural gas, as one major component of fossil fuels, could be utilized to synthesize fossil fuel derivatives and chemicals through variety of conversion processes [3,4]. As shown in Fig. 1.1, the US Energy Information Administration (EIA) has disclosed an approximate 850 trillion cubic feet of proven natural gas reserves while 504 trillion cubic feet of natural gas has been estimated to be recoverable stock in the United States [5].
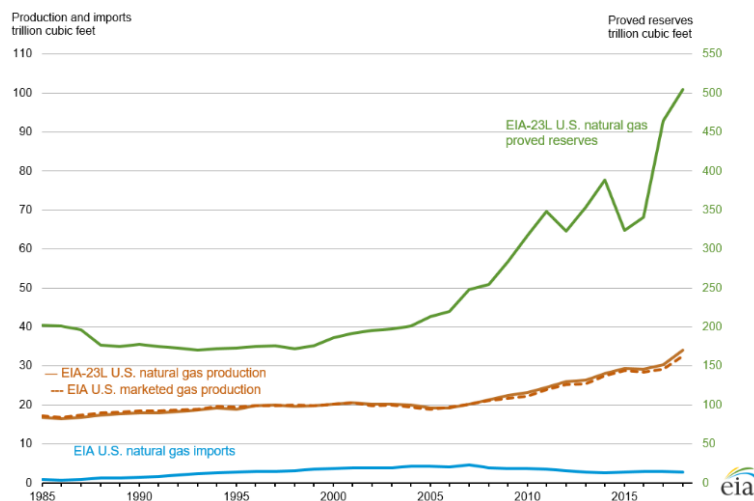
Fig. 1.1. US total natural gas proved reserves, production, and imports from 1985 – 2018, based on [5].

Biogas also contains CH_4 and CO_2 in approximately 3:2 molar ratio and could also be utilized as an important feedstock for natural gas [6]. Biogas is generally produced by anaerobic digestion of organic material. For instance, 266 million tons of solid waste in the United States was landfilled which decomposed to produce approximately 67 % of biogas [7]. Natural gas derived from petroleum reserves and biogas generated from anaerobic digestion constitutes methane as main component (60%–90%). Because methane is also recognized as one potent greenhouse gas [8], conversion of methane as an important C_1 feedstock to produce energy and synthesize chemicals is desirable, while simultaneously contributing to mitigate global warming effect.

1.2 Conversion of Methane: Process Analysis

Methane conversion to chemicals, including methanol, ammonia, dimethyl ether, usually goes through one indirect approach, which methane being transformed into synthesis gases first [9,10]. This is because direct conversion of CH_4 to aforementioned valuable chemicals is limited by low net-yields of products. Due to high C–H bond dissociation energy (~435 kJ/mol), direct conversion of CH_4 becomes impractical. [11]. Syngas – which mainly comprise of CO and H_2 in varying ratio (H_2:CO = 1 – 3) is produced by reforming of CH_4 with an oxidizing agent such as H_2O, O_2 or CO_2. The H_2:CO ratio mainly depends on the oxidizing agent employed.

Few technologies are currently available for methane transformation. They are: steam reforming of methane (SRM) [12–13], partial oxidation of methane (POM) [14–15], dry reforming of methane (DRM) [16–19], combined reforming of methane (CRM) [20–21], autothermal reforming of methane (ATR) [22] and tri-reforming of methane (TRM) [23]. Table 1.1 lists typical reforming reactions, stoichiometry, H_2:CO ratio of syngas and reaction enthalpy [24].

Table 1.1 Reaction, stoichiometry, H$_2$:CO ratio and enthalpy ΔH_{298K} for methane reforming processes.

Reaction	Stoichiometry	H$_2$:CO ratio	ΔH_{298K} (kJ/mol)
SRM	$CH_4 + H_2O \rightarrow CO + 3H_2$	3	206.8
POM	$CH_4 + \dfrac{1}{2}O_2 \rightarrow CO + 2H_2$	2	-35.6
DRM	$CH_4 + CO_2 \rightarrow 2CO + 2H_2$	1	247.3
CRM	$3CH_4 + 2H_2O + CO_2 \rightarrow 4CO + 8H_2$	2	660.9
ATR	$7CH_4 + 3O_2 + H_2O \rightarrow 7CO + 15H_2$	2.2	-6.8
TRM	$20CH_4 + H_2O + 9O_2 + CO_2 \rightarrow 21CO + 41H_2$	1.9	12.9

Steam reforming of methane (SRM) is widely used in industry to produce hydrogen-rich syngas which is typically employed to synthesize ammonia. Partial oxidation of methane (POM) produces syngas with H$_2$:CO ratio as 2:1 which is considered ideal from methanol synthesis viewpoint. However, partial oxidation of methane is practically undesirable due to safety considerations [25]. Dry reforming of methane (DRM) has been shown to be ideal among methane reforming technologies. Because DRM consumes two important greenhouse gases in single reaction while simultaneously producing equimolar mixture of H$_2$ and CO. H$_2$:CO ratio of ~ 1 is desirable for production of long-chain hydrocarbons and oxy-alcohols by Fischer-Tropsch (F–T) synthesis over Fe-based catalysts [26]. Apart from SRM, POM and DRM, other methane reforming technologies such as CRM, ATR and TRM could also be employed according to the

requirements of H_2:CO ratio in syngas. Fig. 1.2 shows brief outline of methane reforming technologies to various downstream chemicals production. From economic point of view, dry reforming of methane (DRM) is accepted as ideal technology for methane reforming. This is attributed to less energy consumption (~20%) compared to various methane reforming techniques [10].
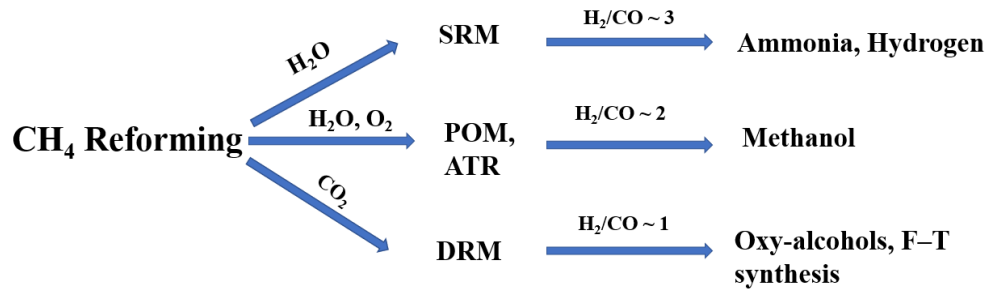
Fig. 1.2. Overview of CH_4 reforming technologies in downstream chemicals production.

Dry reforming of methane is highly endothermic reaction with ΔH_{298K} = 247.3 kJ/mol [24]. Thus, high reaction temperature such as 900°C is required to obtain high syngas yields. The standard Gibbs free energy calculation for DRM process is evaluated from equation 1. Equation 1 shows that minimum temperature required for spontaneous DRM process would be more than 643°C [24].

$$CH_4 + CO_2 \leftrightarrow 2CO + 2H_2, \qquad \Delta G^0 = 61770 - 67.32\ T\ kJ/mol \qquad (1)$$

$$CO_2 + H_2 \leftrightarrow CO + H_2, \qquad \Delta G^0 = -8545 + 7.48\ T\ kJ/mol \qquad (2)$$

$$CH_4 \rightarrow C + 2H_2, \qquad \Delta G^0 = 2190 - 26.45\ T\ kJ/mol \qquad (3)$$

$$2CO \rightarrow C + CO_2, \qquad \Delta G^0 = -39810 + 40.87\ T\ kJ/mol \qquad (4)$$
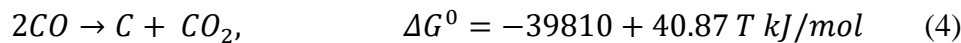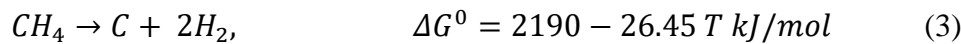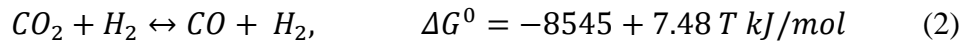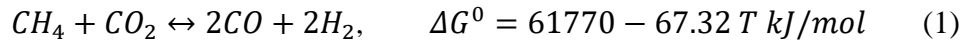
Side reactions during the dry reforming of methane affects the yield to syngas. The prominent side reactions include reverse water-gas shift (RWGS), methane decomposition (MD) and CO disproportionation. Reverse water gas shift reaction consumes H_2 formed by CH_4 dissociation and

reacts with CO_2 to form CO and H_2O shown in equation 2. Thus, RWGS lowers H_2/CO ratio and is the dominant reaction in the temperature 350˚C–750˚C. However, above 750˚C, the formation of H_2O due to RWGS becomes minimal and H_2/CO ratio approaches unity. Methane decomposition (MD) and CO disproportionation as side-reactions forms active/inactive carbon species leading to catalyst deactivation. The thermodynamic Gibbs free energy for methane decomposition (MD, Equation 3) and CO disproportionation (Equation 4) reaction depends on the reaction temperature.

Fig. 1.3 shows thermodynamics of DRM reaction under the consideration of methane decomposition and CO disproportionation. Coke formation is generally inevitable in the temperature range between 300˚C–700˚C and high pressures (> 1 atm). When the temperature is above 700˚C, CO_2 starts to dissociate effectively into CO and O^* (surface adsorbed oxygen species). O^* derived from CO_2 dissociation could oxidize coke on catalyst surface thereby enhancing CO yield. Fig. 1.4 shows that with increase in pressure, coke formation is favored. Typically, CH_4 decomposition is suppressed while CO disproportionation dominates at pressure > 1 atm [24]. In order to address the carbon deposition issue during DRM, various approaches could be employed. For example, the ratio of $CH_4:CO_2$ in the feed could be varied [27]. Typically, equimolar mixture of CH_4 and CO_2 is fed above 1000˚C for reforming which produces H_2 and CO in 1:1 ratio. However, carbon deposition could be reduced by using $CH_4:CO_2$ ratio below one. Thus, CO_2 conversion is higher than CH_4, while H_2/CO ratio is usually below unity. Thus, alternative strategies are necessary to obtain H_2/CO above unity while simultaneously oxidizing coke from catalyst surface.
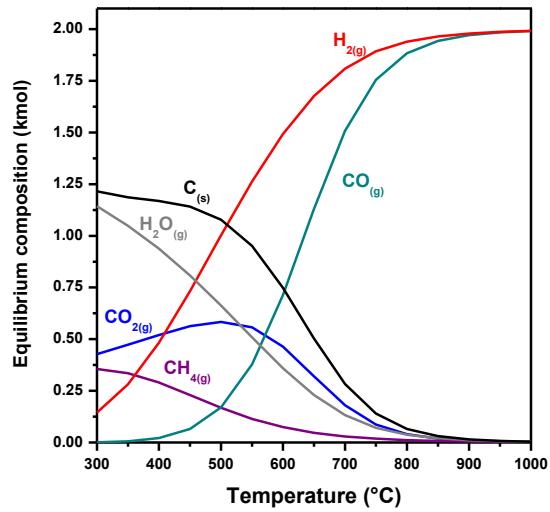
Fig. 1.3

Fig. 1.3. Thermodynamic equilibrium plot for DRM at 1:1 CO_2/CH_4 inlet feed ratio between 300˚C-1000˚C under the consideration of carbon formation, produced in ASPEN Plus V11.
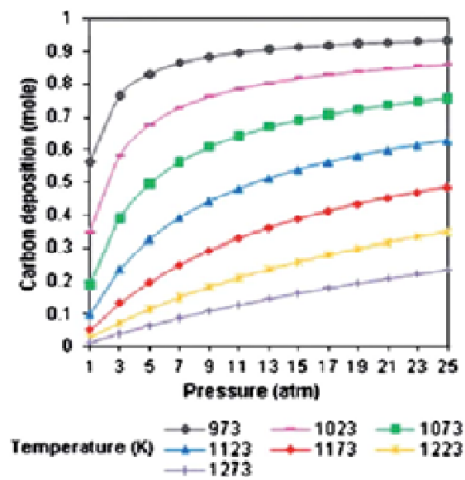
Fig. 1.4

Fig. 1.4. Change in coke formation at 1:1 CO_2/CH_4 inlet feed ratio between 1–25 atm pressure, reproduced from [24].

To meet this requirement, oxidizing agents such as H_2O and/or O_2 could be fed along with CO_2 and CH_4 into reformer which might produce syngas with H_2/CO above unity [28]. Thereby combined steam and dry reforming of methane could be one potential option. Combined steam

6

and dry reforming of methane (CRM) offers flexibility in H_2/CO ratio by varying $CH_4/H_2O/CO_2$ ratio in feed and could also stabilize catalyst by oxidizing coke from catalyst surface [28–30]. Secondly, CRM utilizes nonhazardous feed that could be considerate from safety aspects. However, autothermal reforming (ATR) combines partial oxidation of methane (POM) and steam reforming of methane (SRM) in a single reaction to form syngas with $H_2/CO \sim 2.2$. ATR is often carried out in industry in which 2:1 molar ratio of CH_4/O_2 is heated and fed in steam reformer tubes. Nonetheless, ATR has its drawbacks due to safety concerns attributed to O_2 in feed with CH_4 [9]. Moreover, for ATR, a plant separating O_2 from air also need to be built which adds to manufacturing cost of reforming unit. It is not one cost-effective approach in terms of commercialization of ATR. Tri-reforming of methane (TRM) [31–32] combines DRM along-with SRM and POM in a single reaction as shown in Table 1.1. TRM offers one great advantage of combination of exothermicity from POM and endothermicity from DRM and SRM. With ΔH_{298K} = 12.9 kJ/mol, TRM seems to be thermo-neutral process which produces H_2/CO ratio of ~ 1.9. Thus, tuning the feed ratio might be helpful in achieving desirable H_2/CO ratios and coke deposits mitigation.

In summary, DRM could be one potential choice due to following reasons. 1) DRM could be conducted with natural-gas or biogas resulting in no separation of feed mixture. 2) DRM utilizes two important greenhouse gases in a single reaction to form syngas. 3) DRM excludes the use of O_2 with CH_4 in the feed which might prove fatal from safety considerations. 4) By changing the ratio between CH_4 and CO_2, H_2/CO ratio could be manipulated thereby making DRM to be ideal among reforming processes. 5) DRM could emerge as better alternative to CRM due to high endothermicity of CRM ($\Delta H_{298K,CRM} = 660.9$ kJ/mol vs $\Delta H_{298K,DRM} = 247.3$ kJ/mol).

1.3 Dry Reforming of Methane (DRM)

Dry reforming of methane yields equimolar ratio of CO and H_2. The syngas, mixture of carbon monoxide and hydrogen, is one important platform chemical to produce hydrocarbons and alcohols with suitable catalysts and optimized operation conditions [33]. Catalyst deactivation is the biggest challenge for the development of robust catalysts for DRM reaction. To increase CH_4 and CO_2 conversion and syngas yield, high temperature (>850°C) is necessary. But metal supported oxides catalysts are prone to sintering when temperature is above 850°C. The sintering could be related to the irreversible reaction between active metals and support, which leads to the formation of inactive spinels [34]. While, sintering may also occur due to loss of active metals on catalyst surface. Specifically, when T_{Huttig} ($0.3T_{melting}$) and $T_{Tammann}$ ($0.5T_{melting}$) are reached, metal atoms from the defect and bulk would exhibit mobility [35]. This behavior may cause loss of active site from catalyst surface. However, strong interaction between metal and support might prevent sintering due to metal atom mobility. Nevertheless, the primary reason for catalyst deactivation is suggested to be unavoidable coke formation – which is, however, thermodynamically not favored at high temperature. Coking usually occurs through side-reactions such as CH_4 decomposition and CO disproportionation reaction which are thermodynamically favored below 700°C [34]. Thus, development of stable and active DRM catalysts is desirable.

1.3.1 Catalyst development

1.3.1.1 Precious metals based catalysts

Precious metals such as Ru, Pt, Ir, Pd and Rh [36-38] and non-precious metals such as Ni and Co [39,40], have been studied for dry reforming of methane. Precious metals show higher activity

8

and coke resistance due to their unique properties [24]: i) exposure of d-subshell electron; ii) highly dispersed nanoparticles which enhance dissociative adsorption of H_2/O_2.

Among Ru supported catalysts, $Mg_3(Al)O$ is one better support among the choices of MgO, γ-Al_2O_3, $MgAl_2O_4$ and $Mg_3(Al)O$. 2wt% $Ru/Mg_3(Al)O$ catalysts exhibited superior catalytic activity and stability over 30 h TOS at 750˚C [41]. TEM analysis of spent catalysts confirmed sintering occurred over Ru/MgO, Ru/γ-Al_2O_3 and $Ru/MgAl_2O_4$. Highly dispersed Ru nanoparticles over $Mg_3(Al)O$ support prevented sintering during DRM. Enhanced stability performance of $Ru/Mg3AlO$ was attributed to high Ru dispersion. The increased dispersion is related to surface defects observed over non-crystalline $Mg_3(Al)O$. Upon calcination and reduction, highly dispersed Ru nanoparticles were partially embedded inside the support matrix [40]. Combined *in-situ* XRD and XAFS analysis [42] showed that Ru nanoclusters of size < 1 nm partially formed as oxidized Ru species in close contact with ceria. Ru nanoclusters over ceria, $Ru^{\delta+}$–CeO_{2-x} is thermally stable.

High oxygen mobility originated from metal-support interactions facilitated DRM stability up to 25 h TOS. Activity and stability deteriorated when Ru nanoparticles size increased to 4 nm. Damyanova et. al [43] studied Pt/ZrO_2 catalyst at 550˚C for DRM. They showed that highly dispersed Pt^0 species were responsible for pronounced CH_4 conversion. However, introduction of 1-6 wt% CeO_2 resulted in decreased catalytic activity. The presence of atomically dispersed Ce was attributed to inhibit the interaction between Pt and Zr on metal-support interface thereby decreasing the activity. Besides carbon formation, Pt/Al_2O_3 sintered during DRM reaction due to low metal dispersion. But addition of promoters such as Pr, Zr and Nb in Pt/CeO_2-Al_2O_3 catalyst showed improved activity and carbon resistance compared to Pt/Al_2O_3 [44]. Particularly, high oxygen storage/release capacity of $Pt/CePr$-Al_2O_3 facilitated carbon removal from Pt^0 surface.

Improved reducibility and metal dispersion over Pt/CePr-Al$_2$O$_3$ contributed to stability during DRM.

Ir catalysts supported on Ce$_{0.9}$Pr$_{0.1}$O$_{2,}$ which were prepared by deposition-precipitation (DP) method showed highest catalytic activity in DRM reaction at 750˚C [45]. Catalysts prepared by co-precipitation (CP) and sequential-precipitation (SP) exhibited much lower activity. TEM analysis demonstrated that Ir metal was fully or partially embedded in the matrix of Ce$_{0.9}$Pr$_{0.1}$O$_2$-CP and Ce$_{0.9}$Pr$_{0.1}$O$_2$-SP support. High density of Ir nanoparticles over Ce$_{0.9}$Pr$_{0.1}$O$_2$-DP support explained its maximum activity. Characterization of spent catalysts after 200 h TOS revealed sintering of Ir nanoparticles while no coke deposition was observed. However, introduction of 10 wt% Mg in Ir/Al$_2$O$_3$ catalyst showed improved sintering resistance and coke resistance in DRM for 59 h TOS [46]. XRD analysis of Mg modified Al$_2$O$_3$ support revealed formation of magnesium aluminate spinel. The high sintering resistance of Ir/Mg-Al$_2$O$_3$ catalyst was attributed to metal support interaction.

Rh/γ-Al$_2$O$_3$ prepared by atomic-layer deposition (ALD) and incipient wetness impregnation (IWI) demonstrated coke resistant at 800˚C [47]. However, EDX-TEM analysis of spent catalysts revealed metal-sintering which caused catalyst deactivation. Alternatively, Rh/γ-Al$_2$O$_3$ prepared by wet impregnation method showed coke deposition during DRM at 750˚C [48]. Modifying Al$_2$O$_3$ support with 20 wt% Ce$_{0.5}$Zr$_{0.5}$O$_{2-\delta}$ decreased coke deposition as compared to Rh/Al$_2$O$_3$. Conclusively, Rh/Ce$_{0.5}$Zr$_{0.5}$O$_{2-\delta}$ demonstrated least coke formation. Surface oxygen vacancies in Ce$_{0.5}$Zr$_{0.5}$O$_{2-\delta}$ support may activate CO$_2$ by dissociative adsorption forming CO and O*. This O* species could promote gasification of coke on the support and Rh sites. Catalytic activity followed the order: Rh/Al$_2$O$_3$ > Rh/Al$_2$O$_3$-Ce$_{0.5}$Zr$_{0.5}$O$_{2-\delta}$ > Rh/Ce$_{0.5}$Zr$_{0.5}$O$_{2-\delta}$. HRTEM analysis of used

catalysts showed no significant changes in Rh particle size. The results also suggested sintering resistance of Rh during DRM.

Singha et al. [49] investigated Pd/CeO_2 for DRM reaction. Highly dispersed Pd nanoparticles activated CH_4 at temperature as low as 350˚C. XRD and TEM analysis of spent catalysts after 12 h TOS at 800˚C showed sintering of Pd nanoparticles while no coke deposition was observed. Water produced due to RWGS reaction caused hydroxylation of Pd nanoparticles and was evidenced by presence of $Pd(OH)_4$. $Pd@SiO_2$ core-shell nanocatalysts demonstrated resistance to coking and sintering during DRM at 750˚C [50]. It was suggested that SiO_2 shell of $Pd@SiO_2$ catalyst would divide Pd nanoparticles into small ensembles of Pd which inhibited coke formation. Upon calcination, mesopores of diameter ~ 7.5 nm were formed in the shell which inhibited agglomeration of Pd and growth of filamentous carbon.

1.3.1. 2 Non-Precious metal based catalysts

I) Nickel based catalysts

Precious metals might not be potential choice for industrial application of DRM reaction due to i) catalyst deactivation caused by active metal sintering; ii) high cost in comparison to active non-precious metals such as Ni and Co.

Bradford and Vannice demonstrated that turnover frequency of active metals in DRM reaction followed the order: Ru > Rh > Ni, Ir > Pt > Pd [51]. The different activity was attributed to difference in metal-support interaction. Additionally, participation of O or OH species from the support in metal-support interfacial region might also influence the catalytic activity. However, considering the cost-effectiveness of the active metal catalysts for DRM, Ni or Co might prove better option compared to precious metals. Secondly, recovering of active precious metals

including Pt and Ir would add to the cost of reforming process. Therefore, Ni and Co based catalysts have been investigated [52-54].

Monometallic Ni and Co based catalysts are prone to catalyst deactivation because of carbon formation and metal sintering. Ni/Al_2O_3 catalysts prepared by incipient wetness impregnation and solution combustion synthesis (SCS) methods showed 39.4% and 20% coke deposition during 50 h TOS. Strong metal-support interaction induced in Ni/Al_2O_3 (SCS) catalyst might attribute towards decreased coking [55]. Carbon deposition could be suppressed from 1.95 to 0.13 $\mu mol_C/g_{catalyst}$ [56] while unreduced and calcined Ni/Al_2O_3 catalyst was coated with ALD alumina. Interaction of alumina overcoat with Ni sites enhanced strong metal support interactions. Reduction of $NiAl_2O_4$ spinel to Ni^0 during DRM reaction was responsible for increase in catalytic activity with 20 h TOS.

Morphology of support would also influence the catalytic activity, stability and coke deposition [57]. Maximum coke deposition (23 wt%) was observed over Ni/Al_2O_3 nanoparticles. While, Ni/Al_2O_3 catalyst with nanofiber type morphology exhibited maximum stability and least coke deposition. Al_2O_3 support with nanofiber type morphology may possess basic sites to promote CO_2 chemisorption. Doping 25% TiO_2 with Al_2O_3, improved catalytic activity and stability in DRM. [58]. TiO_2 facilitated redox properties and balanced metal support interactions. Introduction of TiO_2 altered type of deposited coke from graphitic to amorphous, suppressing catalyst deactivation.

II) Cobalt-based catalysts

Co-based monometallic catalysts have been also investigated in DRM reaction. Guo and co-workers showed that 10 wt% Co supported on MgO and Al_2O_3 deactivated during DRM reaction

due to active metal sintering [59]. Further, employing Mg(Al)O hydrotalcite-type material as support improved the activity and stability in terms of coking and sintering resistance. They showed that formation of CoO-MgO solid solution from hydrotalcite type compounds would increase the account of medium-strength basic sites which were suggested to be crucial for CO_2 activation. Co/AlO_x catalyst prepared by co-precipitation approach was inactive in DRM due to formation of $CoAl_2O_4$ spinel [60]. However, introduction of MgO in Co/AlO_x composite facilitated formation of CoO-MgO solid solution which increased the degree of $CoAl_2O_4$ spinel inversion. Further, addition of MgO enhanced the reducibility and basicity of Co/AlO_x. DRM activity at 750˚C over $Co/MgAlO_x$ showed stable performance for 15 h TOS with no obvious signs of coke deposition.

Besides coking, oxidation of active metal species also caused catalyst deactivation [40,61]. For example, Co/ZrO_2 deactivated during DRM reaction by oxidation of Co^0 to CoO_x [62]. Due to strong basicity of ZrO_2, enhanced CO_2 dissociation was facilitated. However, owing to high oxophilicity of Co, surface oxygen species (O^*) derived from CO_2 dissociation oxidized Co^0 to inactive CoO_x. Basic character of ZrO_2 support was inhibited by addition of 1 wt% Al to ZrO_2 support [62]. Consequently, $Co/AlZrO_2$ showed stable catalytic performance in DRM at 850˚C. Strong interaction of Co species with Al in metal-support interfacial region inhibited Co^0 oxidation. Similarly, deactivation was ascribed to oxidation of Co [61] over $Co-TiO_2$ catalysts. Unlike $Co/AlZrO_2$ catalyst [62], strong metal support interaction between Co and TiO_2 lead formation of inactive $CoTiO_3$ phase during DRM.

III) Precious metals modified Ni- and Co-based catalysts

Monometallic catalysts might not prove economical from industrial application of DRM due to following reasons: i) Active precious metals such as Pt, Ru, Rh and Ir might prove expensive

from economic point of view. ii) Inexpensive Ni and Co catalyst show deactivation due to coke formation and/or metal oxidation. One potential option could be promoting Ni and Co based catalysts with trace amount of precious metals such as Pt, Ru, Rh and Pd [63-66]. Addition of precious metals to Ni catalysts might improve catalytic performance and coke resistance due to increased reducibility, enhancement in number of active sites, surface modification and reconstruction [67].

Ni-Pt catalysts prepared by atomic layer deposition (ALD) method showed increased reducibility upon 1 wt% Pt addition to 4.7 wt% Ni. The catalytic activity was increased by 2 folds. While, formation of Pt defects increased carbon diffusion barrier on Ni terrace sites, thereby resisting coke formation [68]. Similarly, adding 3 wt% Pt to 9 wt% Ni showed enhancement in DRM activity due to surface modification of Ni catalyst [69]. Further, carbon formation was inhibited by addition of Pt which facilitated oxidation of CH^* species and hindered carbon diffusion. Plasma pretreatment during preparation of 8 wt% Ni + 0.1 wt% Pt supported on Mg(Al)O facilitated higher surface concentration of Ni compared to monometallic Ni/Mg(Al)O [70]. Addition of 0.1 wt% Pt would increase Ni dispersion and thereby enhance catalyst reducibility. Moreover, coke deposition was mitigated upon Pt addition which was attributed to reduction in particle size and modification of Ni ensembles.

Ru promoted Ni catalysts have been investigated [71]. Reactivity of carbonaceous intermediates would increase upon doping 0.6 wt% Ru to 2 wt% Ni. Increased reactivity of carbon intermediates decreased coking. Addition of Ru would also increase Ni dispersion which would enhance catalytic activity and stability [71,72]. Bobin et al. [73] suggested that formation of Ni–Ru clusters could enhance CO_2 dissociation. Increased rate constant for coke gasification suggested enhanced formation of O^* species formed by CO_2 dissociation.

Rivas and co-workers [74] investigated $LaNi_{0.95}Rh_{0.05}O_3$ perovskites in DRM reaction. Addition of Rh would enhance reducibility and dispersion of Ni. *In-situ* XRD and TEM analysis showed drastic changes in the crystalline network of perovskite-type precursor upon Rh addition. The formation of highly dispersed Ni^0-Rh^0 particles enhanced the activity compared to monometallic Ni catalyst. Bimetallic Ni–Rh supported over boron nitride (BN) was studied by Wu et al [75]. Inertness of support and weak metal-support interaction allowed metal clusters to migrate freely and form Ni–Rh clusters during reduction. The close proximity of Rh with Ni would decrease carbon formation while simultaneously increase the activity compared to monometallic Ni/BN catalyst.

Ma and co-workers [76] investigated mono and bimetallic Ni–Pd catalysts. Addition of 0.5 wt% Pd to 6 wt% Ni would enhance the reducibility of NiO and facilitate the formation of Ni–Pd nanoalloy. Introduction of Pd maintained catalyst stability up to 100 h TOS. The role of Pd was suggested to inhibit filamentous coke formation. Damyanova et al. [77] studied Ni-Pd/MCM-41 catalysts in DRM reaction and showed that Ni:Pd ratio of 4:1 would be optimum to achieve high metallic surface area, metal dispersion and reducibility of Ni. Formation of Pd^0 during reduction facilitated enhanced reduction of NiO by H_2 spill-over phenomenon.

Monometallic Co based catalyst are prone to deactivation due to oxidation of Co^0 by CO_2 [40]. To address this issue, Takanabe et al. [78] synthesized Pt and Ru promoted Co/TiO_2 catalysts. The role of Pt and Ru was attributed to maintain metallic state of Co^0. For $Co/\alpha\text{-}Al_2O_3$, addition of trace amount of Ru (0.1 wt%) in 5 wt% $Co/\alpha\text{-}Al_2O_3$ restricted oxidation of Co^0 [79]. The addition of Ru also inhibited coke deposition. The initial activity over $Co/\alpha\text{-}Al_2O_3$ was higher than Ru-$Co/\alpha\text{-}Al_2O_3$. However, Co^0 oxidation and coke deposition caused deactivation of $Co/\alpha\text{-}Al_2O_3$ in

100 h long run. But Ru-Co/α-Al$_2$O$_3$ demonstrated higher and stable activity after 100 h DRM tests.

The catalytic performance of bimetallic Ru-Co@SiO$_2$ pore shell catalysts depended strongly on catalyst synthesis approach [80]. Specifically, Ru-Co@SiO$_2$ prepared by hydrothermal method showed even distribution of Ru on catalyst surface. The synergism between Ru-Co prevented Co oxidation and catalyst deactivation. Ru-Co@SiO$_2$ prepared by impregnation route caused uneven distribution of Ru on catalyst surface which decreased DRM activity and enhanced coke deposition. The SiO$_2$ shell structure suppressed sintering of Ru-Co.

Besides Ru, promotional effect of Pt in Co-based catalysts is also studied. Chen et al. [81] investigated trace amount of Pt (0.05 – 0.5 wt%) addition to 10 wt%Co/MgO-Al$_2$O$_3$. Strong metal support interaction (SMSI) effect was induced in Co-0.2 Pt catalyst. Addition of Pt promoted the formation of CoAl$_2$O$_4$ spinel which showed increased reducibility. Ultimately, enhanced activity and decreased coke deposition was observed over Co-0.2 Pt/MgO-Al$_2$O$_3$. Synergistic effect between bimetallic Pt-Co/CeO$_2$ catalysts increased the DRM activity in comparison to monometallic Pt/CeO$_2$ and Co/CeO$_2$ catalysts [82]. CeO$_2$ facilitated enhanced CO$_2$ activation forming surface oxygen species O* and supplied O* on Pt/CeO$_2$ surface. While presence of Co promoted the formation of O*. Collectively, O* species were shown to enhance methane activation by CH$_4^* + $ O$^* \rightarrow$ CH$_3^* + $ OH* reaction. However, Pt-Co/CeO$_2$ catalyst displayed high coke formation compared to monometallic Co/CeO$_2$ and Pt/CeO$_2$ catalysts.

Overall, the role of Ru and Pt addition in Co-based catalysts has been attributed to hydrogen/oxygen spill-over phenomenon [40,61,78]. Owing to high reducibility of Ru and Pt compared to Co, it is suggested that addition of Ru and Pt would assist hydrogen dissociation on catalyst surface. This would ultimately prevent oxidation of Co during DRM.

IV) Transition metals modified Ni-based catalysts

Besides promoting Ni catalysts with precious metals, addition of transition metals such as Fe, Co or Cu might also prove beneficial to improve activity and stability of Ni catalysts. Introduction of Fe in monometallic Ni catalysts [83] improved the activity and stability of $Ni/MgAl_2O_4$ hydrotalcites through Fe^{2+}/Fe^0 redox cycle. Under DRM conditions, Fe^0 in Ni-Fe alloy would be partially oxidized to FeO upon CO_2 exposure as shown in Fig. 1.5. FeO located on surface of Ni-Fe nanoparticles would remain in close proximity to Ni^0. FeO formed upon CO_2 exposure would react with deposited carbon to form CO and Fe^0. Thus, introduction of Fe would facilitate better activity, stability and coke resistance compared to monometallic $Ni/MgAl_2O_4$ catalyst.
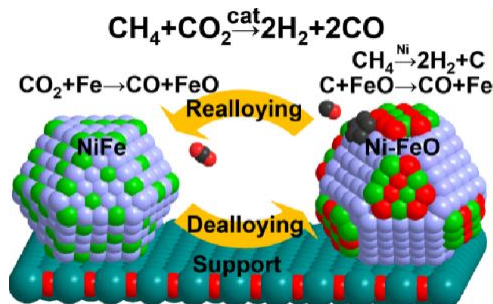
Fig. 1.5. Dealloying and Realloying mechanism during DRM over $Ni–Fe/MgAl_2O_4$ catalyst, reproduced from [83].

Ni-Fe catalysts supported on Mg(Al)O periclase for DRM prepared by colloidal synthesis approach [84] was further studied. Specifically, influence of reduction temperature on catalytic activity was studied. Increasing reduction temperature from 650˚C to 850˚C would change the surface population sites from $Ni^0/FeO_{(at\ 650˚C)}$ to $Ni–Fe_{\ alloy}/FeO_{(at\ 850˚C)}$ during reduction. While under DRM conditions, Fe^0 oxidizes to FeO and tends to migrate into the support periclase to some extent. Catalytic performance in DRM for 30 h TOS showed high activity over Ni-Fe catalysts reduced at 650˚C than catalysts reduced at 850˚C. Low activity over $Ni–Fe_{\ alloy}/FeO_{(at\ 850˚C)}$ was

attributed to presence of significant amount of surface Fe^0 sites [84]. FeO formed upon CO_2 exposure during DRM was shown to oxidize coke to CO.

Theofanidis et al. investigated Fe-Ni/$MgAl_2O_4$ catalysts in the molar ratio of Fe/Ni between 0-1.5 [85]. Optimum activity and stability were facilitated by Fe/Ni ratio of 0.7. Further increase in Fe concentration deteriorated the activity. Using time resolved *in-situ* XRD during H_2-TPR, the formation of Ni-Fe alloy upon reduction at 700°C was confirmed. Ni-Fe alloy would remain stable up to 627°C under CO_2-TPO condition. Upon DRM exposure, the Ni-Fe alloy would decompose to form Ni and FeO_x as shown in Fig. 1.6. Alternative CH_4 and CO_2 pulse experiments suggested that DRM over Ni-Fe/$MgAl_2O_4$ would proceed through Mars–van Krevelen mechanism. Metallic Ni would dissociate methane to H_2 and coke. While, coke formed on Ni sites is oxidized to CO from lattice oxygen present in FeO_x. Deactivation of Ni/$MgAl_2O_4$ was attributed to high rate of coke deposition than coke gasification. Compared to Ni/$MgAl_2O_4$, bimetallic Fe-Ni/$MgAl_2O_4$ showed better stability and coke resistance [85].
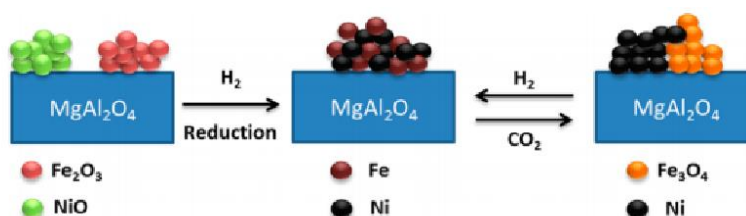
Fig. 1.6. Ni-Fe alloy formation during reduction and dealloying upon CO_2 exposure, reproduced from [85].

Same group investigated Ni catalysts supported on $MgFe_xAl_{2-x}O_4$ for DRM in which Al was partially replaced by Fe in the octahedral spinel of lattice support [86]. During reduction, approximately 50% of Fe from the support would migrate onto the surface by hydrogen spill-over phenomenon. Migration of Fe onto the surface formed Ni–Fe alloy during reduction as shown in

Fig.1.7. Conclusively, Ni–Fe/MgFe$_x$Al$_{2-x}$O$_4$ showed stability and no coke formation up to 65 h TOS. Li and co-workers studied bimetallic Fe-Ni catalysts supported on mesoporous alumina in DRM reaction [87]. A molar ratio of 0.7 Fe/Ni was shown to be optimum which promoted the initial activity. The active phase for DRM was suggested to be FeNi$_3$ alloy. Characterization of spent catalysts showed that bimetallic Ni–Fe nanoparticles were resistant to coking and sintering. Confinement of Ni-Fe nanoparticles onto porous structure of Al$_2$O$_3$ contributed towards coking and sintering resistance. STEM-EDX and XPS analysis showed that FeNi$_3$ alloy nanoparticles would partially dealloy during reforming reaction. Dealloying of FeNi$_3$ alloy was suggested for catalyst deactivation during 24 h TOS reaction.
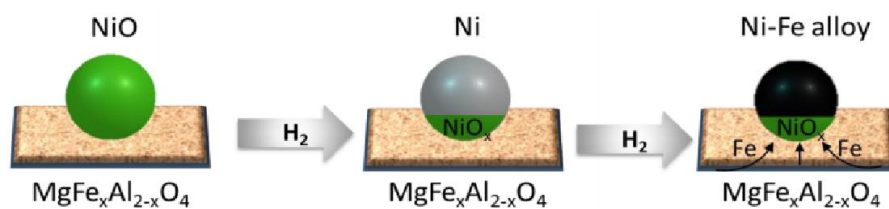
Fig. 1.7. Schematic representation of Ni–Fe alloy formation on Ni/MgFe$_x$Al$_{2-x}$O$_4$ upon Fe migration from support during reduction, reproduced from [86].

Ni-Fe perovskites were investigated for DRM reaction [88,89]. Partial substitution of Ni by Fe in LaNiO$_3$ perovskites would significantly enhance the structure stability and coke resistance in DRM. LaNiO$_3$ decomposed to Ni^0 metal and La$_2$O$_3$ support during DRM which was prone to coke deposition. Contrarily, LaNi$_{0.5}$Fe$_{0.5}$O$_3$ phase was stable and coke resistance during DRM. The role of Fe in LaNiO$_3$ perovskites was attributed to enhance Ni dispersion and metal-support interaction [88]. Contradictorily, Ni-Fe catalysts supported on La$_2$O$_3$ obtained by reduction of LaNi$_{0.8}$Fe$_{0.2}$O$_3$ – type perovskite did not show activity in DRM reaction [18]. The perovskite structure collapsed after reduction and Ni-Fe nanoparticles embedded in to the La$_2$O$_3$ matrix. *In-situ* XRD and EDX

elemental mapping revealed dealloying of Ni-Fe nanoparticles during DRM. Upon CO_2 exposure, Fe oxidized to FeO_x and formed $LaFeO_3$. $LaFeO_3$ was shown to encapsulate active Ni particles, ultimately deactivating the catalyst. Therefore, for Ni-Fe perovskite type of catalysts, structural stability could play significant role in DRM activity.

Alloying Fe with Ni significantly enhanced the stability of Ni-Fe/MgO catalysts in DRM reaction [90]. Addition of Fe in pristine Ni/MgO catalyst would facilitate formation of small Ni ensembles. The role of Fe was attributed to division of large Ni ensembles by catalytically inactive Fe atoms as shown in Fig. 1.8. Small ensembles of Ni atoms favored DRM over CH_4 decomposition. Secondly, addition of Fe increased the surface coverage of O^* species which was ascribed to oxophilicity of Fe. Collectively, introduction of Fe changed the type of deposited coke from inactive refractory carbon to soft carbonaceous species. The active – soft carbonaceous species were oxidized under CO_2 atmosphere during DRM, thereby enhancing catalyst stability and coke resistance.
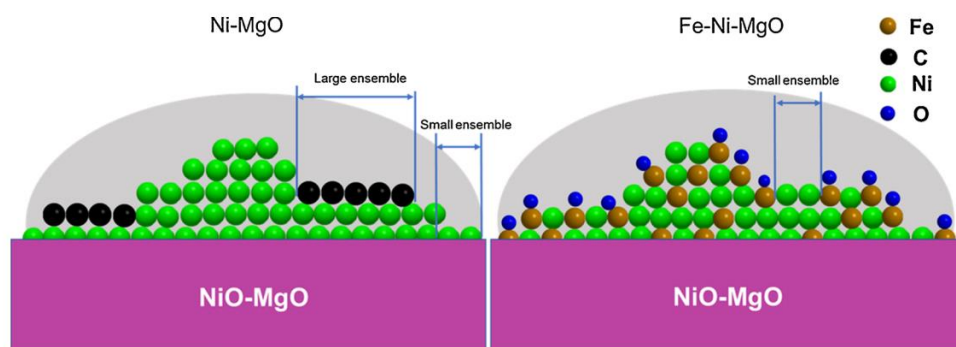
Fig. 1.8. Schematic representation of atomic structure of Ni/MgO and Ni-Fe/MgO catalysts, reproduced from [90].

Co as a promoter to Ni based catalysts has been also studied extensively in DRM [91-93]. The ratio between Ni/Co plays the important role for DRM. Ni/Co ratio of 1:9 over TiO_2 support was

suggested to be optimal for DRM by Nagaoka and co-workers [78]. While, Ni/Co ratio of 4:1 over MgO-Al_2O_3 support [94] and 7:3 over Al_2O_3-La_2O_3 [94] provided maximum catalytic activity and least coke deposition. Optimum ratio between Ni and Co may exist and could depend on the support employed. Usually, a small amount of Co is sufficient to achieve optimum activity and stability in DRM process. Fan et al. [19] synthesized bimetallic Ni-Co/MgO catalysts by hydrothermal process. A $Ni_{7.425}Co_{0.075}Mg_{92.5}O$ catalyst showed stability up to 1000 h TOS with only 1.79 wt% coke deposition after DRM tests. Enhanced stability of bimetallic Ni-Co catalysts was attributed to gasification of coke intermediates due to high oxophilicity of Co. Ni-Co-Mg-Al-O catalysts prepared by co-precipitation method showed 250 h TOS stability in CH_4 conversion [96]. TGA and DTA characterization of spent catalysts showed almost no coke deposition after 250 h TOS stability tests. Strong metal-support interaction, high metal dispersion and surface area was suggested for pronounced activity and stability of Ni-Co-Mg-Al-O.

Addition of Cu into Ni-based catalysts might improve coking resistance and stability during DRM. Song et al. [97] investigated bimetallic Ni-Cu alloy catalysts supported on Mg(Al)O. Tuning the ratio between Cu/Ni could have either promoting or suppressing effect on catalytic activity. A catalyst with Cu/Ni molar ratio of 0.25–5 was suggested to be optimum for DRM. Ni-Cu/MgAlO catalyst with Cu/Ni ratio of 0.25–5 significantly decreased coke formation up to 1/136 times compared to Ni/Mg(Al)O. Activation energy measurements and CH_4-TPSR experiments showed increase in CH_4 dissociation barrier upon Cu addition. While, CO_2-TPSR characterization experiment demonstrated enhanced dissociation of CO_2 to CO and O^* upon Cu addition. Lee and co-workers presented that addition of 1 wt% Cu into Ni/Al_2O_3 was sufficient enough for coke-resistance and catalyst stability [98]. While, Cu content upto 5 wt% was detrimental due to high coke deposition. Similarly, for SiO_2 supported Ni-Cu catalysts, a Cu/Ni ratio between 0.12-0.2

was shown to be optimum for DRM reaction [99]. Thus, discrepancies in the optimum Cu/Ni ratio or Co/Ni ratio for Cu and Co promoted Ni- based catalysts might be attributed to differences in metal-support interactions, metal particle size, or distribution of active components.

1.3.2 Catalyst support effect

Catalyst deactivation in DRM is mainly attributed to coke formation and active metal sintering. Formation of coke would mask the active sites while sintering of active metal could decrease the metal surface area. The choices of support may affect coke formation and metal sintering thereby influencing catalytic performance.

DRM reaction is shown to proceed via mono-functional or bi-functional pathway over supported catalysts [34]. CH_4 activates on metallic sites while CO_2 may activate on metallic sites or support [100]. DRM reaction follows mono-functional pathway where both – CH_4 and CO_2 are activated on metallic sites over inert supports such as SiO_2 and boron nitride (BN) [75,101]. Over acidic supports including Al_2O_3, DRM occurs via bi-functional mechanism in which CH_4 is activated on metal sites. While CO_2 activates on support by the reaction with surface hydroxyl groups [57,67,102]. For basic support such as La_2O_3, CO_2 is activated by formation of $La_2O_2CO_3$ while CH_4 dissociates on active metal. La-oxycarbonate reacts with CH_x species formed by CH_4 decomposition to produce CO and H_2 [33,103,104]. Reducible supports including CeO_2, TiO_2, have been also studied in DRM reaction. During reduction process, metallic sites of the catalyst could dissociate H_2 on the surface [40,105-107]. Dissociation of H_2 on catalyst surface might reduce the support by hydrogen spill-over phenomenon forming oxygen defects. Oxygen defects were demonstrated as active site for CO_2 activation.

Zhang et al. [108] showed that Ni/SiO_2 catalyst synthesized through impregnation method would deactivate in DRM reaction due to coke formation. Deactivation was attributed to poor dispersion of Ni nanoparticles and weak metal-support interaction. They demonstrated that strong interaction between Ni and SiO_2 may exist when ultra-small Ni nanoparticles of ~ 3.2 nm size were prepared. Strong metal-support interaction (SMSI) effect induced by high dispersion of Ni nanoparticles over SiO_2 resulted in stable DRM reaction up to 30 h TOS at 700°C with no coke deposition and metal-sintering. Similarly, core-shell $Ni@SiO_2$ catalyst were synthesized and calcined at 500°C, 600°C and 700°C resulting in Ni nanoparticles with sizes ~ 1.4 nm, 1.9 nm and 2.6 nm respectively [109]. $Ni@SiO_2$ calcined at 600°C had medium metal-support interaction (MMSI), which showed maximum and stable DRM activity up to 40 h TOS. Those results showed that particle size depends on metal-support interaction.

Besides controlling particle size and metal-support interaction, the interfacial structure between metal and support could enhance DRM activity [110]. Herein, $Ni/CeO_2\text{-}SiO_2$ catalyst was synthesized by plasma decomposition method. Interfacial structure between metal and support would contain reactive oxygen species in close proximity with Ni nanoparticles. Such reactive oxygen species assisted in coke removal during DRM and contributed to enhanced DRM performance. Ni catalyst over inert supports such as hexagonal – boron nitride (h-BN) demonstrated coke formation due to weak metal-support interaction (WMSI) during DRM [111]. Introduction of interfacial vacancy defects on h-BNNS support (hexagonal boron nitride nanosheets) would facilitate strong metal-support interaction (SMSI). Herein, Ni was shown to be homogenously embedded on the surface of h-BNNS. This phenomenon of surface engineering of h-BNNS support would enrich active Ni sites thereby providing sintering resistance during DRM reaction. Recently, layered double hydroxide derived $(Ni,Mg)Al_2O_4$ sheets were incorporated with

h-BN to promote confinement effect and strong metal-support interaction [112]. It was shown that interface confinement effect between h-BN and $(Ni,Mg)Al_2O_4$ could resist Ni nanoparticles from agglomeration and sintering. While formation of B–OH species during DRM could facilitate oxidation of carbonaceous species. Collectively, h-BN/$(Ni,Mg)Al_2O_4$ demonstrated excellent activity and stability for 100 h TOS during DRM at 750˚C.

Ni-based catalysts over acidic supports such as Al_2O_3 are widely investigated for DRM reaction. Li et al. [113] investigated Ni catalysts over Al_2O_3 and modified Al_2O_3 supports in DRM. They showed that Ni/Al_2O_3 deactivated during 50 h DRM test due to coke formation. However, monolayer coverage of Ni/Al_2O_3 by La_2O_3 demonstrated stable activity and resistance to coking. Catalytic activity, however, decreased due to reduction in Ni surface area by La_2O_3 monolayer coverage. Modification of Al_2O_3 support by $La_2O_2CO_3$ increased metal-support interaction, Ni surface area and reducibility. Ni/Al_2O_3-$La_2O_2CO_3$ presented enhanced activity and stable performance for 50 h TOS compared to Ni/Al_2O_3. Ni catalyst over porous Al_2O_3 support prepared by atomic layer deposition (ALD) method induced strong metal-supported interaction (SMSI) effect [114]. $NiAl_2O_4$ spinel was formed during ALD deposition of Ni over porous Al_2O_3. Reduction of $NiAl_2O_4$ spinel in CO and H_2 atmosphere would form highly dispersed Ni nanoparticles which showed stable catalytic performance.

Promoting Al_2O_3 with 6 wt% CeO_2 increased Ni dispersion and support-interaction [115]. Close contact between Ni and Ce was suggested to facilitate high electron density and accessibility of active sites which improved catalytic activity and stability compared to Ni/Al_2O_3 catalyst. Among basic supports such as La_2O_3 and MgO, La_2O_3 has been extensively studied for DRM reaction [100]. Upon CO_2 exposure, La_2O_3 forms $La_2O_2CO_3$ which is supposed to react with coke precursors forming CO and H_2 [33,103,104,113]. In a comprehensive study of Ni/La_2O_3 catalysts,

Li et al. [33] showed that type of support would play important role in coke removal and catalytic activity. Uneven Ni dispersion and low surface area of Ni were observed over Ni/La_2O_3. Consequently, $La_2O_2CO_3$ formed during DRM could not react with carbon intermediates. To improve Ni dispersion and surface area, $La_2O_2CO_3$ was chosen as support, because $La_2O_2CO_3$ would induce strong metal-support interaction (SMSI). Upon reduction of $Ni/La_2O_2CO_3$, highly dispersed Ni nanoparticles would enhance catalytic activity and coke-resistance.

Strong metal-support interaction (SMSI) effect also prevails in reducible supports such as CeO_2 and TiO_2. SMSI can alter metal electronic properties via charge transfer between metal and support [116]. For Ni/CeO_2 catalysts, metal support interactions were tuned to obtain coke resistance. Specifically, reduction of Ni/CeO_2 above 600°C caused decoration/encapsulation of Ni surface by a thin layer of cerium species due to SMSI. Ultimately, adsorption and activation of CH_4 and CO_2 was inhibited. However, due to high oxygen mobility of ceria, coke was oxidized at the metal-support interface which contributed to enhanced carbon resistance [116]. Employing Zr in the lattice of CeO_2 served several purposes to improve catalytic activity in DRM [117]. Addition of 20 wt% Zr enhanced reducibility of Ni/CeO_2 and prevented sintering due to SMSI effect. Moreover, Zr restricted migration of Ni in to CeO_2 restricting $Ni_xCe_{1-x}O_{2-y}$ solid solution formation and thereby maintained Ni^0 over $Ni/CeZrO_2$ catalyst.

For TiO_2 supported Ni catalysts, stable activity performance and coke-resistance was attributed to decoration of large Ni ensembles by partially reduced TiO_x species [107]. Specifically, upon reduction at 700°C, partially reduced TiO_x species would migrate over exposed Ni surface. Migration of TiO_x over Ni surface might decrease free energy of system and induces strong metal-support interaction (SMSI) effect [40,107].

25

1.3.3 Mechanistic and Kinetic studies

1.3.3.1 Activation of CH_4 and CO_2

Ni based catalysts have been extensively investigated for dry reforming of methane. The activation sites for CH_4 and CO_2 depend strongly on the choices of catalysts. For example, activation of CH_4 proceeds through direct dissociation of C–H bond over metallic Ni over Ni/SiO_2 and Ni/Al_2O_3 catalysts [34,100]. While, activation of CH_4 occurred via oxidative dehydrogenation of C–H bond over Ni pyrochlore and Ni perovskite catalysts [118,119]. Using labelled isotopic experiments, Kumar et al. [118] demonstrated that O^* species derived from CO_2 dissociation initiated the breakage of C-H bond. XPS analysis of O 1s spectra identified presence of lattice oxygen species which would facilitate activation of CH_4 over $La_{0.8}Sr_{0.2}Ni_{0.8}M_{0.2}O_3$ (M = Bi, Cu Co, Fe or Cr) perovskites [119].

Meanwhile, CO_2 activation proceeds through one of the following routes: 1) dissociation on active Ni^0 site to form CO^* and O^* species over SiO_2 supported catalysts [108], 2) H^* assisted activation in metal–support interface followed by dissociation of formate ($HCOO^*$) species [110,120], 3) activation on oxygen vacancies over reducible supports including CeO_2 and ZrO_2 [116,121] and 4) reaction with basic supports, such as La_2O_3, to form $La_2O_2CO_3$ species [113,122]. Briefly, the activation of CH_4 and CO_2 over Ni catalysts can be represented by following equations.

(A) CH_4 activation:

(i) $CH_4^* \rightarrow C^* + 2H_2$ (5)

(ii) $CH_4^* + O^* \rightarrow CH_3^* + H^*$ (6)

(B) CO_2 activation:

(i) $CO_2^* \rightarrow CO^* + O^*$ (7)

(ii) $CO_2^* + H^* \rightarrow CO^* + OH^*$ (8)

(iii) $CO_2^* + O_{v-1} \rightarrow CO^* + O_v$ (9)

(iv) $CO_2^* + La_2O_3 \rightarrow La_2O_2CO_3$ (10)
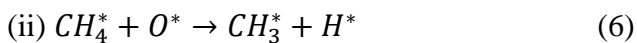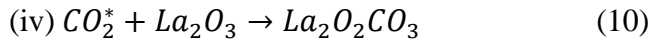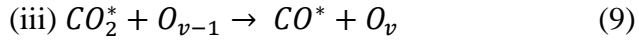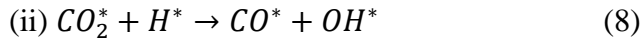
The activation energy for CH_4 and CO_2 range between 29–117 kJ/mol and 33–92 kJ/mol over Ni catalysts respectively [51]. Table 1.2 lists some of activation energies for CH_4 and CO_2 over Ni catalysts. Discrepancies in activation energy of CH_4 and CO_2 over various catalysts could be attributed to active metal dispersion, particle size and metal-support interaction [34].

Table 1.2. Activation energies for DRM over Ni based catalysts

Catalyst	Reaction Temperature (˚C)	E_a (kJ/mol)		Reference
		CH_4	CO_2	
Ni/Al$_2$O$_3$	550–650	31.1	40.5	[122]
Ni-CeO$_2$/MgAlO	450–550	78.7	59.6	[123]
Ce$_{0.7}$La$_{0.2}$Ni$_{0.1}$O$_{2-\delta}$	600–750	70.5	71	[124]
Ni/TiO$_2$	400–550	108.9	87.9	[125]
Ni/CeO$_2$	400–500	49.8	50.8	[116]

1.3.3.2 DRM mechanism and rate expression modelling

Reaction mechanism in DRM is mainly based on Langmuir–Hinshelwood–Hougen–Watson (LHHW) or Eley–Rideal (ER) models [127]. LHHW model formalism is based upon following 3 steps: a) adsorption of reactants, b) surface reaction, c) desorption of products. Generally, it is

assumed that one intermediate elementary step is slow and rate determining While other reaction steps are quasi-equilibrated. However, incorporating catalyst deactivation rate into reaction rate equation would modify LHHW model and could be shown by following equation.

$$r = k(T) \int_{t_0}^{t} r_d \, dt \, [CH_4]^a [CO_2]^b$$

Where, r is reaction rate, r_d is deactivation rate, k(T) is rate constant as a function of reaction temperature, and $[CH_4]^a$ $[CO_2]^b$ is pressure of reactants.

In ER model, one reactant is adsorbed on active site whereas other reactant remains in gas phase. The reaction between associatively adsorbed species and gas phase molecule is considered as rate determining step (RDS) [127].

Generally, the reaction mechanism over Ni based catalysts in DRM is based on LHHW model and involves following elementary reactions. 1) CH_4 is adsorbed and activated on Ni^0 sites. Carbon or hydrogen-containing carbon species (CH_x) are produced. 2) CO_2 is dissociated to CO^* and O^*. O^* species react with H^* to form OH^*. 3) CH_xO species form at metal-support interface by reaction between CH_x and OH^*. 4) CH_xO decomposes to CO and H_2.

Reaction conditions and nature of catalyst might attribute to inconsistency in determining reaction rate model [127]. In most of the mechanistic and kinetic studies over Ni catalysts, CH_4 dissociation has been suggested as slow and rate determining step (RDS) [123,124,128]. Besides CH_4 dissociation, decomposition of CH_xO was also shown to be RDS [126]. For Ni catalysts supported over La_2O_3, Verykios et al. [103,104] used SSITKA technique and reported that methane decomposition on Ni sites and surface reaction between carbon and $La_2O_2CO_3$ as RDS. DRM mechanism and rate determining step (RDS) based on LHHW model are discussed below.

Case 1: *CH₄ decomposition as RDS:* Han et al. [128] applied *in-situ* DRIFTS analysis to probe reaction mechanism over Ni-Mg/Hydrochar catalyst between 700°C–850°C. The increase in CH_4 and CO_2 conversion led to the increase of OH^*. They proposed that activation of CO_2 would occur via formation of H^* from CH_4 decomposition, and OH^* species formed by dissociation of intermediate formate ($HCOO^*$) oxidized coke. When CH_4 dissociation was suggested as rate determining step (RDS), the following steps were proposed, shown in equations (11–17).

I: Activation and dissociation of CH_4 on Ni sites to form C^* and H_2.

$$CH_4 + * \overset{K_1}{\leftrightarrow} CH_4^* \qquad\qquad (11)$$

$$CH_4^* + 4* \overset{k_2}{\leftrightarrow} C^* + 4H^* \qquad\qquad (12)$$
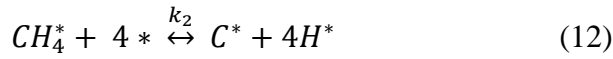
II: Adsorption and thereby dissociation of CO_2 by H^* species formed from CH_4 decomposition.

$$CO_2 + * \overset{K_3}{\leftrightarrow} CO_2^* \qquad\qquad (13)$$

$$CO_2^* + H^* \overset{K_4}{\leftrightarrow} CO^* + OH^* \qquad\qquad (14)$$
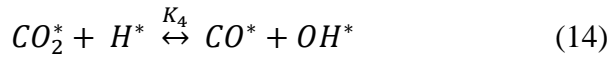
III: Oxidation of C^* by OH^* species formed by reaction between CO_2^* and H^*.

$$C^* + OH^* \overset{K_5}{\leftrightarrow} CO^* + H^* \qquad\qquad (15)$$
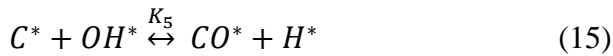
IV: Desorption of CO^* and H^* to CO(g) and H_2(g).

$$2H^* \overset{K_6}{\leftrightarrow} H_2 + 2* \qquad\qquad (16)$$

$$CO^* \overset{K_7}{\leftrightarrow} CO + * \qquad\qquad (17)$$

Therefore, the rate expression was derived as

$$r_{CH_4} = K_1 k_2 [CH_4] \left(\frac{[C_{MT}]}{M} \right)^5 \qquad (18)$$

$$Where, M = 1 + K_1[CH_4] + K_3[CO_2] + \frac{[CO]}{K_7} + \left(\frac{[H_2]}{K_6} \right)^{0.5} + \frac{[CO]^2}{K_3 K_4 K_5 K_7{}^2 [CO_2]} + \frac{K_3 K_4 K_5 K_7 [CO_2] [H_2]^{0.5}}{[CO][K_6]^{0.5}}$$

Case 2. *CH$_x$O decomposition as RDS:* Previous studies [123,124,128] showed that CH$_4$ dissociation controls reaction kinetics during DRM. However, Bradford and Vannice proposed that CH$_4$ adsorption and dissociation step is rather reversible over Ni/TiO$_2$ and Ni/MgO [126]. Carbon formed from CH$_4$ decomposition has higher reactivity than CH$_x$ species. H$_2$ addition in the feed increased CH$_4$ concentration which suggested that CH$_4$ dissociation could be reversible. Reaction between CH$_x$ and OH* species is considered as the free-radical reaction, thus no activation barrier would occur for formation of CH$_x$O in gas phase. Contrarily, decomposition of CH$_x$O in the gas phase revealed activation barrier about 71–339 kJ/mol. Thus, steps shown in equation (20–24,26) are considered as quasi-equilibrated while steps in equation (19) and (25) would account for kinetic rate expression [126].

$$CH_4 + * \overset{K_1}{\leftrightarrow} CH_x^* + \left(\frac{4-x}{2} \right) H_2 \qquad (19)$$

$$2 \left[CO_2 + * \overset{K_2}{\Leftrightarrow} CO_2^* \right] \qquad (20)$$

$$H_2 + 2 * \overset{K_3}{\Leftrightarrow} 2H^* \qquad (21)$$

$$2 \left[CO_2^* + H^* \overset{K_4}{\Leftrightarrow} CO^* + OH^* \right] \qquad (22)$$

$$OH^* + H^* \overset{K_5}{\Leftrightarrow} H_2O + 2 * \qquad (23)$$

$$CH_x^* + OH^* \overset{K_6}{\Leftrightarrow} CH_x^*O + H^* \qquad (24)$$

$$CH_x^*O \xrightarrow{k_7} CO^* + \left(\frac{x}{2}\right)H_2 \qquad (25)$$

$$3\left[CO^* \overset{K_8}{\Leftrightarrow} CO + *\right] \qquad (26)$$
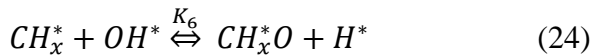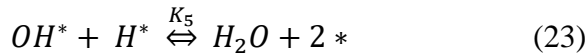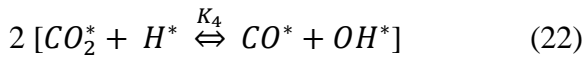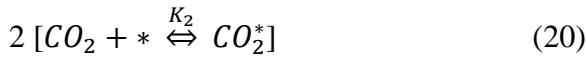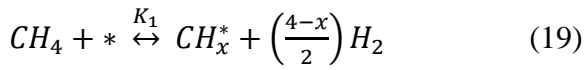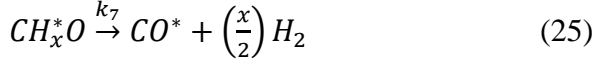
$$r_{CH_4} = \frac{K_1 P_{CH_4} P_{CO_2}}{\left(\frac{K_8}{k_7 K_2 K_4 K_6}\right)P_{CO}P_{H_2}^{(4-x)/2} + \left[1 + \left(\frac{K_1}{k_7}\right)P_{CH_4}\right]P_{CO_2}} \qquad (27)$$

Case 3. *CH_4 decomposition and C gasification by CO_2 adsorbed on catalyst as RDS:* $La_2O_2CO_3$ species are formed upon CO_2 adsorption because the strong interaction between CO_2 and basic La_2O_3. For Ni/La_2O_3 catalysts, Verykios et al. [103,104] showed that oxycarbonate species participate in the gasification of coke. On the basis of SSITKA technique, coke gasification by oxycarbonate was suggested as the RDS. Additionally, small quantities of reversibly adsorbed CH_4 were also detected. It indicated that CH_4 dissociation could be considered as slow and kinetically relevant step. Conclusively, CH_4 dissociation and carbon gasification were suggested to be RDS in DRM over Ni/La_2O_3. The sequence of reaction mechanism and rate equation is shown in steps (28–31) and 32 respectively.

$$CH_4 + * \overset{K_1}{\leftrightarrow} CH_4^* \qquad (28)$$

$$CH_4^* \xrightarrow{k_2} C^* + 2H_2 \qquad (29)$$

$$CO_2 + La_2O_3 \overset{K_3}{\leftrightarrow} La_2O_2CO_3 \qquad (30)$$

$$La_2O_2CO_3 + C^* \xrightarrow{k_4} 2CO + La_2O_3 + * \qquad (31)$$
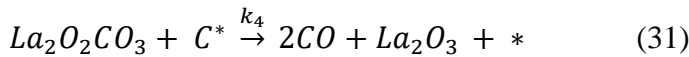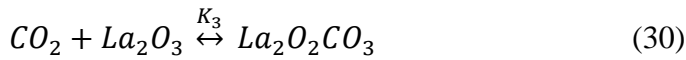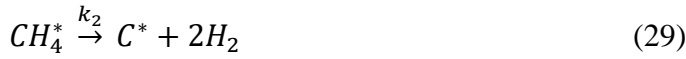
$$r_{CH_4} = \frac{K_1 k_2 K_3 k_4 P_{CH_4} P_{CO_2}}{K_1 k_2 K_3 P_{CH_4} P_{CO_2} + K_1 k_2 P_{CH_4} + K_3 k_4 P_{CO_2}} \qquad (32)$$

Case 4. E-R Model.

Few studies showed that reaction mechanism over Ni catalyst follow ER model. kinetic study in DRM over Ni/Al_2O_3 catalyst showed that CH_4 activates and dissociates on active Ni sites according to equation (33). The rate expression shown below was derived considering that reaction between CH_x species and gas phase CO_2 is RDS [127].

$$CH_4 + * \xleftrightarrow{K_{CH_4}} CH_x^* + \left(\frac{4-x}{2}\right)H_2 \qquad (33)$$

$$CH_x^* + CO_2 \xrightarrow{k_1} 2CO + H_2 + * \qquad (34)$$
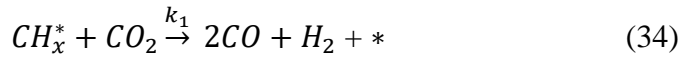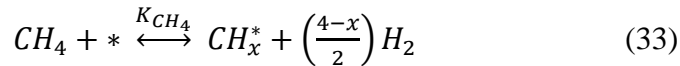
$$r_{CH_4} = \frac{k_1 K_{CH_4}\left(P_{CH_4}P_{CO_2} - \frac{P_{CO}^2 P_{H_2}^2}{k_1}\right)}{1 + K_{CH_4}P_{CH_4}}$$

1.3.4 Catalyst Deactivation

Catalyst deactivation refers to loss of catalytic activity with time on stream during reaction run. Often, catalyst deactivation during DRM is associated with carbon deposition, active metal sintering and/or sulfur poisoning [34,129]. Fig. 1.9 shows catalyst deactivation mechanisms.

1.3.4.1 Carbon deposition

Carbon deposition has been suggested as primary reason for catalyst deactivation in DRM [129]. Coke formation mainly occurs through CH_4 decomposition and/or CO disproportionation reaction. Thermodynamically, CH_4 decomposition contributes to carbon deposition under low reaction temperature (< 650˚C). While, CO disproportionation is favored under high operating

pressure (> 1atm) [24,34,100]. Operating temperature above 750°C is suggested to avoid the coke

formation.

A)

B)

C)
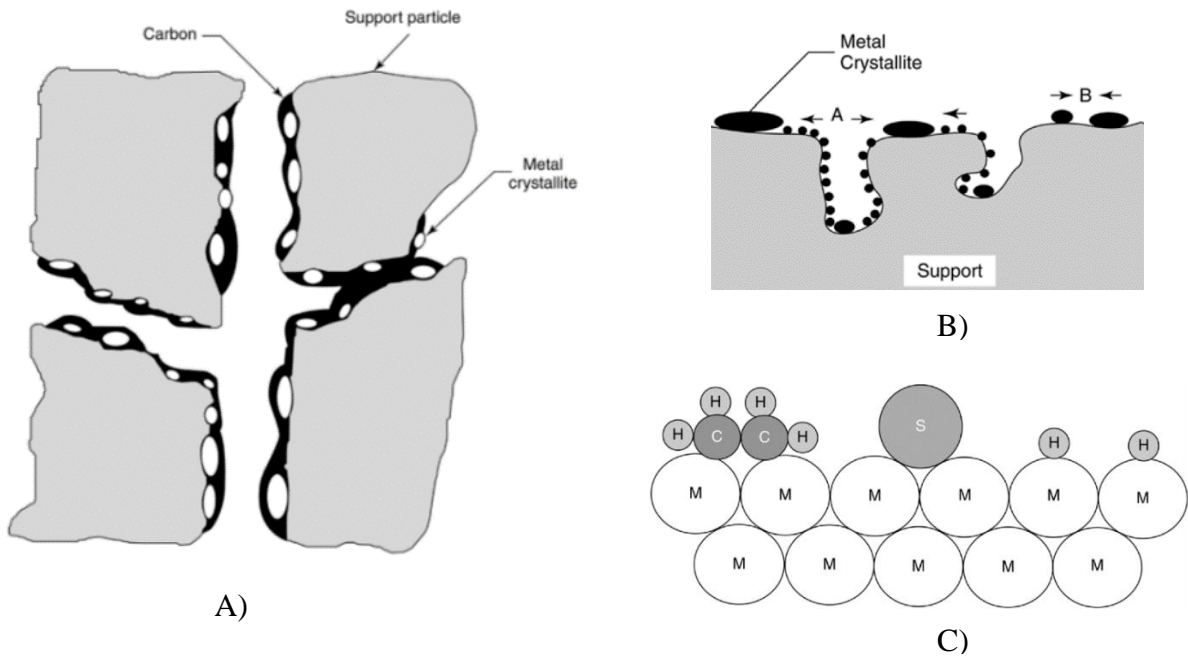
Fig.1.9. Catalyst deactivation mechanisms: A) Carbon deposition, B) Metal Sintering, C) Sulfur

poisoning, reproduced from [129].
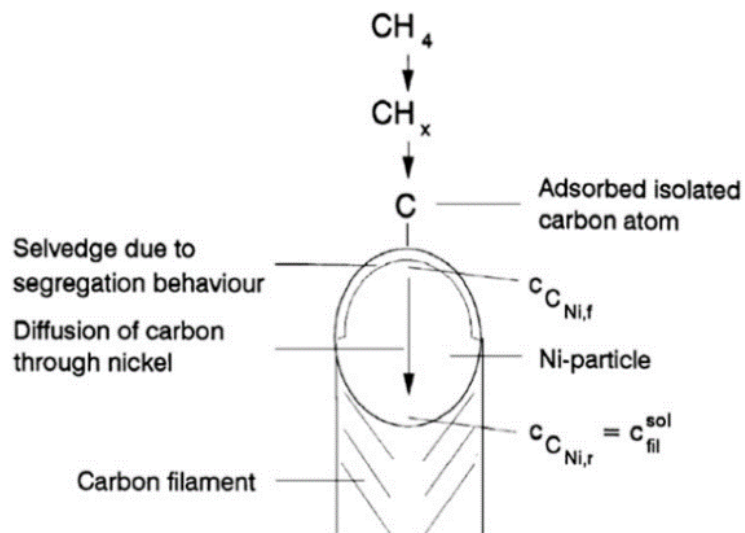
Fig.1.10. Schematic of carbon filament formation, reproduced from [130].

33

The growth of carbon filaments has been recognized as a three step deposition–diffusion–precipitation process [16,130]. As shown in Fig.1.10, upon dissociation of hydrocarbon on Ni surface, hydrogen is released and carbon dissolves in Ni forming a uniform layer. With increase in rate of hydrocarbon decomposition, carbon formed diffuses through Ni particle to the support side and precipitates at metal-support interface. When rate of carbon formation exceeds rate of diffusion and precipitation, formation of carbon filaments begins and gradually occupies the active Ni sites [130]. The type of carbon formed during DRM could differ in morphology, reaction temperature, type of metal/promoter and support [34]. The carbon formed as a result of CH_4 decomposition and CO disproportionation could be amorphous, encapsulating and/or graphitic [16,97]. Catalyst stability depends strongly on the oxidation of such carbon species. For example, oxidation of amorphous carbon occurs below 500˚C. It is thus suggested that amorphous carbonaceous does not contribute towards catalyst deactivation [58,131]. When rate of amorphous carbon formation increases than its gasification, gradual carbon builds up and transforms to graphite. Graphite type of carbon are polynuclear aromatic compounds that show resistance to gasification with either oxygen or hydrogen [130]. It has been demonstrated that graphitic carbon gasifies above 600˚C and thus, may contribute in catalyst deactivation [131].

Carbon deposition during DRM could be inhibited or controlled through several approaches demonstrated in the literature. One of them could be controlling size and dispersion of Ni nanoparticles [132]. Specifically, coke formation is more severe over large Ni ensembles [107]. Singha et al. [132] demonstrated that addition of 4.3wt% MgO to 4.8wt% Ni/ZnO catalyst increased dispersion of Ni nanoparticles from 7.3% to 19.6%. Amount of carbon deposited over 4.8Ni–4.3MgO/ZnO was about 0.2 wt% only after 100 h DRM test at 800˚C. While, 4.8Ni/ZnO showed 13 wt% coke deposits.

Besides controlling size and dispersion of Ni nanoparticles, addition of transition metals to Ni including Fe, Co, Cu or Mn could also prove beneficial to control coke formation. For example, Fan et al. [18] showed that role of Co in Ni-Co alloy catalysts was to promote gasification of carbon species during DRM. Specifically, owing to high oxophilicity of Co, enhanced dissociative adsorption of CO_2 to CO and O^* was facilitated.

Promotional effect of Fe addition to Ni catalysts in coke suppression has been discussed in literatures [83-86]. The role of Fe was attributed to its redox properties in Ni-Fe/$MgAl_2O_4$ catalysts. Fe^0 formed by reduction was oxidized to FeO_x during DRM. Coke formed from CH_4 cracking was then oxidized by lattice oxygen from FeO_x. For MgO supported Ni-Fe alloy catalysts, it was shown that addition of Fe caused formation of small Ni ensembles [90]. Consequently, DRM was favored and CH_4 decomposition was inhibited over small Ni ensembles in Ni-Fe/MgO. Moreover, addition of Fe also altered the type of carbon deposits from refractory to soft–carbons which could be easily gasified by CO_2 during DRM [90].

Alloying 25–45 % Cu with Ni also suppressed coke formation effectively [97]. The role of Cu was suggested to occupy edge and kink sites of Ni^0 which are active sites for CH_4 decomposition. Secondly, addition of Cu enhanced the formation of O^* species through CO_2 dissociation. O^* species derived from CO_2 assisted in coke gasification. Strong metal–support interaction induced by MnO addition to Ni-Co perovskites provided stability by inhibiting growth of Ni crystals [133].

Tuning the concentration of surface oxygen species of reducible supports including CeO_2, TiO_2, ZrO_2 could decrease coke deposits in DRM [17,134,135]. Substituting 20 atom-% CeO_2 with Ti^{4+} and Pr^{3+} dopants in the support could effectively suppress coke formation in Ni/CeO_2 catalysts [135,136]. Introducing Ti^{4+} and Pr^{3+} as dopants in CeO_2 support increased concentration of surface oxygen species. O^* species from the support actively participated in coke removal forming oxygen

35

vacant site. Simultaneously, CO_2 activation was also enhanced on vacant oxygen sites forming CO and O^*. Increasing basicity of support could be also beneficial in coke inhibition. Specifically, addition of alkaline earth metal oxides including MgO, CaO or SrO may enhance adsorption of mildly acidic CO_2 [137-139]. Increasing CO_2 adsorption facilitates CO_2 dissociation to CO and O^*. While O^* species could assist oxidation of carbon thereby preventing catalyst deactivation.

Table 1.3. Overview of coke deposition as a function of reaction temperature and CH_4 conversion over Ni catalysts

Catalyst	CH_4 Conversion (%)	Coke deposition (wt%)	Reaction Temperature (°C)	Ref
17wt%Ni-5wt%Zr/MgAlO	32	40.7	550	[140]
5wt%Ni/MCM-41	75	4.4	700	[141]
2.5wt%Ni+2.5wt%Co/Al$_2$O$_3$-ZrO$_2$	67.3	5	700	[142]
3.6wt%Ni@SiO$_2$	87	0.7	750	[143]
12wt%Ni/MgAlO	87	4	750	[144]
4.8wt%Ni-4.3wt%MgO/ZnO	98.8	0.2	800	[132]
4.5wt%Ni/Zr-CeO$_2$	42	13.6	800	[145]
5wt% Ni/CeO$_2$-SiO$_2$	97	9.9	800	[146]

Table 1.3 shows carbon deposition over supported Ni catalysts in DRM between 550°C–800°C temperature. As coke deposition mainly occur from CH_4 decomposition, activity in terms of CH_4 conversion has been reported in Table 1.3. Thermodynamically, coke formation is favored at low temperature (< 650°C). While, effective dissociation of CO_2 to CO and O^* above 650°C may contribute towards enhanced coke resistance in DRM. For 17wt%Ni-5wt%Zr/MgAlO catalyst, 40.7 wt% coke deposits were estimated [140]. Increasing reaction temperature would decrease coke deposition. For example, monometallic Ni/MCM-41 [141] is better catalyst compared to bimetallic Ni-Co/Al$_2$O$_3$-ZrO$_2$ [142] in terms of coke resistance and activity at 700°C. Similarly, at 750°C, 3.6 wt%Ni@SiO$_2$ [143] showed lower coke deposits than 12 wt%Ni/MgAlO [144] for

same CH_4 conversion. 4.8wt%Ni – 4.3wt% MgO/ZnO [132] catalyst was superior in catalytic activity and coke resistance at 800˚C. The differences in carbon deposition could be attributed to Ni loading, particle size and dispersion. Thus, a balance between carbon formation and carbon gasification is essential for stable DRM operation.

1.3.4.2 Sintering

Sintering refers to loss of active metal surface area by growth of metal nanoparticles during catalysis [147]. Generally, the growth of nanoparticles is associated with two mechanism: a) particle migration and coalescence (PMC), b) Ostwald ripening (OR). Particle migration involves mobility of metal particles in Brownian-like motion. Subsequently, nanoparticles come in close proximity with each other leading to coalescence and particle size growth. Ostwald ripening refers to interparticle migration of mobile molecular species to support surface. Herein, the particle growth is driven by differences in surface free energies of adatoms on catalyst surface. It is suggested that sintering mechanism might change during catalysis depending upon size of nanoparticles. Specifically, when metal particles are very small in the early stages of catalysis, sintering proceeds through PMC. When metal nanoparticles become effectively large and immobile, Ostwald ripening dominates [147]. Schematic of catalyst deactivation due to sintering is shown in Fig.1.9 (B).

One effective approach to control and/or inhibit sintering is to increase metal-support interaction. Zhang et al. [108] synthesized Ni/SiO_2 catalysts by one-pot hydrothermal approach. This synthesis approach facilitated formation of highly dispersed ultra-small Ni nanoparticles (3.2 nm). H_2–TPR analysis demonstrated that strong metal-support interaction (SMSI) existed between Ni and SiO_2. SMSI effect inhibited sintering and growth of Ni nanoparticles for 30 h TOS DRM [108]. Recently, it was shown that surface engineering of defect induced boron nitride were

exceptional support for anti-sintering of Ni nanoparticles [111,118,148]. TEM and H_2–TPR analysis showed that Ni dispersion was improved in presence of defect sites of boron nitride. While, SMSI effect would inhibit sintering of Ni nanoparticles.

1.3.4.3 Sulfur Poisoning

Besides coking and sintering, catalyst deactivation might also be attributed to sulfur poisoning. It has been reported that for reforming reactions, H_2S is commonly recognized as catalyst poison [129]. Typically, H_2S chemisorbs on metal surface according to equation (35), thereby deactivating the catalyst by formation of metal–S bond. Conceptual model of catalyst deactivation by sulfur poisoning is shown in Fig. 1.9 (C). Catalyst poisoning has been shown to occur by following 3 steps: a) dissociative adsorption of H_2S on active metal site, resulting in blockage of one-three to one-fourth topside metal atoms by sulfur atoms, b) Electronic modification of active metal atoms, thereby disabling the tendency of active metal atoms to adsorb and/or dissociate reactants, c) reconstruction of catalyst surface causing alterations in catalytic properties [129].

$$H_2S + Metal \rightarrow Metal - S + H_2 \qquad (35)$$
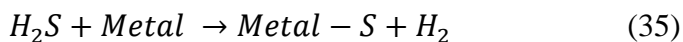
Resistance of Ni based reforming catalysts against sulfur poisoning could be improved by addition of Rh. Theofanidis et al. [149] showed that addition of Rh in $Ni/MgAl_2O_4$ catalysts in the molar ratio of Ni:Rh as ~ 40:1 should be sufficient enough to inhibit catalyst poisoning. Specifically, addition of Rh formed Ni-Rh alloy which refrained the dissociation of H_2S to SH^* and H^* species during reforming. Compared to $Ni/MgAl_2O_4$ catalysts, Ni-Rh alloy increased the activation barrier of H_2S dissociation, thereby preventing catalyst deactivation from sulfur poisoning.

1.4 Rationales and Objectives

Owing to increasing greenhouse gases emissions and the urge to potentially utilize natural gas resources, it is necessary to convert CH_4 into valuable feedstock for synthesis of chemicals and fuels. Utilization of natural gas resources including CH_4 would also serve as an alternative to depleting oil resources. The rationale for this project is to address conversion of CH_4 using a soft oxidant such as CO_2. Employment of CO_2 along with CH_4 (DRM) would require extremely high temperatures (>800˚C) to achieve equilibrium conversions. However, DRM could also be operated at low temperatures < 600˚C to make process economical. In this context, membrane reactors or reactors operated by solar energy could be employed for low temperature DRM. Thus, this dissertation focuses on low temperature dry reforming of methane. Nevertheless, thermodynamically coke formation becomes more prominent below 600˚C. Therefore, a reaction temperature of 550˚C is chosen for studying low temperature DRM. The objective of the present research is to eliminate coke formation at low temperature DRM using inexpensive Ni-based catalysts. Addition of abundant metals to Ni catalysts such as Fe eliminates the choice of precious metals as promoters. Thus, bimetallic Ni-Fe catalysts are synthesized to study DRM. This study focuses on different synthesis approaches for preparation of bimetallic Ni-Fe catalysts supported over TiO_2. Secondly, modification of catalyst support using a redox CeO_2 is elucidated for low temperature DRM. Physical and chemical properties of catalysts are investigated in detail by applying various catalyst characterization techniques. Analysis of coke formation in spent Ni-Fe catalysts after DRM is presented. Finally, the role of Fe in coke removal and syngas formation mechanism is unraveled.

1.5 References

[1] M. Maestri, D. G. Vlachos, A. Beretta, G. Groppi, E.Tronconi, AIChE J. 55 (2009) 993–1008.

[2] A. Naidja, C. R. Krishna, T. Butcher and D. Mahajan, Prog. Energ. Combust. 29 (2003) 155–191.

[3] M.V. Iyer, L.P. Norcio, E.L. Kugler, D.B. Dadyburjor, Ind. Eng. Chem. Res. 42 (2003) 2712-2721.

[4] Z. Boukha, C. Jiménez-González, B. de Rivas, J.R. González-Velasco, J.I. Gutiérrez-Ortiz, R. López Fonseca, Appl. Catal. B 158–159 (2014) 190-201.

[5] https://www.eia.gov/naturalgas/crudeoilreserves/

[6] U. Izquierdo, V. L. Barrio, J. Requies, J. F. Cambra, M. B. Guemez, P. L. Arias, Int. J. Hydrogen Energy 38 (2013) 7623–7631.

[7] https://www.eia.gov/energyexplained/biomass/landfill-gas-and-biogas.php

[8] https://www.ch4global.com/

[9] N. Kumar, M. Shojaee, J.J. Spivey, Curr. Opin. Chem. Eng. 9 (2015) 8-15.

[10] J.R.H. Ross, Catal. Today 100 (2005) 151-158.

[11] A. Caballero, P.J. Perez, Chem. Soc. Rev. 42 (2013) 8809-8820.

[12] S.D. Angeli, L. Turchetti, G. Monteleone, A.A. Lemonidou, Appl. Catal. B 181 (2016) 34-46.

[13] E.T. Kho, J. Scott, R. Amal, Chem. Eng. Sci. 140 (2016) 161-170.

[14] M.D. Salazar-Villalpando, D.A. Berry, T.H. Gardner, Int. J. Hydrogen Energy 33 (2008) 2695-2703.

[15] A. Scarabello, D. Dalle Nogare, P. Canu, R. Lanza, Appl. Catal. B 174–175 (2015) 308-322.

[16] D. Li, S. Xu, K. Song, C. Chen, Y. Zhan, L. Jiang, Appl. Catal. A 552 (2018) 21–29.

[17] M. Zhang, J. Zhang, Y. Wu, J. Pan, Q. Zhang, Y. Tan, Y. Han, Appl. Catal. B 244 (2019) 427–437.

[18] A. Tsoukalou, Q. Imtiaz, S.M. Kim, P.M. Abdala, S. Yoon, C.R. Müller, J. Catal. 343 (2016) 208–214.

[19] X. Fan, Z. Liu, Y.A. Zhu, G. Tong, J. Zhang, C. Engelbrekt, J. Ulstrup, K. Zhu, X. Zhou, J. Catal. 330 (2015) 106–119.

[20] Y. Xia, N. Lu, J. Li, N. Jiang, K. Shang, Y. Wu, J. CO_2 Util. 37 (2020) 248-259.

[21] J.R. Rostrup-Nielsen, J. Sehested, J.K. Nørskov, Adv. Catal. 47 (2002) 65-139.

[22] Y. Yan, Z. Zhang, L. Zhang, X. Wang, K. Liu, Z. Yang, Int. J. Hydrogen Energy 40 (2015) 1886-1893.

[23] A. V. P. Lino, C. B. Rodella, E. M. Assaf, J. M. Assaf, Int. J. Hydrogen Energy 45 (2020) 8418-8432.

[24] S. Arora, R. Prasad, RSC Adv. 6 (2016) 108668-108688.

[25] M.S. Fan, A.Z. Abdullah, S. Bhatia, ChemCatChem 1 (2009) 192-208.

[26] Y. Xu, D. Liu, X. Liu, Appl. Catal. A 552 (2018) 168-183.

[27] M.K. Nikoo, N. A. S. Amin, Fuel Process. Technol. 92 (2011) 678-691.

[28] A. C. D. Freitas, R. Guirardello, J. CO_2 Util. 7 (2014) 30-38.

[29] G. A. Olah, A. Goeppert, M. Czaun, G.K.S. Prakash, J. Am. Chem. Soc. 135 (2013) 648-650

[30] G. A. Olah, A. Goeppert, M. Czaun, T. Mathew, R.B. May, G.K.S. Prakash, J. Am. Chem. Soc. 137 (2015) 8720-8729.

[31] J. Yoo, Y. Bang, S. J. Han, S. Park, J. H. Song, I. K. Song, J. Mol. Catal. A 410 (2015) 74-80.

[32] C. Song, W. Pan, Catal. Today 98 (2004) 463-484.

[33] X. Li, D. Li, H. Tian L. Zeng, Z. J. Zhao, J. Gong, Appl. Catal. B 202 (2017) 683-694.

[34] D. Pakhare, J. J. Spivey, Chem. Soc. Rev. 7 (2014) 7813-7837.

[35] J.A. Moulijn, A.E. Diepen, F. Kapteijn, Appl. Catal. A 212 (2001) 3-16.

[36] H. Liu, D. Wierzbicki, R. Debek, M. Motak, T. Grzybek, P. D. Costa, M. E. Gálvez, Fuel 182 (2016) 8–16.

[37] H. S. Whang, M. S. Choi, J. Lim, C. Kim, I. Heo, T. S. Chang, H. Lee, Catal. Today 293–294 (2017) 122–128.

[38] S. A. Singh, G. Madras, Appl. Catal. A 518 (2016) 102–114.

[39] C. C. Chonga, S. N. Bukharia, Y. W. Chenga, H. D. Setiabudi, A. A. Jalil, C. Phalakornkule, Appl. Catal. A 584 (2019) 117174

[40] K. Takanabe, K. Nagaoka, K. Nariai, K. Aika, J. Catal. 230 (2005) 75-85.

[41] D. Li, R. Li, M. Lu, X. Lin, Y. Zhan, L. Jiang, Appl. Catal. B 200 (2017) 566-577.

[42] Z. Liu, F. Zhang, N. Rui, X. Li, L. Lin, L. E. Betancourt, D. Su, W. Xu, J. Cen, K. Attenkofer, H. Idriss, J. A. Rodriguez, S. D. Senanayake, ACS Catal. 9 (2019) 3349-3359.

[43] S. Damyanova, B. Pawelec, K. Arishtirova, M. V. M. Huerta, J. L. G. Fierro, Appl. Catal. B 89 (2009) 149-159.

[44] R. O. Fonseca, R. C. Rabelo-Neto, R. C. C. Simoes, L. V. Mattos, F. B. Noronha, Int. J. Hydrogen Energy 45 (2020) 5182-5191.

[45] F. Wang, L. Xu, J. Zhang, Y. Zhao, H. Li, H. X. Li, K. Wu, G. Q. Xu, W. Chen, Appl. Catal. B 180 (2016) 511-520.

[46] S. C.P. Maina, A. D. Ballarini, J. I. Vilella, S. R. Miguel, Catal. Today 344 (2020) 129-142.

[47] Y. Li, J. Jiang, C. Zhu, L. Li, Q. Li, Y. Ding, W. Yang, Materials 11 (2018) 172.

[48] I. V. Yentekakis, G. Goula, M. Hatzisymeon, I. B. Argyropoulou, G. Botzolaki, K. Kousi, D. I. Kondarides, M. J. Taylor, C. M. A. Parlett, A. Osatiashtiani, G. Kyriakou, J. P. Holgado, R. M. Lambert, Appl. Catal. B 243 (2019) 490-501.

[49] R. K. Singha, A. Yadav, A. Shukla, M. Kumar, R. Bal, Catal. Commun. 92 (2017) 19-22.

[50] L. Yue, J. Li, C. Chen, X. Fu, Y. Gong, X. Xia, J. Hou, C. Xiao, X. Chen, L. Zhao, G. Ran, H. Wang, Fuel 218 (2018) 335-341.

[51] M. C. J. Bradford, M. A. Vannice, Catal. Rev. 41 (1999) 1-42.

[52] J. H. Kim, D. J. Suh, T. J. Park, K. L. Kim, Appl. Catal. A 197 (2000) 191–200.

[53] R. Debek, M. E. Galvez, F. Launay, M. Motak, T. Grzybek, P. D. Costa, Int. J. Hydrogen Energy 41 (2016) 11616-11623.

[54] H. Wang, X. Dong, T. Zhao, H. Yu, M. Li, Appl. Catal. B 245 (2019) 302–313.

[55] S. Ali, M. M. Khader, M. J. Almarri, A. G. Abdelmoneim, Catal. Today 343 (2020) 36-47.

[56] P. Littlewood, S. Liu, E. Weitz, T. J. Marks, P. C. Stair, Catal. Today 343 (2020) 18-25.

[57] D. Shen, M. Huo, L. Li, S. Lyu, J. Wang, X. Wang, Y. Zhang, J. Li, Catal. Sci. Technol. 10 (2020) 510–516.

[58] M. Shah, A. Bordoloi, A. K. Nayak, P. Mondal, Fuel Process. Technol. 192 (2019) 21-35.

[59] Y. Guo, J. Lu, Q. Liu, X. Bai, L. Gao, W. Tu, Z. Wang, Catal. Commun. 116 (2018) 81-84.

[60] W. O. Alabi, K. O. Sulaiman, H. Wang, Chem. Eng. J. 390 (2020) 124486.

[61] K. Nagaoka, K. Takanabe, K. Aika, Appl. Catal. A 255 (2003) 13-21.

[62] J. Park, S. Yeo, I. Heo, T. Chang, Appl. Catal. A 562 (2018) 120-131.

[63] F. Menegazzo, M. Signoretto, F. Pinna, P. Canton, N. Pernicone, Appl. Catal. A 439 (2012) 80–87.

[64] I. Luisetto, C. Sarno, D. Felicis, F. Basoli, C. Battocchio, S. Tuti, S. Licoccia, E. D. Bartolomeo, Fuel Process. Technol. 158 (2017) 130–140.

[65] H. Cheng, S. Feng, W. Tao, X. Lu, W. Yao, G. Li, Z. Zhou, Int. J. Hydrogen Energy 39 (2014) 12604-12612.

[66] Z. Hou, P. Chen, H. Fang, X. Zheng, T. Yashima, Int. J. Hydrogen Energy 31 (2006) 555-561.

[67] Z. Bian, S. Das, M. H. Wai, P. Hongmanorom, S. Kawi, ChemPhysChem 18 (2017) 3117 – 3134.

[68] T. D. Gould, M. M. Montemore, A. M. Lubers, L. D. Ellis, A. W. Weimer, J. L. Falconer, J. W. Medlin, Appl. Catal. A 492 (2015) 107-116.

[69] L. Li, L. Zhou, S. O. Chikh, D. H. Anjum, M. B. Kanoun, J. Scaranto, M. N. Hedhili, S. Khalid, P. V. Laveille, L. D'Souza, A. Clo, J. M. Basset, ChemCatChem 7 (2015) 819-829.

[70] X. Yu, F. Zhang, N. Wang, S. Hao, W. Chu, Catal. Lett. 144 (2014) 293–300.

[71] C. Crisafulli, S. Scirè, S. Minicò, L. Solarino, Appl. Catal. A 225 (2002) 1–9.

[72] C. Crisafulli, S. Scire, R. Maggiore, S. Minico, S. Galvagno, Catal. Lett. 59 (1999) 21–26.

[73] A. S. Bobin, V. A. Sadykov, V. A. Rogov, N. V. Mezentseva, G. M. Alikina, E. M. Sadovskaya, T. S. Glazneva, N. N. Sazonova, M. Yu Smirnova, S. A. Veniaminov, C. Mirodatos, V. Galvita, G. B. Marin, Top. Catal. 56 (2013) 958-968.

[74] M. E. Rivas, J. L. G. Fierro, M. R. Goldwasser, E. Pietri, M. J. P. Zurita, A. G. Constant, G. Leclercq, Appl. Catal. A 344 (2008) 10–19.

[75] J. C. S. Wu, H. C. Chou, Chem. Eng. J. 148 (2009) 539–545.

[76] Q. Ma, J. Sun, X. Gao, J. Zhang, T. Zhao, Y. Yoneyama, N. Tsubaki, Catal. Sci. Technol. 6 (2016) 6542–6550.

[77] S. Damyanova, B. Pawelec, K. Arishtirova, J. L. G. Fierro, C. Sener, T. Dogu, Appl. Catal. B. 92 (2009) 250–261.

[78] K. Nagaoka, K. Takanabe, K. Aika, Appl. Catal. A 268 (2004) 151-158.

[79] J. Park· T. Chang, Cat. Lett. 149 (2019) 3148-3159.

[80] Y. Pang, Y. Dou, A. Zhong, W. Jiang, L. Gu, X. Feng, W. Ji, C. Au, Appl. Catal. A 555 (2018) 27-35.

[81] L. Chen, Q. Huang, Y. Wang, H. Xiao, W. Liu, D. Zhang, T. Yang, Int. J. Hydrogen Energy 44 (2019) 19878-19889.

[82] Z. Xie, B. Yan, S. Kattel, J. H. Lee, S. Yao, Q. Wu, N. Rui, E. Gomez, Z. Liu, W. Xu, L. Zhang, J. G. Chen, Appl. Catal. B 236 (2018) 280-293.

[83] S.M. Kim, P.M. Abdala, T. Margossian, D. Hosseini, L. Foppa, A. Armutlulu, W. Van Beek, A. Comas-Vives, C. Copéret, C. Müller, J. Am. Chem. Soc. 139 (2017) 1937–1949.

[84] T. Margossian, K. Larmier, S.M. Kim, F. Krumeich, C. Müller, C. Copéret, ACS Catal. 7 (2017) 6942–6948.

[85] S.A. Theofanidis, V. V. Galvita, H. Poelman, G.B. Marin, ACS Catal. 5 (2015) 3028–3039.

[86] S. A. Theofanidis, V. V. Galvita, H. Poelman, N. V. R. A. Dharanipragada, A. Longo, M. Meledina, G. V. Tendeloo, C. Detavernier, G. B. Marin, ACS Catal. 8 (2018) 5983-5995.

[87] B. Li, Y. Luo, B. Li, X. Yuan, X. Wang, Fuel Process. Technol. 193 (2019) 348-360.

[88] X. Song, X. Dong, S. Yin, M. Wang, M. Li, H. Wang, Appl. Catal. A 526 (2016) 132-138.

[89] S. M. Lima, J. M. Assaf, Catal. Lett. 108 (2006) 63-70.

[90] T. Zhang, Z. Liu, Y. Zhu, Z. Liu, Z. Sui, K. Zhu, X. Zhou, Appl. Catal. B 264 (2020) 118497.

[91] H. Ay, D. Uner, Appl. Catal. B 179 (2015) 128–138.

[92] X. Gao, Z. Tan, K. Hidajat, S. Kawi, Catal. Today 281 (2017) 250–258.

[93] Z. Bian, S. Kawi, J. CO_2 Util. 18 (2017) 345–352.

[94] H. Long, Y. Xu, X. Zhang, S. Hu, S. Shang, Y. Yin, X. Dai, J. Energy Chem. 22 (2013) 733–739.

[95] J. Xu, W. Zhou, Z. Li, J. Wang, J. Ma, Int. J. Hydrogen Energy 34 (2009) 6646–6654.

[96] J. Zhang, H. Wang, A. K. Dalai, J. Catal. 249 (2007) 300–310.

[97] K. Song, M. Lu, S. Xu, C. Chen, Y. Zhan, D. Li, C. Au, L. Jiang, K. Tomishige, Appl. Catal. B 239 (2018) 324–333.

[98] J. H. Lee, E. G. Lee, O. S. Joo, K. D. Jung, Appl. Catal. A 269 (2004) 1–6.

[99] H. W. Chen, C. Y. Wang, C. H. Yu, L. T. Seng, P. H. Liao, Catal. Today 97 (2004) 173-180.

[100] H.O. Seo, Catalysts 8 (2018) 110.

[101] S. Das, J. Ashok, Z. Bian, N. Dewangan, M. H. Wai, Y. Du, A. Borgna, K. Hidajat, S. Kawi, Appl. Catal. B 230 (2018) 220-236.

[102] C. Liang, L. Zhang, Y. Zheng, S. Zhang, Q. Liu, G. Gao, D. Dong, Y. Wang, L. Xue, X. Hu, Fuel 262 (2020) 116521.

[103] V. A. Tsipouriari, X. E. Verykios, Catal. Today 64 (2001) 83-90.

[104] V. A. Tsipouriari, X. E. Verykios, J. Catal. 187 (1999) 85-94.

[105] T. V Sagar, D. Padmakar, N. Lingaiah, P.S. Sai Prasad, Catal. Lett. 149 (2019) 2597–2606.

[106] M. Yu, Y.A. Zhu, Y. Lu, G. Tong, K. Zhu, X. Zhou, Appl. Catal. B 165 (2015) 43–56.

[107] Q. G. Yan, W. Z. Weng, H. L. Wan, H. Toghiani, R. K. Toghiani, C. U. Pittman, Appl. Catal. A 239 (2003) 43–58.

[108] Q. Zhang, T. Tang, J. Wang, M. Sun, H. Wang, H. Sun, P. Ning, Catal. Commun. 131 (2019) 105782.

[109] L. Zhang, F. Wang, J. Zhu, B. Han, W. Fan, L. Zhao, W. Cai, Z. Li, L. Xu, H. Yu, W. Shi, Fuel 256 (2019) 115954.

[110] X. Yan, T. Hu, P. Liu, S. Li, B. Zhao, Q. Zhang, W. Jiao, S. Chen, P. Wang, J. Lu, L. Fan, X. Deng, Y. X. Pan, Appl. Catal. B 246 (2019) 231-241.

[111] Y. Cao, P. Maitarada, M. Gao, T. Taketsugu, H. Li, T. Yan, L. Shi, D. Zhang, Appl. Catal. B 238 (2018) 51-60.

[112] K. Bu, S. Kuboon, J. Deng, H. Li, T. Yan, G. Chen, L. Shi, D. Zhang, Appl. Catal. B 252 (2019) 86-97.

[113] K. Li, C. Pei, X. Li, S. Chen, X. Zhang, R. Liu, J. Gong, Appl. Catal. B 264 (2020) 118448.

[114] Z. Shang, S. Li, L. Li, G. Liu, X. Liang, Appl. Catal. B 201 (2017) 302-309.

[115] S. Damyanova, B. Pawelec, R. Palcheva, Y. Karakirova, M. C. C. Sanchez, G. Tyuliev, E. Gaigneaux, J. L. G. Fierro, Appl. Catal. B 225 (2018) 240-253.

[116] M. Li, A. C. Veen, Appl. Catal. B 237 (2018) 641-648.

[117] F. Zhang, Z. Liu, X. Chen, N. Rui, L. E. Betancourt, L. Lin, W. Xu, C. Sun, A. M. M. Abeykoon, J. A. Rodriguez, J. Terzan, K. Lorber, P. Djinovic´, S. D. Senanayake, ACS Catal. 10 (2020) 3274-3284.

[118] N. Kumar, S. Kanitkar, Z. Wang, D. Haynes, D. Shekhawat, J. J. Spivey, Int. J. Hydrogen Energy 44 (2019) 4167-4176.

[119] K. Sutthiumporn, T. Maneerung, Y. Kathiraser, S. Kawi, Int. J. Hydrogen Energy 37 (2012) 11195-11207.

[120] Z. Xie, Q. Liao, M. Liu, Z. Yang, L. Zhang, Energy Convers. Manage. 153 (2017) 526-537.

[121] M. Zhang, J. Zhang, Z. Zhou, S. Chen, T. Zhang, F. Song, Q. Zhang, N. Tsubaki, Y. Tan, Y. Han, Appl. Catal. B 264 (2020) 118522.

[122] K. Li, X. Chang, C. Pei, X. Li, S. Chen, X. Zhang, S. Assabumrungrat, Z. J. Zhao, L. Zeng, J. Gong, Appl. Catal. B 259 (2019) 118092.

[123] Y. Cui, H. Zhang, H. Xu, W. Li, Appl. Catal. A 318 (2007) 79-88.

[124] J. Niu, S. E. Liland, J. Yang, K. R. Rout, J. Ran, D. Chen, Chem. Eng. J. 377 (2019) 119763.

[125] L. Pino, C. Italiano, M. Laganà, A. Vita, V. Recupero, Catal. Sci. Technol. 10 (2020) 2652-2662.

[126] M. C. J. Bradford, M. A. Vannice, Appl. Catal. A 142 (1996) 97-122.

[127] Y. Kathiraser, U. Oemar, E. T. Saw, Z. Li, S. Kawi, Chem. Eng. J. 278 (2015) 62-78.

[128] J. Han, Y. Liang, L. Qin, Y. Wang, H. Wang, F. Yu, B. Zhao, Catal. Lett. 150 (2020) 1479-1488.

[129] M. D. Argyle, C. H. Bartholomew, Catalysts 5 (2015) 145-269.

[130] A. M. Amin, E. Croiset, W. Epling, Int. J. Hydrogen Energy 36 (2011) 2904-2935.

[131] M. Shah, S. Das, A. K. Nayak, P. Mondal, A. Bordoloi, Appl. Catal. A 556 (2018) 137-154.

[132] R. K. Singha, A. Yadav, A. Agrawal, A. Shukla, S. Adak, T. Sasaki, R. Bal, Appl. Catal. B 191 (2016) 165-178.

[133] W. Y. Kim, J. S. Jang, E. C. Ra, K. Y. Kim, E. H. Kim, J. S. Lee, Appl. Catal A 575 (2019) 198-203.

[134] S. S. Kim, S. M. Lee, J. M. Won, H. J. Yang, S. C. Hong, Chem. Eng. J. 280 (2015) 433-440.

[135] C. M. Damaskinos, M. A. Vasiliades, A. M. Efstathiou, Appl. Catal. A 579 (2019) 116-129.

[136] M. A. Vasiliades, M. M. Makri, P. Djinovic´, B. Erjavec, A. Pintar, A. M. Efstathiou, Appl. Catal. B 197 (2016) 168-183.

[137] S. J. H. Rad, M. Haghighi, A. A. Eslami, F. Rahmani, N. Rahemi, Int. J. Hydrogen Energy 41 (2016) 5335-5350.

[138] S. Sengupta, G. Deo, J. CO_2 Util. 10 (2015) 67-77.

[139] B. Ghods, F. Meshkani, M. Rezaei, Int. J. Hydrogen Energy 41 (2016) 22913-22921.

[140] R. Debek, M. Motak, M.E. Galvez, T. Grzybek, P. D. Costa, Appl. Catal. B 223 (2018) 36-46.

[141] P. Frontera, A. Macario, A. Aloise, P. L. Antonucci, G. Giordano, J. B. Nagy, Catal. Today, 218–219 (2013) 18-29.

[142] A. S. A. Fatesh, J. K. A. Dahrieh, H. Atia, U. Armbruster, A. A. Ibrahim, W. U. Khan, A. E. Abasaeed, A. H. Fakeeha, Int. J. Hydrogen Energy 44 (2019) 21546-21558.

[143] F. Wang, B. Han, L. Zhang, L. Xu, H. Yu, W. Shi, Appl. Catal. B 235 (2018) 26-35.

[144] X. Lin, R. Li, M. Lu, C. Chen, D. Li, Y. Zhan, L. Jiang, Fuel 162 (2015) 271-280.

[145] I. Luisetto, S. Tuti, C. Romano, M. Boaro, E. D. Bartolomeo, J. K. Kesavan, S. S. Kumar, K. Selvakumar, J. CO_2 Util. 30 (2019) 63-78.

[146] Sudarno, S. M. Razali, N. A. Mijan, S. Sivasangar, Y.H. T. Yap, Int. J. Hydrogen Energy 44 (2019) 20738-20750.

[147] T. W. Hansen, A. T. Delariva, S. R. Challa, A. K. Datye, Acc. Chem. Res. 46 (2013) 1720-1730.

[148] K. Bu, J. Deng, X. Zhang, S. Kuboon, T. Yan, H. Li, L. Shi, D. Zhang, Appl. Catal. B 267 (2020) 118692.

[149] S. A. Theofanidis, J. A. Z. Pieterse, H. Poelman, A. Longo, M. K. Sabbe, M. Virginie, C. Detavernier, G. B. Marin, V. V. Galvita, Appl. Catal. B 267 (2020) 118691.

Chapter 2

Experimental

This chapter focuses on the details of synthesis, characterization and activity performance of Ni-Fe catalysts employed for DRM in the project. Section 2.1.1 describes about synthesis of mono and bimetallic Ni-Fe catalysts supported over TiO_2 by incipient wetness impregnation route. Literature studies on the effect of catalyst preparation on activity performance has showed enhanced metal and support interactions while employing advanced catalytic preparation approach. Section 2.1.2 describes synthesis of mono and bimetallic $Ni-Fe/TiO_2$ catalysts by hydrotalcite route. Utilization of CeO_2 as support has shown to induce SMSI effect. Thus, 20 wt% TiO_2 is replaced by CeO_2 in support material. Preparation of TiO_2-CeO_2 mixed oxide support is entailed in section 2.1.3. TiO_2-CeO_2 synthesis is followed by co-impregnation of hydrotalcite derived Ni-Fe catalyst onto mixed oxide support. Section 2.2 discusses characterization of Ni-Fe catalysts by temperature programmed reactions (TPRes), pulse CO-chemisorption, X-ray photoelectron spectroscopy (XPS), Thermogravimetric analysis-differential thermogravimetry (TGA-DTG), Raman spectroscopy and *in-situ* diffuse reflectance infrared fourier transform spectroscopy (DRIFTS) analysis. While catalytic activity performance in DRM is described in 2.3.

2.1 Catalyst synthesis

2.1.1 Ni-Fe/TiO₂ synthesis by incipient wetness impregnation

In one typical preparation, required amounts of $Ni(NO_3)_2 \cdot 6H_2O$ and/or $Fe(NO_3)_3 \cdot 9H_2O$ were dissolved separately in 10 mL D.I. water. Two aqueous solutions were simultaneously added to

P25-TiO$_2$ support. The mixture was stirred at 35˚C for 24 h. After impregnation, the slurry was dried at 95˚C to evaporate water. Dried samples were kept in vacuum oven at 95˚C overnight. As-prepared catalysts were calcined in air at 450˚C for 4 h. The total metal loading was designed as 10 wt%. Samples were labeled as Ni/TiO$_2$, Ni$_3$Fe$_1$/TiO$_2$, Ni$_1$Fe$_1$/TiO$_2$, Ni$_1$Fe$_3$/TiO$_2$ and Fe/TiO$_2$.

2.1.2 Ni-Fe/TiO$_2$ synthesis by hydrotalcite-type precursors

Bimetallic Ni-Fe catalysts derived from hydrotalcite-type precursors were synthesized by co-precipitation method. Typically, required amounts of Ni(NO$_3$)$_2$·6H$_2$O and Fe(NO$_3$)$_3$·9H$_2$O aqueous solutions were added dropwise in 0.2 M Na$_2$CO$_3$ solution under vigorous stirring at room temperature at a constant pH of 10 ± 0.5. The mixture solution was vigorously stirred for additional 30 minutes at room temperature. The precipitates were collected by centrifugation and washed with D.I. water until the pH of precipitates become ~ 7. As-synthesized Ni-Fe hydrotalcites were wet-impregnated on P25-TiO$_2$ support and stirred for 24 h at room temperature. Ni-Fe hydrotalcites/TiO$_2$ were collected by centrifugation and dried under vacuum at 95˚C for 48 h. Ni-Fe oxides/TiO$_2$ were obtained by calcining Ni-Fe hydrotalcites/TiO$_2$ in air at 450˚C for 4 h at 5˚C/min ramp rate. A similar co-precipitation procedure was followed for preparation of monometallic Ni/TiO$_2$ and Fe/TiO$_2$ catalysts. The designed total metal loading of Ni or (Ni+Fe) was 10 wt%. Samples were labelled as Ni/TiO$_2$, Ni$_3$Fe$_1$/TiO$_2$, Ni$_1$Fe$_1$/TiO$_2$, Ni$_1$Fe$_3$/TiO$_2$ and Fe/TiO$_2$.

2.1.3 Synthesis of mixed oxide TiO$_2$-CeO$_2$ support and Ni-Fe/TiO$_2$-CeO$_2$ catalyst

TiO$_2$-CeO$_2$ support (80wt%TiO$_2$ and 20 wt% CeO$_2$) was synthesized by impregnation of Ce(NO$_3$)$_3$·6H$_2$O with P25-TiO$_2$. Typically, 1.6 g of TiO$_2$ was dissolved in Ce(NO$_3$)$_3$·6H$_2$O solution and the mixture was stirred at room temperature for 4 h. The homogeneous mixture was

then dried at 120°C. As-prepared TiO_2-$Ce(NO_3)_3 \cdot 6H_2O$ was calcined in air for 4 h at 450°C to form mixed oxide TiO_2-CeO_2 support. Ni-Fe/TiO_2-CeO_2 catalyst was prepared by a method described in section 2.1.2.

2.2 Catalyst characterization

2.2.1 Temperature programmed reactions

Hydrogen–Temperature programmed reduction (H_2-TPR) was conducted in Micromeritics Autochem II 2920. Typically, 50 mg of calcined catalyst was pretreated with helium at 150°C to remove any adsorbed moisture. Subsequently, the catalyst was cooled down to room temperature with pure helium. H_2-TPR was performed using 10%H_2/Ar (30 mL/min) from room temperature to 700°C at 5°C/min ramp rate.

Methane – Temperature programmed surface reaction/Differential Thermogravimetry (CH_4-TPSR/DTG) experiments were performed in Micromeritics AutoChem II 2920 and Mettler Toledo Thermal Analyzer (TGA/DSC 1) respectively. For CH_4-TPSR, approximately 50 mg of calcined catalyst was reduced with 10%H_2/Ar (30 mL/min) at 550°C for 1 h at 10°C/min ramp rate. Upon reduction, the catalyst surface was purged with helium to remove weakly adsorbed H_2 and cooled to ambient temperature. Subsequently, 10%CH_4/He (30 mL/min) was introduced while the temperature rising from ambient temperature to 600°C at 10°C/min ramp rate. Then pure helium was introduced to cool the catalysts. The carbon species formed during CH_4–TPSR were characterized by differential thermogravimetry (DTG). Spent catalyst after CH_4-TPSR test was subjected to 40 mL/min air to oxidize carbon species from room temperature to 800°C at 5°C/min ramp rate.

Carbon dioxide–Temperature programmed surface reaction/Hydrogen–Temperature programmed reduction (CO_2-TPSR/H_2-TPR) experiments were performed in Micromeritics AutoChem II 2920. Same pretreatment procedure like CH_4–TPSR was employed. $10\%CO_2$/He (30 mL/min) was introduced while the temperature raising from ambient temperature to $700°C$ at $10°C$/min ramp rate. Then pure helium was introduced to cool the catalysts. The oxygen species formed during CO_2 dissociation were characterized by performing H_2-TPR using $10\%H_2$-Ar (30 mL/min) from ambient temperature to $700°C$ at $10°C$/min ramp rate.

2.2.2 CO pulse chemisorption

Carbon monoxide chemisorption was conducted in Micromeritics Autochem II 2920. Typically, 50 mg of calcined catalyst was reduced at $450°C/550°C$ for 1 h at $10°C$/min ramp rate using $10\%H_2$/Ar (30 mL/min). After reduction, the catalyst bed was cooled down to room temperature using pure helium. Subsequently, multiple pulses of $10\%CO$/He were injected at room temperature to saturate metallic sites.

2.2.3 X-ray photoelectron spectroscopy

X-ray photoelectron spectroscopy (XPS) was carried out on a Thermo Scientific K-Alpha system. Spectrophotometer was equipped with an Al source and a $180°$ double focusing hemispherical analyzer. Additionally, a 128–channel detector was equipped at a pass energy of 50 eV for the analyses of the core level signals of Fe 2p, Ni 2p, O 1s, Ce 3d and Ti 2p. XPS spectra data were calibrated using C 1s peak (284.8 eV).

2.2.4 Thermogravimetric Analysis-Differential Thermogravimetry (TGA-DTG)

Thermogravimetric analysis (TGA)/Differential thermogravimetry (DTG) of the used catalysts was performed on Mettler Toledo Thermal Analyzer (TGA/DSC 1). Typically, used catalyst was oxidized in air while temperature was increased from 25˚C to 800˚C at ramping rate of 5˚C/min.

2.2.5 Raman spectroscopy

Raman spectra was carried out with a NT-MDT Raman spectrometer using a diode laser beam. An excitation wavelength of 532 nm was used. The Raman spectra were collected by co-adding five scans of 10 s and the laser power of 22 ± 2 mW under ambient conditions.

2.2.6 *In-situ* DRIFTS analysis

In-situ Diffuse Reflectance Infrared Fourier Transform Spectroscopy (DRIFTS) experiment was performed in ThermoFisher Nicolet IS50 FTIR spectrometer using Harrick Scientific diffuse reflection accessory equipped with mercury-cadmium-telluride (MCT) detector. Prior to the test, the catalyst was reduced *ex-situ* at 450˚C/550˚C for 1 h. Following reduction, the catalyst was transferred into DRIFTS cell and purged under helium for 1 h at 550˚C. Thereafter, the background of DRIFTS was obtained under He until the collected background spectra remained stable. Following background scan, a pulse of 10%CH_4/He (20 cc/min) was introduced in the reactor cell for 5 min. The IR spectra was collected every 1 min. 10%CO_2/He pulse of equal volume was introduced for 5 min followed by another pulse of 10% CH_4/He.

2.2.7 BET surface area analysis

The specific surface area of reduced catalysts was determined by N_2 physisorption in Micromeritics ASAP 2020 porosity analyzer at -196°C. Prior to physisorption, approximately 0.15 g of sample was degassed under He at 350°C for 6 h. The specific surface area of catalysts was evaluated based on Brunauer-Emmett-Teller (BET) method.

2.3 Catalytic activity performance

The dry reforming of methane tests were carried out in a fixed-bed reactor at 550°C and atmospheric pressure. 0.1 – 0.2 g of calcined catalyst was reduced with 30% H_2/He at 450°C/550°C for 1 h. Subsequently, pure helium was introduced to the reactor. The mixture of 10% CH_4/He and 10% CO_2/He was introduced simultaneously into the reactor with flow rate as 30 mL/min. A similar procedure was employed for evaluating catalytic performance in CH_4 decomposition reaction. The outlet gases concentrations were analyzed by online SRI GC (8610C) equipped with one TCD and one FID. Consumption of CH_4 and/or CO_2 was calculated using the following equations:

$$CH_4 \ consumption \ = \left(\frac{F_{CH_4 \ in} - F_{CH_4 \ out}}{metal \ surface \ area} \right)$$

$$CO_2 \ consumption = \left(\frac{F_{CO_2 \ in} - F_{CO_2 \ out}}{metal \ surface \ area} \right)$$

$$H_2/CO \ \text{Ratio} = \frac{H_2 \ produced \ (\mu mol \cdot h^{-1})}{CO \ produced \ (\mu mol \cdot h^{-1})}$$

$$Carbon \ Balance \ (\%) \ = \left(\frac{F_{CH_4 \ out} + F_{CO_2 \ out} + F_{CO \ out}}{F_{CH_4 \ in} + F_{CO_2 \ in}} \right) * 100$$

Chapter 3

Bimetallic Ni-Fe/TiO$_2$ catalysts synthesized by wet-impregnation procedure for low temperature dry reforming of methane

3.1 Introduction

Greenhouse gases emission, particularly CO_2, CH_4, NO_x, has elevated the surface temperature of earth in the past few decades [1,2]. In order to mitigate anthropogenic greenhouse gases levels, catalysis could be one of the possible approaches [3]. One of the plausible ways to utilize methane as an important C$_1$ feedstock could be its transformation to useful chemicals. For instance, steam reforming of methane is widely used in industry to produce hydrogen with the aid of Ni based catalysts [4]. Analogous to steam reforming, the dry reforming unites CH_4 and CO_2 in a single reaction and produces synthesis gas, the mixture of carbon monoxide and hydrogen. Dry reforming of methane (DRM, reaction 1) is inevitable to high reaction temperature because of high endothermicity and is accompanied by reverse water-gas shift reaction (reaction 2) [5].

$$CH_4 + CO_2 \rightarrow 2CO + 2H_2 \qquad\qquad \Delta H = 247 \; kJ/mol \qquad\qquad (1)$$

$$CO_2 + H_2 \rightarrow CO + H_2O \qquad\qquad \Delta H = 41.2 \; kJ/mol \qquad\qquad (2)$$

$$CH_4 \rightarrow C + 2H_2 \qquad\qquad \Delta H = 75 \; kJ/mol \qquad\qquad (3)$$

$$2CO \rightarrow C + CO_2 \qquad\qquad \Delta H = -172.5 \; kJ/mol \qquad\qquad (4)$$

The major challenge for the industrial development of DRM is catalyst deactivation. Methane decomposition (reaction 3) and CO disproportionation (reaction 4) causes coke deposition, which is suggested as primary reason for catalyst deactivation. The active catalysts for DRM include

precious metals such as Ru, Rh, Pt and Pd. Precious metals are reported to be coke resistant [6]. However, their high cost and low abundance hinder their practical applications. Non-precious metals, particularly Ni-based catalysts have been studied [5]. Ni based catalysts show initial activity comparable to precious metals but are prone to deactivation due to coking [5]. Thus, it is essential to develop Ni-based catalysts for DRM that show activity comparable to precious metals but are coke resistant. Various strategies could be employed to enhance the performance of Ni-based catalysts. Choice of supports could be one potential option. For example, complete formation of NiO–MgO solid solution and high Ni dispersion was suggested for enhanced activity and coke resistance over Ni/MgO catalysts [7]. Formation of $La_2O_2CO_3$ during DRM over Ni/La_2O_3 was responsible for coke removal [8]. Metal-support interactions could also play important role in preventing coke formation. Metallic Ni formed by reduction of $NiAl_2O_4$ spinel in CO and H_2 atmosphere was shown to be highly active and stable catalyst for DRM [9]. Highly dispersed Ni catalysts supported over $MgAl_2O_4$ were also demonstrated to be coke resistant. This was attributed to the interaction of Ni with $MgAl_2O_4$ spinel and high resistance to sintering [10]. On the other hand, reducible supports including CeO_2 could also be promising, because its surface oxygen species could oxidize coke to CO [11]. However, formation of CeO_{2-x} after reduction was not helpful in alleviating carbon deposits. Large ensembles of Ni^0 formed upon reduction were responsible for coking [12]. TiO_2 support has also been studied for dry reforming of methane [13]. It was inferred that Ni interacts strongly with TiO_x species formed upon reduction at 700˚C. Migration of TiO_x over the exposed Ni particles might reduce the formation of large Ni^0 ensembles. This phenomenon would ultimately decrease the surface free-energy and could enhance the coke resistance [14]. Similarly, interface between active metal and TiO_x (Me–O_v–Ti^{3+}) was suggested to be favorable for activity and coke removal [15]. Besides oxide supports, introduction of first

row transition metals as promoters could be also beneficial. For example, Fe, Co or Cu were suggested to suppress coke deposition over Ni catalysts [16]. Oxophilic nature of cobalt in Ni–Co catalysts was shown to remove coke [17]. Ni–Fe catalysts also emerged to be coke resistant. Herein, FeO_x formed upon CO_2 exposure dealloyed from Ni–Fe alloy. FeO_x was then responsible for oxidizing coke to CO [18–20]. In conclusion, choice of support along with promoting metal/metal oxide might stabilize Ni catalysts by inhibiting coke formation during dry reforming reaction.

Among transition metals, Fe could be promising choice as a promoter because of its abundance and low cost in comparison to Co and Cu. We hypothesize that tuning Ni with Fe over a reducible oxide support such as TiO_2 could be a potential option to inhibit coke deposition. To the best of our knowledge, bimetallic Ni–Fe/TiO_2 catalysts have not been investigated for dry reforming of methane. In this study, we explore the effect of Fe addition in Ni/TiO_2 on catalytic performance and coke formation.

3.2. Results and discussion

3.2.1 Hydrogen–Temperature Programmed Reduction (H_2-TPR)

Hydrogen–temperature programmed reduction (H_2-TPR) was employed to study the reducibility of Ni/TiO_2, Fe/TiO_2 and Ni–Fe/TiO_2 catalysts. We conducted peak deconvolution analysis to gain insights of reduction process. Fig.3.1 shows H_2-TPR profiles of monometallic and bimetallic catalysts. For Ni/TiO_2, peak 1 (323˚C) and peak 2 (368˚C) is attributed to bulk NiO species which do not interact with the support [14]. Reduction of species corresponding to peak 1 and/or 2 forms large Ni^0 particles which show tendency for carbon deposition [14,21]. Peak 3 (409˚C) is assigned to the reduction of strongly interacting NiO–TiO_2 species [14]. The reduction

of NiO in Ni/TiO$_2$ is represented as NiO + H$_2$ → Ni^0 + H$_2$O. Table 3.1 shows that estimated total H$_2$ consumption over Ni/TiO$_2$ is 2.25 mmol H$_2$/g$_{catalyst}$. For Fe/TiO$_2$, Reduction of Fe$_2$O$_3$ occurred through three steps, Fe$_2$O$_3$ → Fe$_3$O$_4$ → FeO → Fe^0 [22-24]. Peak 1 (262°C) is attributed to the reduction of Fe$_2$O$_3$ → Fe$_3$O$_4$. While peak centered at 319°C is assigned to the reduction of Fe$_3$O$_4$ → FeO. Further reduction of FeO to Fe^0 occurred around 660°C. The overall estimated total H$_2$ consumption by Fe/TiO$_2$ is 3.01 mmol H$_2$/g$_{catalyst}$. Reduction of Fe$_2$O$_3$ is represented as Fe$_2$O$_3$ + 3H$_2$ → 2Fe^0 + 3H$_2$O.

H$_2$-TPR profiles of bimetallic Ni–Fe/TiO$_2$ catalysts are distinctly different from their monometallic counterparts. Ni$_3$Fe$_1$/TiO$_2$ and Ni$_1$Fe$_1$/TiO$_2$ showed similar reduction profiles and could be fitted with 4 distinct Gaussian peaks. Peak 1 (around 212°C) is contributed to the reduction of bulk NiO [14]. Peak 2 (around 256°C) is related to the reduction of Fe$_2$O$_3$ to Fe$_3$O$_4$ [23]. Peak 3 (around 289°C) results from reduction of Fe$_3$O$_4$ to FeO [23]. Peak 4 centered around 335°C demonstrates reduction of NiO species to Ni^0 which strongly interacts with TiO$_2$ support [14]. Details of peak analysis and hydrogen consumption are summarized in Table 3.1. H$_2$ consumption corresponding to peak 1 in Ni$_3$Fe$_1$/TiO$_2$ and Ni$_1$Fe$_1$/TiO$_2$ catalysts decreased in comparison to Ni/TiO$_2$. It may be explained as introduction of Fe in Ni/TiO$_2$ inhibited the formation of bulk NiO. Contrarily, H$_2$ consumption related to the reduction of strongly interacting NiO–TiO$_2$ species to Ni^0 increased from 1.37 mmol H$_2$/g$_{catalyst}$ over Ni/TiO$_2$ to 1.45 mmol H$_2$/g$_{catalyst}$ over Ni$_3$Fe$_1$/TiO$_2$. It suggested that 2.5 wt% addition of Fe might have increased the strong interactions of NiO with TiO$_2$ support and hence the reducibility of NiO. However, H$_2$ consumption corresponding to peak 2 increased from 0.32 mmol H$_2$/g$_{catalyst}$ over Ni$_3$Fe$_1$/TiO$_2$ to 1.03 mmol H$_2$/g$_{catalyst}$ over Ni$_1$Fe$_1$/TiO$_2$. Those results indicated that peak 2 in Ni–Fe/TiO$_2$ catalysts is related to the reduction of Fe$_2$O$_3$. Additionally, comparing the H$_2$–TPR profiles of Ni–Fe/TiO$_2$

catalysts with monometallic Fe/TiO$_2$, it could be observed that reduction of Fe$_2$O$_3$ → Fe$_3$O$_4$ would correspond to peak 2. Furthermore, H$_2$ consumption corresponding to peak 3 drops approximately 10 times with increase in Fe loading from 2.5 wt% to 5 wt%. It suggested that reduction of Fe$_3$O$_4$ to FeO is inhibited in Ni$_1$Fe$_1$/TiO$_2$. The behavior is explained by decreased amount of Ni^0 in Ni$_1$Fe$_1$/TiO$_2$ which facilitates hydrogen spill-over during reduction. H$_2$ consumption corresponding to reduction of NiO–TiO$_2$ species to Ni^0 dropped from 1.45 mmol H$_2$/g$_{catalyst}$ over Ni$_3$Fe$_1$/TiO$_2$ to 1.26 mmol H$_2$/g$_{catalyst}$ over Ni$_1$Fe$_1$/TiO$_2$. It suggested that substitution of Fe in Ni/TiO$_2$ up to 2.5 wt% could be beneficial to enhance the reducibility of NiO and further substitution might not be helpful. It should be noted that reduction of NiO and Fe$_2$O$_3$ in Ni-Fe/TiO$_2$ catalysts occurred differently, suggesting non-interacting behavior within metal oxides on support.

Ni$_1$Fe$_3$/TiO$_2$ demonstrated reduction profile similar to Fe/TiO$_2$. A shoulder peak at 217˚C is assigned to weak interactions between NiO and TiO$_2$ support. Peak 2 (267˚C) represents reduction of Fe$_2$O$_3$ to Fe$_3$O$_4$. Peak 3 (304˚C) is related to the reduction of NiO to Ni^0. Further, peak 4 and 5 located at 388˚C and 526˚C is attributed to step reduction of Fe$_3$O$_4$ → FeO → Fe^0 respectively. H$_2$ consumption for reduction of NiO–TiO$_2$ to Ni^0 over Ni$_1$Fe$_3$/TiO$_2$ dropped to 0.32 mmol H$_2$/g$_{catalyst}$ compared to that of Ni/TiO$_2$ catalyst. These results imply that 7.5 wt% substitution of Ni by Fe did not enhance the reducibility of NiO. Similar TPR profile of bimetallic Ni–Fe/TiO$_2$ catalysts has been reported in the literature [25]. However, reduction temperature related to NiO and Fe$_2$O$_3$ in Ni/TiO$_2$, Fe/TiO$_2$ and Ni–Fe/TiO$_2$ catalysts differed from our results. This behavior could be attributed to difference in catalyst preparation and calcination procedure.
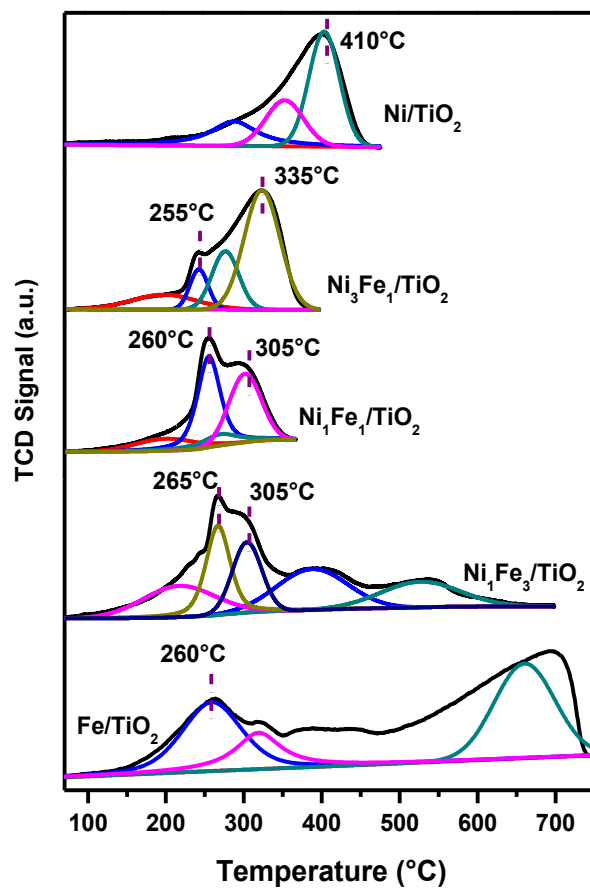
Fig. 3.1. H_2-TPR profiles of Ni/TiO_2, Ni–Fe/TiO_2 and Fe/TiO_2 catalysts synthesized by wet-impregnation route.

Table 3.1. Analysis of H_2-TPR profiles of Ni/TiO_2, Ni–Fe/TiO_2 and Fe/TiO_2 catalysts synthesized by wet-impregnation route.

Catalyst	Peak 1	Peak 2	Peak 3	Peak 4	Peak 5	Total (mmol/$g_{catalyst}$)
Ni/TiO_2	323 (0.4)	368 (0.48)	409 (1.37)	–	–	2.25
Ni_3Fe_1/TiO_2	212 (0.18)	256 (0.32)	289 (0.37)	335 (1.45)	–	2.32
Ni_1Fe_1/TiO_2	203 (0.14)	259 (1.03)	274 (0.037)	305 (1.26)	–	2.47
Ni_1Fe_3/TiO_2	217 (0.18)	267 (1.11)	304 (0.32)	388 (0.61)	526(0.43)	2.65
Fe/TiO_2	262 (0.85)	405 (0.42)	615 (0.54)	690 (1.2)	–	3.01

3.2.2 Pulse CO-Chemisorption

Table 3.2 shows CO uptake values over reduced catalysts. Typically, CO uptake values are correlated with number of metallic sites on catalyst surface with the assumption that each CO molecule chemisorbs one metallic site. For monometallic Ni/TiO_2 catalyst, the CO uptake is 18.2 $\mu mol/g$. While monometallic Fe/TiO_2 did not show chemisorbed CO suggesting metallic sites were absent in Fe/TiO_2. The chemisorption values indicated Ni/TiO_2 contains essentially higher metallic sites than Fe/TiO_2. Consequently, addition of Fe inhibited formation of metallic sites and results are reflected by decreased CO uptake values. The CO uptake values decreased from 9.7 to 3.5 $\mu mol/g$ in Ni_3Fe_1/TiO_2 and Ni_1Fe_3/TiO_2 catalyst respectively.

Table 3.2. CO uptake values over Ni/TiO_2, $Ni-Fe/TiO_2$ and Fe/TiO_2 catalysts synthesized by wet-impregnation route.

Catalyst	CO Adsorbed ($\mu mol/g$)
Ni/TiO_2	10.8
Ni_3Fe_1/TiO_2	9.7
Ni_1Fe_1/TiO_2	4.7
Ni_1Fe_3/TiO_2	3.5
Fe/TiO_2	0

3.2.3 Methane–Temperature Programmed Surface Reaction/Differential Thermogravimetry (CH_4-TPSR/DTG)

CH_4-TPSR was performed to screen the activity of CH_4 over mono and bimetallic catalysts. As shown in Fig.3.2a, CH_4 was activated around 400˚C and simultaneously peaked up to 540˚C in Ni/TiO_2. Addition of Fe shifted CH_4 activation temperature to 450˚C and peaked up to 590˚C.

While monometallic Fe/TiO$_2$ did not show activity towards CH$_4$ and agrees with the literature reports [19,20]. The results suggested that addition of Fe to Ni/TiO$_2$ inhibited dissociation of CH$_4$. Such behavior may prove beneficial to avoid coke deposition during DRM. The type of carbon formed during CH$_4$-TPSR tests was elucidated by TGA-DTG experiment and is shown in Fig.3.2b. Ni/TiO$_2$ showed carbon oxidation peak around 540˚C. However, this peak was shifted to lower temperature at 500˚C in Ni-Fe/TiO$_2$ catalysts. The results indicated that addition of Fe is helpful to promote oxidation of carbon. Coke formation on Ni catalysts is shown to be deposition-diffusion-precipitation mechanism [26]. Herein, coke deposited on Ni sites diffuses from metal to support interface to the other side of catalyst surface. Owing to the inactivity of Fe atoms towards carbon, addition of Fe will ultimately inhibit the diffusion and precipitation of coke precursors in the vicinity of Ni atoms. This argument is further supported by H$_2$-TPR analysis which showed non-interacting nature of Ni-Fe species on the surface.
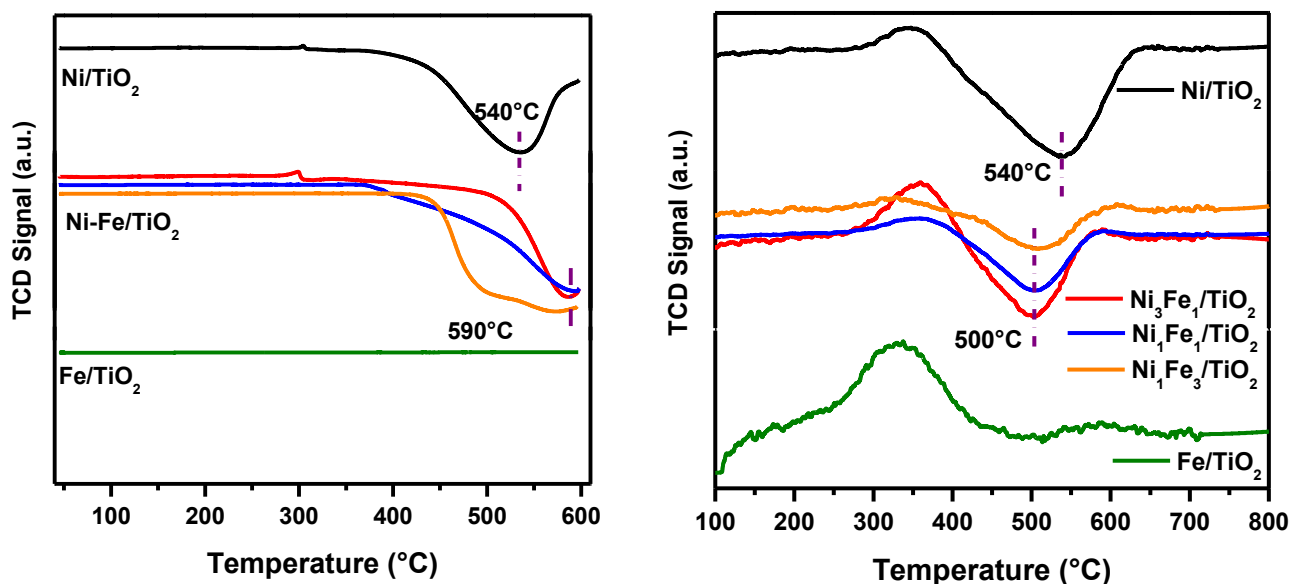

Fig. 3.2. CH$_4$-TPSR profiles (a) and DTG profiles (b) of Ni/TiO$_2$, Ni-Fe/TiO$_2$ and Fe/TiO$_2$ catalysts synthesized by wet-impregnation route

3.2.4 Carbon dioxide – Temperature programmed surface reaction/Hydrogen – Temperature programmed reduction (CO_2-TPSR/H_2-TPR)

Activation and thereby dissociation CO_2 to CO^* and O^* is beneficial during DRM. The O^* species reacts with CH_x species derived from CH_4 decomposition to produce CO and H_2. Moreover, CO_2-TPSR/H_2-TPR could also provide understanding on the nature of active centers on catalyst surface to dissociate CO_2 to CO^* and O^* [27]. Thus, CO_2-TPSR/H_2-TPR is performed over reduced catalysts to gain insights on CO_2 dissociation. CO_2-TPSR/H_2-TPR over reduced catalysts could be described according to following equations.

$$CO_2 \rightarrow CO^* + O^* \quad (5)$$

$$O^* + H_2 \rightarrow H_2O \quad (6)$$
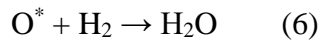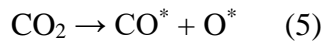
Dissociation of CO_2 on active metal or interface between active-metal and support forms CO^* and surface adsorbed oxygen species O^*. Formed O^* species are then characterized by H_2-TPR. The H_2 consumed in the TPR is directly correlated to O^* species formed during CO_2 dissociation according to equation 5 and 6. Fig. 3.3 shows H_2-TPR profiles of reduced Ni/TiO_2, Ni-Fe/TiO_2 and Fe/TiO_2 catalysts after performing CO_2-TPSR tests. Ni/TiO_2 catalyst showed three distinct H_2 consumption peaks. Reduction of O^* formed during CO_2-TPSR begins nearly at 85˚C and peaks up to 540˚C. Both peaks are attributed to active Ni^0 centers in Ni/TiO_2 catalyst. For Fe/TiO_2 catalyst, there is no low temperature peak unlike Ni/TiO_2 catalyst. Interestingly, the H_2-TPR profile of Fe/TiO_2 after CO_2-TPSR showed a strong H_2 consumption peak above 700˚C. This result indicated strong ability of Fe/TiO_2 to effectively dissociate CO_2 to CO^* and O^*. Accordingly, the O^* reduction peaks of Ni-Fe/TiO_2 catalysts after CO_2-TPSR shifted to higher temperature than

Ni/TiO$_2$ catalyst. Ni$_3$Fe$_1$/TiO$_2$ showed a small peak at 95˚C, a broad peak around 560˚C and a shoulder peak at 610˚C. For all the Ni-Fe/TiO$_2$ catalysts, peaks located below 600˚C are assigned to Ni^0 centers. Whereas, peak appearing above 600˚C is related to Fe^0 sites. Comparison between O* reduction peak temperatures of Ni/TiO$_2$ and Ni-Fe/TiO$_2$ catalysts suggested that introduction of Fe enhanced the adsorption of O* species formed from CO$_2$ dissociation. In other words, addition of Fe would promote gasification of coke formed from CH$_4$ decomposition during DRM. Similar CO$_2$-TPSR/H$_2$-TPR profile of Ni/Mg(Al)O and Ni-Cu/Mg(Al)O catalyst has been reported [28]. To gain further information on O* formation, H$_2$ consumption during H$_2$-TPR after CO$_2$-TPSR was calculated. As shown in Table 3.3, the amount of H$_2$ consumed increased upon Fe addition. This result suggested that introduction of Fe would promote CO$_2$ dissociation to CO* and O* at least under current experimental conditions.

Table 3.3. H$_2$ consumption during H$_2$-TPR after CO$_2$-TPSR tests over Ni/TiO$_2$, Ni-Fe/TiO$_2$ and Fe/TiO$_2$ catalysts synthesized by wet-impregnation route.

Catalyst	H$_2$ Consumption (mmol g$_{(Ni+Fe)}^{-1}$)
Ni/TiO$_2$	8.3
Ni$_3$Fe$_1$/TiO$_2$	26.9
Ni$_1$Fe$_1$/TiO$_2$	32.0
Ni$_1$Fe$_3$/TiO$_2$	-
Fe/TiO$_2$	-
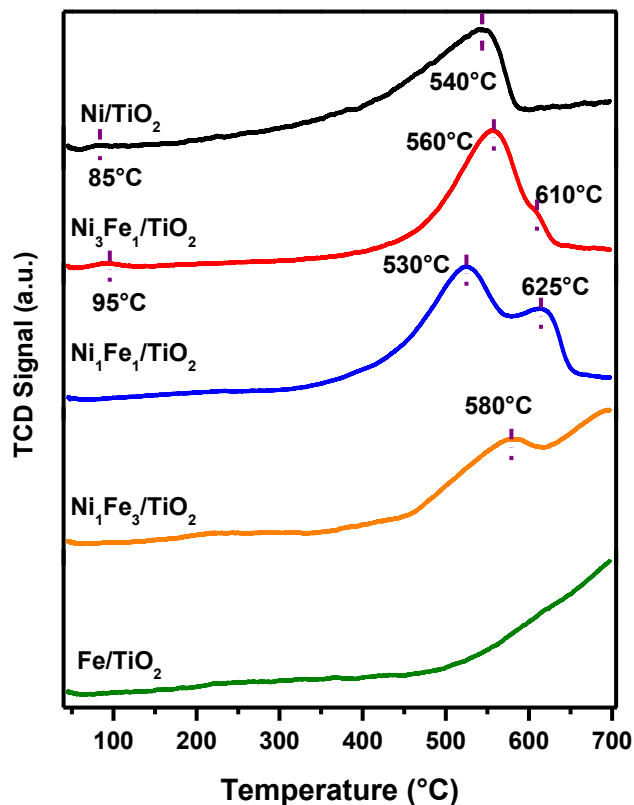
Fig. 3.3. H_2-TPR profiles of Ni/TiO$_2$, Ni-Fe/TiO$_2$ and Fe/TiO$_2$ catalysts synthesized by wet-impregnation route after CO$_2$-TPSR test.

3.2.5 X-ray Photoelectron Spectroscopy (XPS) of reduced catalysts

X-ray photoelectron spectroscopy (XPS) is applied to understand oxidation state and concentration of surface species. Ni $2p_{3/2}$ spectra of reduced catalysts are shown in Fig. 3.4a. For all reduced catalysts, peak appearing at 852.7 eV is assigned to Ni^0 while peak around 855.5 eV is attributed to Ni^{2+} present as NiO. Presence of Ni^{2+} peaks suggested incomplete reduction of NiO in Ni/TiO$_2$ and Ni–Fe/TiO$_2$ catalysts at 450°C. Generally, Ni^{2+} peak is located around 854.4 eV in Ni-based catalysts. However, a shift of +1.4 eV in NiO indicated decreased electron density of Ni^{2+}. Specifically, electron transfer from Ni^{2+} at metal-support interface would result due to interaction between NiO and TiO$_2$ [29,30]. The observation agrees with H$_2$-TPR analysis of

68

Ni/TiO$_2$ which demonstrated metal-support interactions between NiO and TiO$_2$. XPS spectra of Fe 2p$_{3/2}$ in reduced Ni-Fe/TiO$_2$ catalysts is shown in Fig. 3.4b. For Ni$_3$Fe$_1$/TiO$_2$, peak occurring at 709.7 eV is assigned to Fe^{2+} [28,31]. While Ni$_1$Fe$_1$/TiO$_2$ and Ni$_1$Fe$_3$/TiO$_2$ catalysts revealed presence of Fe^{3+} at 711.2 eV along-with Fe^{2+}. Deconvolution of Ti 2p$_{3/2}$ spectra showed Ti^{3+} peak at 457.4 eV in the reduced catalysts. Existence of Ti^{3+} species affirms formation of oxygen vacancies in TiO$_2$ supported catalysts. Previous reports have demonstrated formation of TiO$_x$ species by hydrogen spill-over process during reduction of Ni/TiO$_2$ catalysts [14]. The composition of surface species in the reduced catalysts was evaluated and is shown in Table 3.4. It is observed that Ni^0 concentration dropped significantly from 1.17% to 0.16% Ni/TiO$_2$ and Ni-Fe/TiO$_2$ catalysts. Drop in Ni^0 concentration directly influenced catalytic activity performance in DRM. For Ni$_3$Fe$_1$/TiO$_2$, surface composition of Fe^{2+} was about 4.58%. While, Fe^{2+} concentration decreased significantly in Ni$_1$Fe$_1$/TiO$_2$ and Ni$_1$Fe$_3$/TiO$_2$. This behavior could be explained by the ability of metallic Ni species to promote H$_2$ dissociation [32]. Hydrogen spillover would enhance the reduction of iron oxide [32]. Therefore, increasing the Fe loading from 2.5 wt% to 7.5 wt% (i.e. Ni$_3$Fe$_1$/TiO$_2$ → Ni$_1$Fe$_3$/TiO$_2$) decreased the number of active metallic Ni species which would inhibit the reduction of iron oxides. XPS results of Ni and Fe are consistent with H$_2$-TPR showing that reducibility of iron oxide decreased with decrease in Ni loading. While there is considerable interaction between NiO and TiO$_2$ support. Further, the surface Ni/Fe ratio in the reduced Ni-Fe/TiO$_2$ catalysts were 1.36, 0.43 and 0.28 which were lower than their bulk counterparts. The observation suggested partial encapsulation of Ni by Fe species during reduction process. Surface O/Ti ratio for all the reduced catalysts was below 2 evidencing the formation of TiO$_x$ upon reduction.
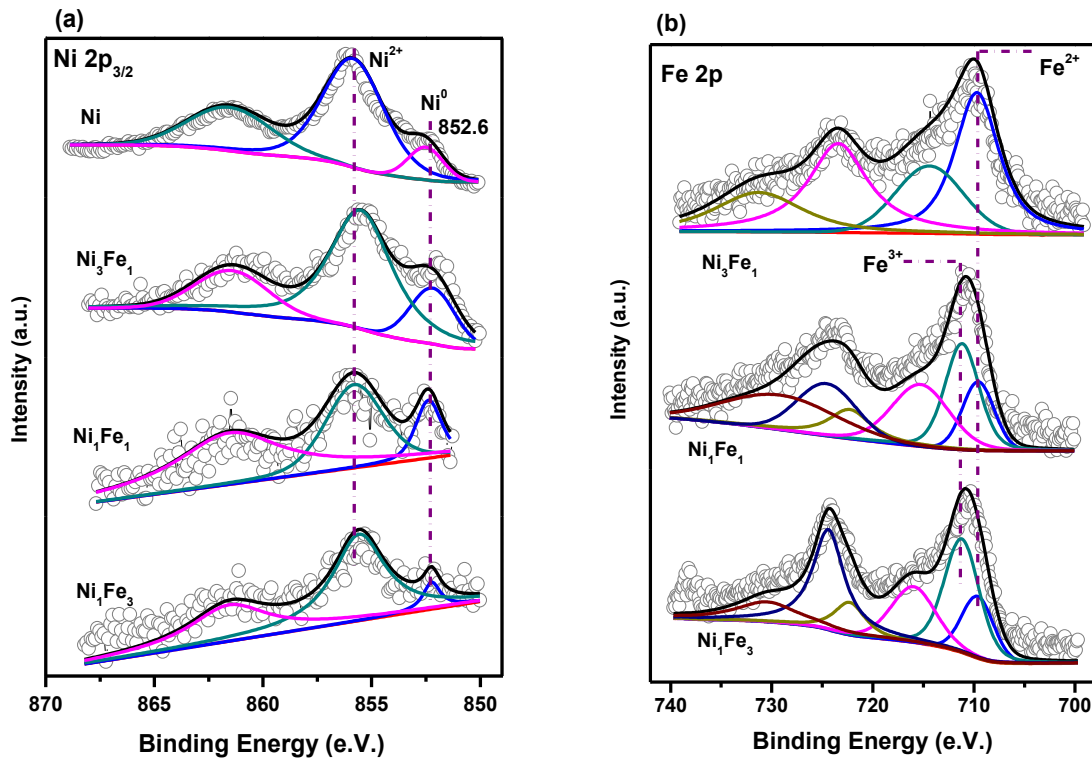
Fig.3.4. (a) Ni 2p$_{3/2}$ XPS spectra and (b) Fe 2p XPS spectra of reduced catalysts synthesized by wet-impregnation route.

Table 3.4. Atomic concentration (%) of surface species in reduced catalysts synthesized by wet-impregnation route.

Catalyst	Ni^0	Ni^{2+}	Fe^{2+}	Fe^{3+}	Ni/Fe	O/Ti
Ni/TiO$_2$	1.15	9.22	-	-	-	1.34
Ni$_3$Fe$_1$/TiO$_2$	1.02	6.22	5.60	-	1.29	1.37
Ni$_1$Fe$_1$/TiO$_2$	0.29	2.29	2.17	3.96	0.42	1.41
Ni$_1$Fe$_3$/TiO$_2$	0.20	1.64	2.01	4.59	0.28	1.54

3.2.6 Catalytic performance in dry reforming of methane and CH_4 – decomposition

Fig. 3.5a and 3.5b shows consumption rates of CH_4 and CO_2 as a function of reaction time respectively. For Ni/TiO$_2$, the CH_4 and CO_2 conversion after 1 h TOS is 62 $\mu mol/m^2_{Ni+Fe}$ h and 71 $\mu mol/m^2_{Ni+Fe}$ h respectively. Higher consumption of CO_2 compared to CH_4 is attributed to RWGS reaction prevalent under given reaction conditions. CH_4 consumption increases monotonically while CO_2 consumption drops with TOS. After 6 h of reaction, the CH_4 consumption increased to 69 $\mu mol/m^2_{Ni+Fe}$ h whereas CO_2 consumption decreased to 66 $\mu mol/m^2_{Ni+Fe}$ h. The increase in CH_4 consumption with TOS is attributed to occurrence of CH_4 decomposition which is considered as inevitable side reaction on Ni-based catalysts [33,34]. On the other hand, drop in CO_2 consumption is related to CO disproportionation that produces CO_2, and is thermodynamically favored below 700˚C [6]. As shown in Fig. 3.6c, the H_2/CO ratio over Ni/TiO$_2$ after 1 h TOS was 0.83 and increased to 0.94 after 6 h. The carbon decreased from 89% to 84% during TOS. Thus, catalytic performance on Ni/TiO$_2$ suggested that initial activity is essentially controlled by DRM while CH_4 decomposition dominates after 2 h TOS. Similar behavior has been observed over Ni based catalysts which showed dominance towards CH_4 decomposition with TOS at 550˚C [33,34]. In comparison to Ni/TiO$_2$, bimetallic Ni–Fe/TiO$_2$ catalysts showed lower CH_4 and CO_2 consumption. This indicated passivating effect of Fe on catalytic performance. The CH_4 and CO_2 consumption over Ni$_3$Fe$_1$/TiO$_2$ after 1 h TOS was 67 $\mu mol/m^2_{Ni+Fe}$ h and 70 $\mu mol/m^2_{Ni+Fe}$ h respectively. Unlikely the Ni/TiO$_2$ catalyst, the CH_4 conversion dropped to 51 $\mu mol/m^2_{Ni+Fe}$ h. It seems that 2.5 wt% substitution of Ni by Fe might have increased the activation barrier for CH_4 decomposition [18]. This behavior could be beneficial for reducing carbon deposition. The H_2/CO ratio observed over Ni$_3$Fe$_1$/TiO$_2$ after 1 h TOS was 0.77 and remains almost similar during the reaction. Decrease in H_2/CO ratio over Ni$_3$Fe$_1$/TiO$_2$ than Ni/TiO$_2$ suggests suppression of CH_4 decomposition as side

reaction. However, this decrease could also be related to presence of iron oxide which could accelerate reverse water-gas shift reaction in Ni_3Fe_1/TiO_2 catalyst [35]. The carbon balance over Ni_3Fe_1/TiO_2 after 1 h TOS was 90.9% and increased to 91.8% after 6 h of reaction. These results indicated that 2.5 wt% substitution of Ni by Fe might have promoted carbon removal from catalyst surface during the course of reaction.

5 wt% substitution of Ni by Fe dropped the CH_4 and CO_2 consumption drastically. After 1 h TOS, the CH_4 consumption over Ni_1Fe_1/TiO_2 was 27 $\mu mol/m^2_{Ni+Fe}$ h and decreased to 13 $\mu mol/m^2_{Ni+Fe}$ h after 6 h. Similarly, CO_2 consumption dropped from 25 $\mu mol/m^2_{Ni+Fe}$ h to 14 $\mu mol/m^2_{Ni+Fe}$ h. The catalytic performance results of Ni_1Fe_1/TiO_2 with TOS suggested loss of active Ni^0 sites during the course of reaction. The H_2/CO ratio revealed interesting behavior during the course of reaction. After 1 h, the ratio was 0.67 and dropped to 0.43 after 6 h, which is lower than thermodynamic equilibrium value of 0.86 under the consideration of DRM and RWGS reactions. Such behavior indicated dominance of reverse water-gas shift reaction over dry reforming [12,18,36]. Decrease in H_2/CO ratio compared to Ni_3Fe_1/TiO_2 could also be attributed to increase in Fe loading (2.5 wt% → 5 wt%) that shows selectivity towards CO formation [32]. Meanwhile, the carbon balance increases from 92.7% to 96.0% and could be related to removal of coke by iron oxide sites. When it comes to Ni_1Fe_3/TiO_2 catalyst, similar trend as Ni_1Fe_1/TiO_2 in CH_4/CO_2 conversion, H_2/CO ratio and carbon balance was observed. The CH_4/CO_2 consumption and H_2/CO ratio further dropped. However, the carbon balance further increased from 94.5% to 97.8%. Activity performance over Ni_1Fe_3/TiO_2 with TOS suggested reduction in accessible Ni^0 sites during reaction and that presence of FeO_x sites might have shifted the reaction equilibrium from dry reforming to reverse water-gas shift. Thus, tuning the ratio between Ni and Fe could be helpful for DRM by controlling the side reactions. Kim et al. [18] demonstrated highest CH_4

72

consumption over $Ni/MgAl_2O_4$ catalyst after 1 TOS, which decreased significantly after 10 h TOS. Deactivation of $Ni/MgAl_2O_4$ was attributed to coke formation. However, bimetallic Ni–$Fe/MgAl_2O_4$ catalysts showed stable CH_4 consumption during DRM and decreased coking. Compared to our results, a similar trend in H_2/CO ratio was also reported. For monometallic $Ni/MgAl_2O_4$ catalyst, the H_2/CO ratio exceeded the thermodynamic equilibrium value. While Ni–$Fe/MgAl_2O_4$ showed decrease in H_2/CO ratio compared to $Ni/MgAl_2O_4$. Such behavior was attributed to side reactions such as CH_4 decomposition or CO disproportionation reaction.

The catalytic activity in CH_4 decomposition is shown in Fig.3.6a-b. Similar to DRM, Ni/TiO_2 showed maximum CH_4 conversion while addition of Fe decreased CH_4 decomposition activity. The results agree with CH_4-TPSR shown in section 3.3. However, formation of CO was also observed besides H_2 during CH_4 decomposition. As the reactant feed contains only CH_4, formation of CO suggested oxidation of coke precursors by the lattice oxygen from FeO_x and TiO_2 support. Further, it should be noticed that amount of CO formed increases with Fe content, indicating that lattice oxygen from FeO_x would play dominant role to oxidize coke species.
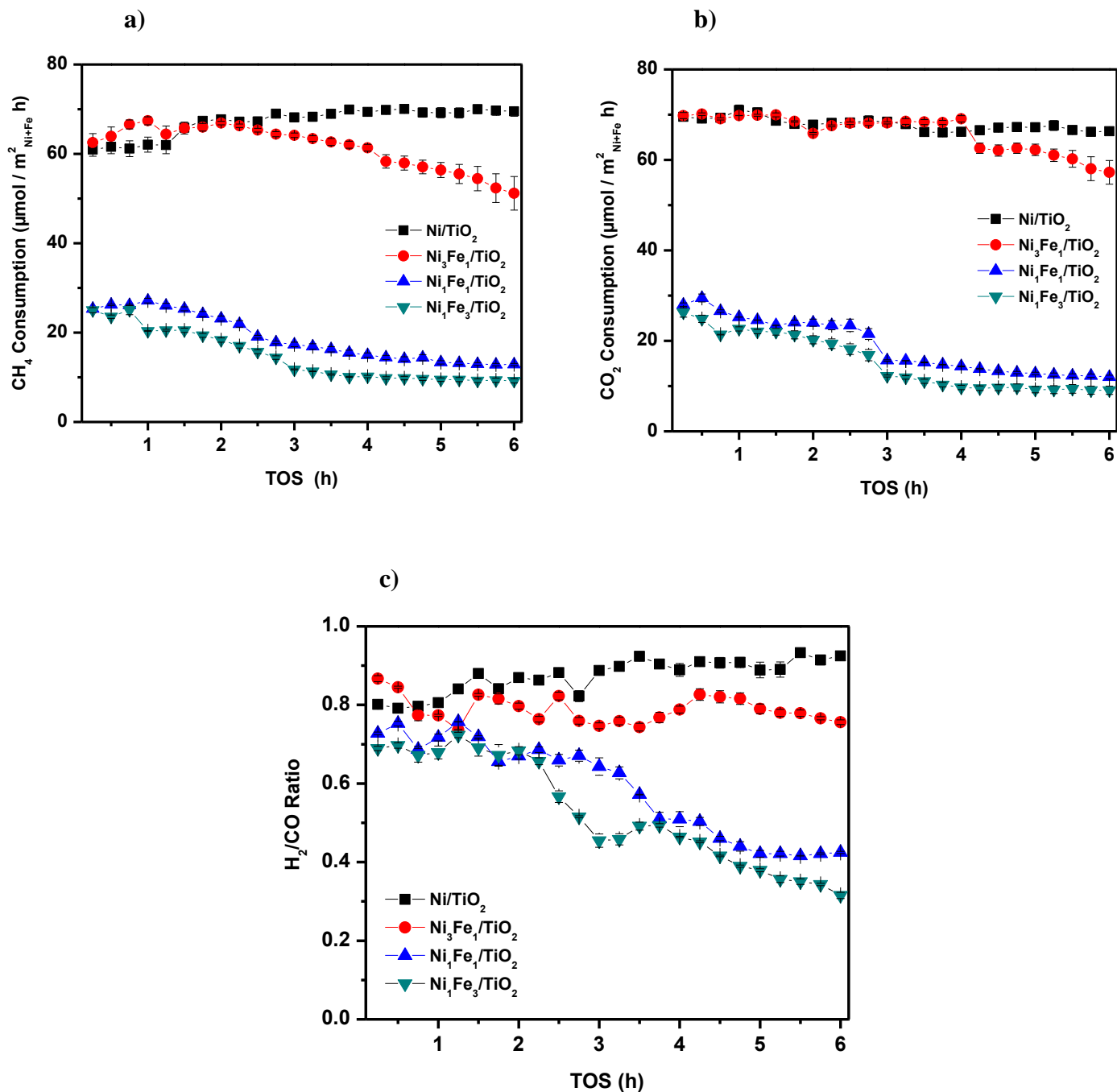
Fig. 3.5. Catalytic activity results of DRM tests over Ni/TiO_2 and $Ni–Fe/TiO_2$ catalysts synthesized by wet-impregnation route: (a) CH_4 consumption, (b) CO_2 consumption, (c) H_2/CO ratio. Reaction Conditions: $10\% CH_4 + 10\% CO_2$ balanced with helium, Temperature: $550 ˚C$.
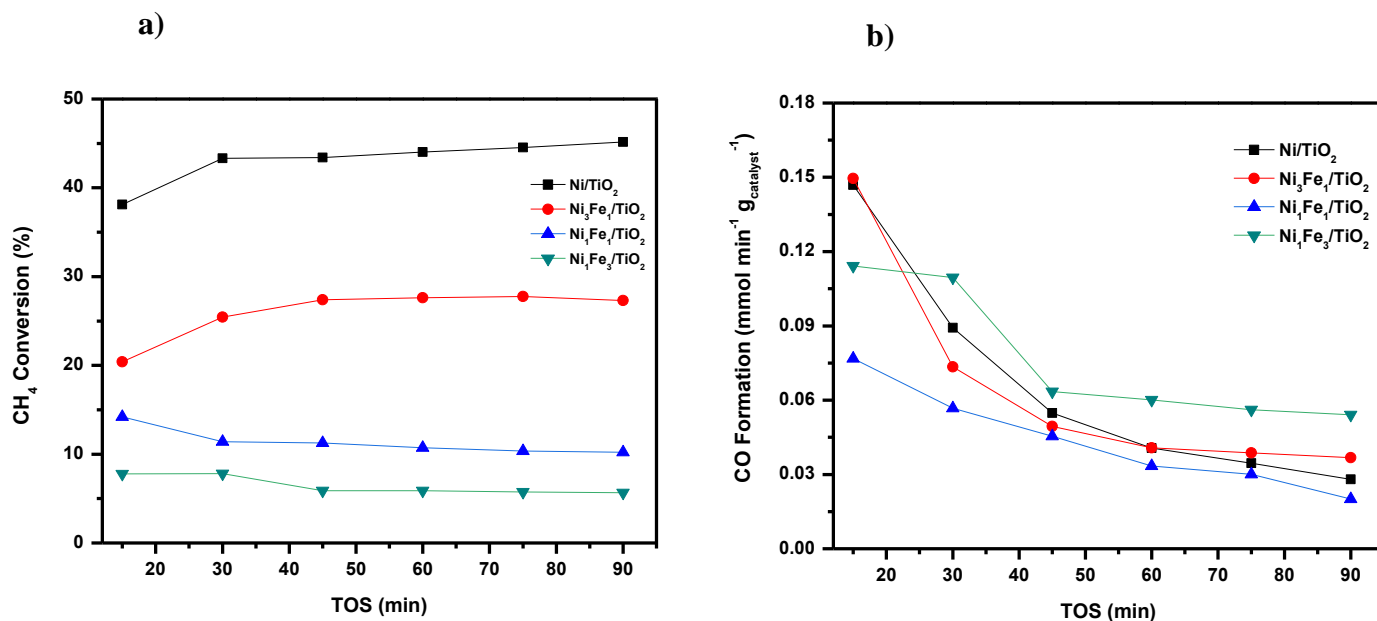
Fig. 3.6. Catalytic activity in steady-state CH_4-decompsoition over Ni/TiO_2 and $Ni\text{-}Fe/TiO_2$ catalysts synthesized by wet-impregnation route, a) CH_4 conversion, and b) CO formation rate (mmol CO $g_{catalyst}$ min^{-1})

3.2.7   Characterizations of used catalysts

3.2.7.1 X-ray Photoelectron Spectroscopy (XPS)

XPS spectra of used catalysts is shown in Fig. 3.7a-d. For all the Ni/TiO_2 and $Ni\text{-}Fe/TiO_2$ catalysts, Ni^0 was observed at 852.7 eV. However, in case of Ni/TiO_2, Ni^{2+} peak appeared at 856.5 eV which exhibited a chemical shift of +1 eV to higher BE values in comparison to reduced Ni/TiO_2. The behavior suggested enhanced interaction of Ni species with the support during DRM reaction [27]. It is postulated that lattice oxygen from the reducible supports including TiO_2 and CeO_2 is consumed at metal-support interface during DRM owing to high mobility of oxygen atoms [37]. Thus, lattice oxygen from TiO_2 support would oxidize coke precursors at metal-support

75

interface to enhance coke removal during reforming reaction. Such process leads to significant interaction between metal and support species thereby shifting the B.E. to high values compared to their reduced counterparts. For Ni_3Fe_1/TiO_2, the Ni^{2+} peak appeared at 856 eV which is 0.5 eV higher than reduced catalysts. It indicated that interaction between Ni species and support were lowered in Ni_3Fe_1/TiO_2 than Ni/TiO_2 in used catalysts. Nevertheless, participation of lattice oxygen from TiO_2 support is also indicated. For, Ni_1Fe_1/TiO_2 and Ni_1Fe_3/TiO_2, Ni^{2+} peak remained at 855.5 eV which implied that there was no significant interaction between Ni species and support during DRM. In other words, lattice oxygen of TiO_2 support in Ni_1Fe_1/TiO_2 and Ni_1Fe_3/TiO_2 did not play significant role in coke removal. However, we attribute carbon gasification over Ni_1Fe_1/TiO_2 and Ni_1Fe_3/TiO_2 by lattice oxygen from FeO_x species only. The Fe 2p spectra of all used Ni-Fe/TiO_2 catalysts demonstrated mixture of Fe^{2+} and Fe^{3+}. Our results showed that Fe^{2+} was oxidized to Fe^{3+} which is attributed to oxophilicity of Fe. Previous studies on Ni-Fe catalysts for DRM also demonstrated oxidation of Fe to FeO_x upon CO_2 exposure [18,19]. Further, O 1s spectra of used catalysts were analyzed to gain insights of different types of oxygen species over used catalysts. It was observed that O 1s spectra of all the Ni/TiO_2 and Ni-Fe/TiO_2 showed 3 peaks upon deconvolution. Peak occurring at 529.7 eV was assigned to O^{2-} in metal oxide [38]. While peaks appearing at 531.5 eV and 533.5 eV are assigned to different types of surface adsorbed oxygen species (SAOS) [38,39]. Presence of SAOS would play important role during DRM and is further demonstrated by reaction mechanism studies using *in-situ* DRIFTS analysis shown in section 3.1. C 1s XPS spectra of Ni/TiO_2 and Ni-Fe/TiO_2 showed a major peak around 284.8 eV which originates due to the adventitious carbon or C–C graphitic type of carbon species. This peak is usually employed for calibration of XPS spectra. Another peak appearing between 286–286.2 eV is assigned to C–O species. Peak between 288.1–288.6 eV is attributed to CO_3^{2-} interacting

with the support [40,41]. The C 1s spectra of used Ni/TiO_2 catalyst shows an additional peak at ~ 290.9 eV binding energy. Such feature has been attributed to graphite or graphitic type carbon species due to $\pi \rightarrow \pi^*$ transitions [41]. However, C 1s peak due to $\pi \rightarrow \pi^*$ transition was not observed in $Ni-Fe/TiO_2$ catalysts. The results suggested coke resistant nature of $Ni-Fe/TiO_2$ catalysts, specifically under applied reaction conditions. The molar composition of surface species after DRM was calculated and is shown in Table 3.5. Notably, Ni^0 concentration in Ni/TiO_2 increased which implied evolution of surface Ni^0 species during reaction. It may be explained that hydrogen produced by CH_4 dissociation during DRM reduced Ni^{2+} to Ni^0. The results of molar composition are also supported by increased CH_4 conversion during DRM over Ni/TiO_2. For $Ni-Fe/TiO_2$ catalysts, molar composition of Ni^0 decreased in comparison to their reduced counterparts. This resulted in decreased Ni/Fe ratio in used catalysts. While, Fe^{2+} was oxidized to mixture of Fe^{2+} and Fe^{3+} in $Ni-Fe/TiO_2$.

Table 3.5. Atomic concentration (%) of surface species in Ni/TiO_2 and $Ni-Fe/TiO_2$ spent catalysts synthesized by wet-impregnation route.

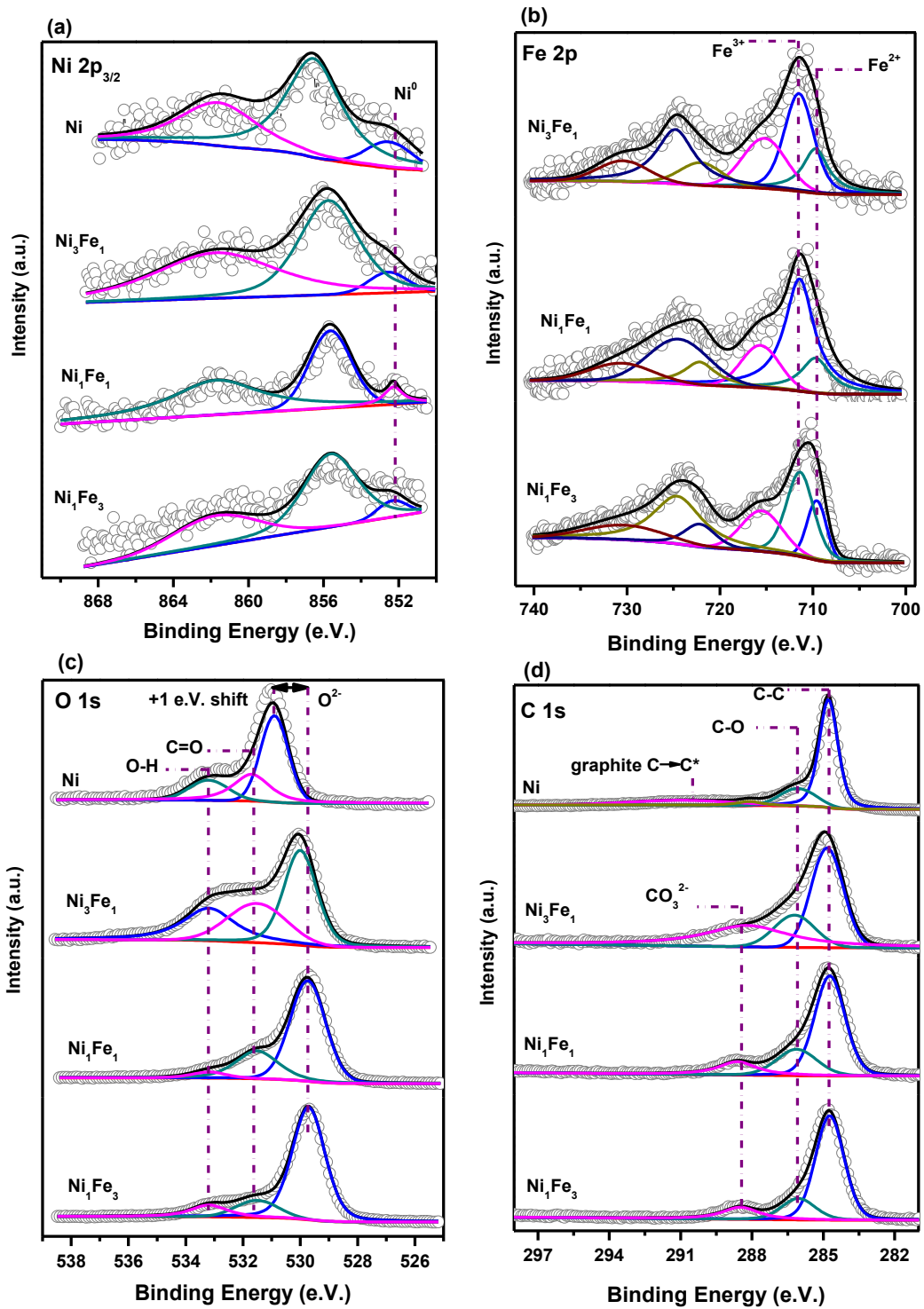| Catalyst	Ni^0	Ni^{2+}	Fe^{2+}	Fe^{3+}	Ni/Fe	O/Ti
Ni/TiO_2	1.91	8.65	-	-	-	0.97
Ni_3Fe_1/TiO_2	0.68	3.69	2.46	4.76	0.60	1.34
Ni_1Fe_1/TiO_2	0.21	1.90	1.27	4.06	0.39	1.60
Ni_1Fe_3/TiO_2	0.11	1.13	1.65	3.80	0.23	1.63

Fig. 3.7 (a) Ni 2p$_{3/2}$, (b) Fe 2p (c) O 1s and (d) C 1s XPS spectra of used catalysts synthesized by wet-impregnation route.
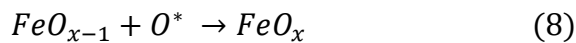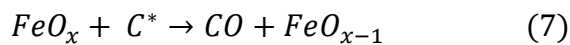
3.2.7.2 Thermogravimetric Analysis (TGA)/Differential Thermogravimetry (DTG)

Catalyst deactivation in dry reforming reaction is usually associated with coke deposition, active-metal sintering and/or agglomeration of metal particles [42]. We applied thermogravimetric analysis to study coke deposition. Analysis of weight percentages of used catalysts is shown in Table 3.6. Fig. 3.8a shows TGA profile of used Ni/TiO_2 catalyst and could be divided into three phases. Phase I (25°C-250°C) depicts the weight loss region which could be due to desorption of physiosorbed moisture. Phase II (250°C-450°C) highlights weight gain that is attributed to the oxidation of metallic species [12,43]. Phase III (450°C-650°C) shows weight loss that is associated with combustion of deposited coke. High temperatures above 450°C for oxidation of carbonaceous species might be required because oxygen atoms cannot be activated by carbon-encapsulated Ni particles [44]. TGA curve of used catalyst revealed 23.4 wt% coke deposition on Ni/TiO_2. CH_4 decomposition and/or CO disproportionation reactions are two main reactions to explain coking formation [45]. To understand the type of deposited coke, 1st derivative of TGA curve was employed. DTG profile of Ni/TiO_2 in Fig. 3.8b showed an asymmetric peak between 475°C-650°C which suggest4 that more than one type of coke may form. The peak centered at 525°C could be due to oxidation of hydrogen containing C species (CH_x) and/or amorphous carbon. Such species do not contribute towards catalyst deactivation. Second peak located around 620°C could be due to oxidation of graphitic carbon which could not be easily gasified as amorphous or CH_x type carbon and thereby contributes in catalyst deactivation [45]. Fig. 3.8c shows TGA curves of bimetallic $Ni–Fe/TiO_2$ catalysts after dry reforming tests. The weight loss in phase I and weight gain in phase II agrees with the findings of Ni/TiO_2. Our results showed that phase III of Ni_3Fe_1/TiO_2 demonstrated only 0.1 wt% coke deposition while Ni_1Fe_1/TiO_2 and Ni_1Fe_3/TiO_2 did not reveal any carbon accumulation. Our observation suggested that Fe might be helpful to

decrease the coke formation. 1st derivative of TGA profile of bimetallic Ni–Fe/TiO$_2$ catalysts was evaluated, shown in Fig. 3.8d. Phase I and phase II shows similar features as of Ni/TiO$_2$. However, absence of peak/s corresponding to phase III in Ni–Fe/TiO$_2$ catalysts suggest that introduction of Fe strongly inhibits carbon deposition. DFT calculations on Ni$_2$Fe overlayer of Ni (111) has revealed that the energy barrier for dissociation of CH fragments to carbon and hydrogen increases upon Fe introduction [46]. It suggested that introduction of Fe might have refrained the dissociation of CH fragments to carbon. This phenomenon would ultimately inhibit the carbon deposition on catalyst surface. Furthermore, if there were any carbon deposited as a result of CO disproportionation (reaction 4), then those carbonaceous species would have been oxidized by FeO$_x$ according to Mars-Van Krevelan mechanism. The coke accumulated in the neighborhood of Ni–Fe species could be oxidized by lattice oxygen from FeO$_x$ [18]. The loss of oxygen atom could be then compensated by reactive oxygen species O* which might be formed by CO$_2$ dissociation.

TGA-DTG analysis of spent catalysts after CH$_4$ decomposition test was performed and results are shown in Fig.3.9. We observed that monometallic Ni/TiO$_2$ catalyst exhibited two types of carbon deposits viz. amorphous and graphitic. While introduction of Fe altered carbon deposition from graphitic to amorphous. Literature studies on TGA analysis of spent Ni catalyst showed that amorphous carbon species did not contributed towards catalyst deactivation. Whereas graphitic coke would cover the active Ni^0 sites during DRM thereby deactivating the catalyst. Thus, alteration of carbon deposits from graphitic to amorphous upon Fe addition would be beneficial to enhance coke resistance in Ni-Fe/TiO$_2$ catalysts.

$$FeO_x + C^* \rightarrow CO + FeO_{x-1} \qquad (7)$$

$$FeO_{x-1} + O^* \rightarrow FeO_x \qquad (8)$$
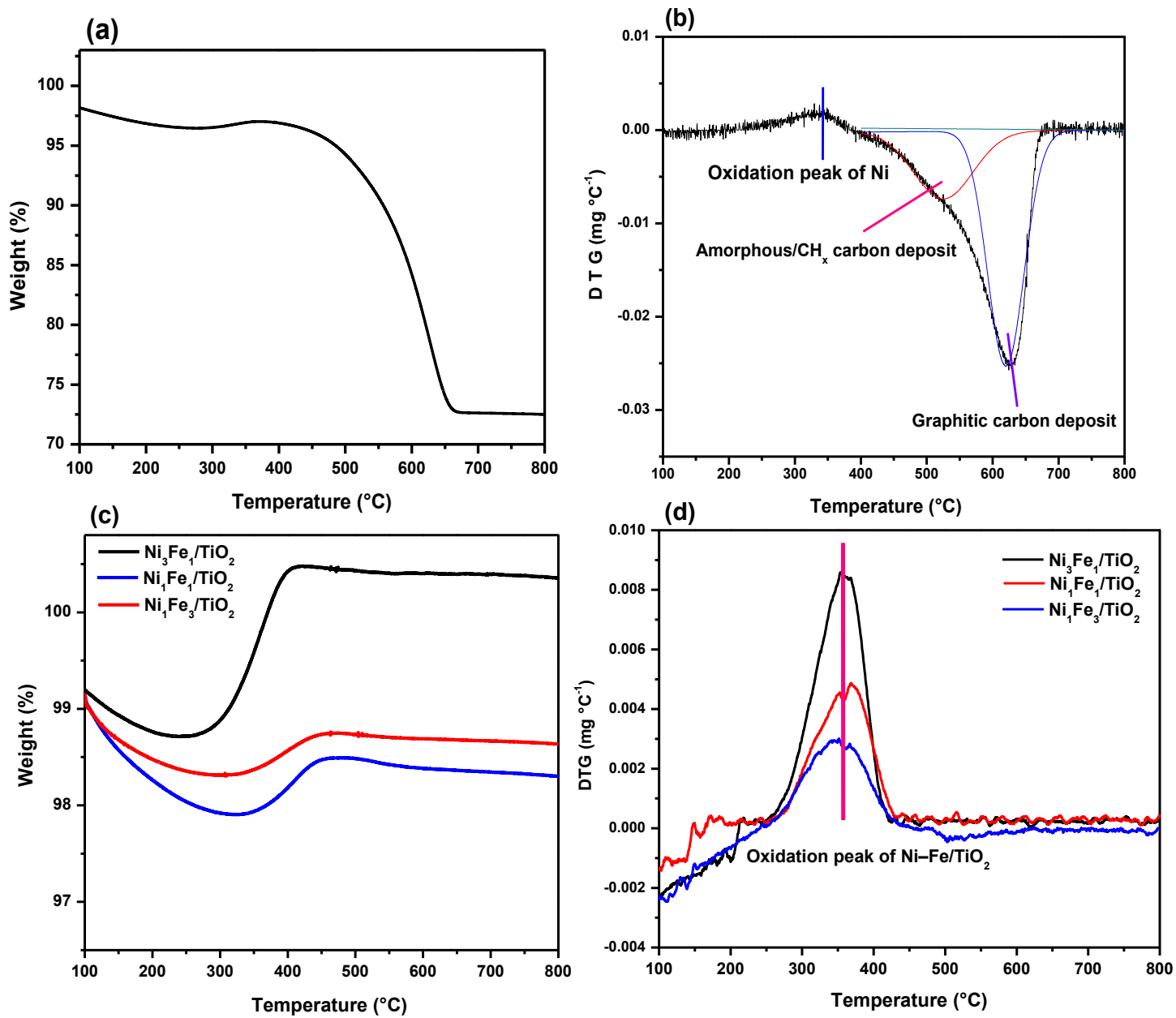
Fig. 3.8. Thermogravimetric analysis (TGA) and Differential Thermogravimetry (DTG) of used catalysts: (a,b) Ni/TiO$_2$, (c,d) Ni–Fe/TiO$_2$.
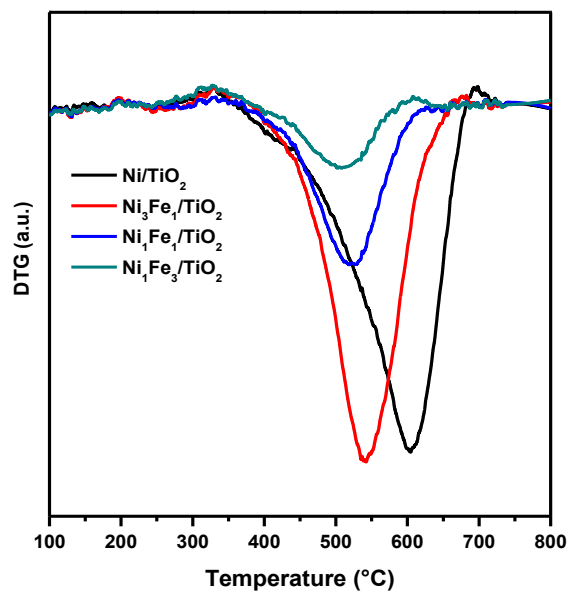
Fig. 3.9. DTG analysis of spent Ni/TiO_2 and Ni-Fe/TiO_2 catalysts synthesized by wet-impregnation route after CH_4 decomposition tests.

Table 3.6. Analysis of TGA/DTG data of used catalysts after DRM.

	Phase I	Phase II	Phase III
Catalyst	Weight loss	Weight gain	Weight loss
	25°C-250°C	250°C -450°C	450°C -650°C
Ni/TiO_2	4.5 %	0.4%	23.4%
Ni_3Fe_1/TiO_2	1.1%	1.7%	0.1%
Ni_1Fe_1/TiO_2	0.7%	1.2%	N.D.
Ni_1Fe_3/TiO_2	0.9%	0.8%	N.D.

3.2.7.3 Raman spectroscopy of used catalysts after DRM

Raman Spectroscopy of used catalysts was performed to estimate graphitic degree of coke on used catalysts. Typically, Raman spectra of used catalysts after dry reforming tests show D and G band of carbon around 1345 cm^{-1} and 1570 cm^{-1} respectively. The D-band is characteristic of amorphous carbon or hydrogen – containing carbon species (CH_x) whereas G-band refers to ordered sp^2 C = C bond in graphite [18,47]. The ratio between D-band intensity and G-band intensity (I_D/I_G) represents degree of crystallinity of deposited coke on catalyst surface. Moreover, degree of crystallinity of coke is associated with its oxidation temperature [18]. Relatively high degree of crystallinity between monometallic Ni and bimetallic Ni-Fe catalysts would suggest high temperature is required to oxidize carbon during dry reforming [18]. Fig. 3.10 shows Raman spectra of used catalysts after DRM test. Only Ni/TiO_2 catalyst demonstrated presence of amorphous and graphitic carbon. The calculated I_D/I_G ratio was 1.00 over Ni/TiO_2 which indicated that amorphous and graphitic carbon species are equally present on catalyst surface. While all the $Ni-Fe/TiO_2$ catalysts did not show Raman bands corresponding to deposited coke. The result indicated introduction of Fe is beneficial to inhibit coke deposition and agrees with TGA-DTG results explained in section 3.2.7.2.
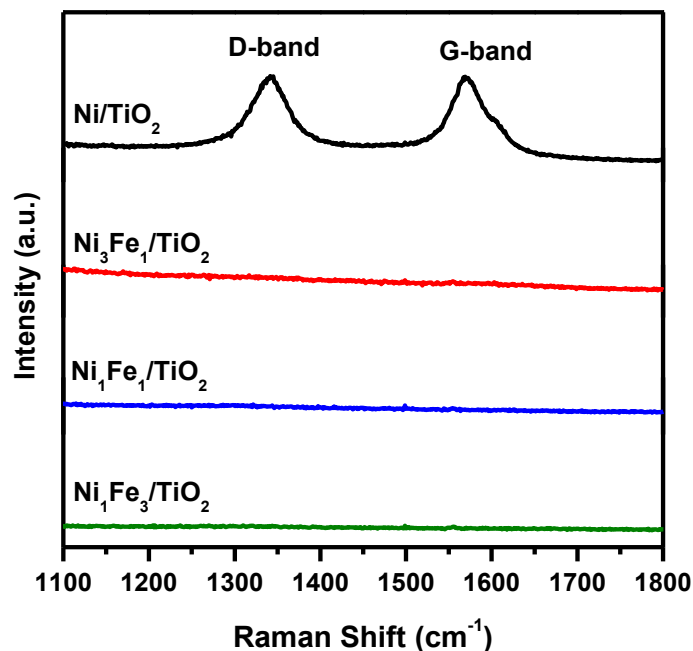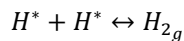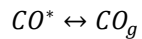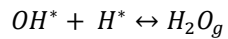
Fig. 3.10. Raman spectra of used Ni/TiO_2 and $Ni-Fe/TiO_2$ catalysts synthesized by wet-impregnation route after DRM.

3.3. *In-situ* DRIFTS analysis over Ni/TiO_2 and Ni_3Fe_1/TiO_2 catalysts

In order to understand reaction mechanism and its intermediates, *in-situ* DRIFTS analysis was performed over *ex-situ* reduced Ni/TiO_2 and Ni_3Fe_1/TiO_2 catalysts. The catalysts were first pretreated with helium at 550°C for 1 h. A pulse of CH_4/He was then introduced into the reaction cell and transient spectra was recorded. Fig.3.11 shows IR spectra during the first pulse of CH_4/He over Ni/TiO_2 catalyst. Peaks appearing at 1304 cm^{-1} and 3015 cm^{-1} are attributed to gas phase CH_4 [1]. The transient spectra recorded after t = 1 min showed peak at 2363 cm^{-1} attributed to gas phase CO_2 [37]. Formation of gas phase CO_2 suggested that lattice oxygen of TiO_2 oxidizes coke precursors originated from CH_4 decomposition. Similar behavior has been previously observed in the literature [37]. While transient spectra from t = 2 min to t = 5 min showed peaks corresponding to formyl species (CHO^*) at 1717 cm^{-1} and formate species ($HCOO^*$) at 1352 cm^{-1} [37,48]. Those

84

peaks indicated oxidation of CH species by lattice oxygen of TiO_2 support. During CO_2/He pulse, peaks related to carbonate species (COO^*) at 1540 cm^{-1} and hydroxyl species (OH^*) at 3735 cm^{-1} [37,49] were observed. Carbonate type intermediate species are suggested to be formed by activation of CO_2 on catalyst surface. However, presence of formyl and hydroxyl species indicated that H^* species formed by CH_4 dissociation facilitated transformation of carbonate species. A 2nd pulse of CH_4/He was followed by CO_2/He pulse. The population of formate species decreased gradually with time which decomposed to hydroxyl species and adsorbed CO located at 1900 cm^{-1} [50] and hydroxyl species. Based on the above discussion, following reaction mechanism is suggested over Ni/TiO_2 catalyst.

$$CH_{4_g} + * \overset{Ni^0}{\longleftrightarrow} CH^*/C^* + 3H^*$$

$$C^* + O_x \leftrightarrow CO_2$$

$$CH^* + O_x \leftrightarrow HCOO^*/CHO^*$$

$$CO_{2_g} \overset{Ni^0}{\longleftrightarrow} COO^*$$

$$COO^* + 2H^* \leftrightarrow CHO^* + OH^*$$

$$HCOO^* \leftrightarrow CHO^* + O^*$$

$$CHO^* \rightarrow CO^* + H^*$$

$$OH^* + H^* \leftrightarrow H_2O_g$$

$$CO^* \leftrightarrow CO_g$$

$$H^* + H^* \leftrightarrow H_{2_g}$$
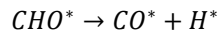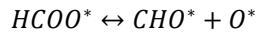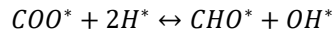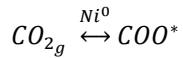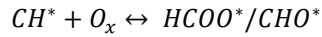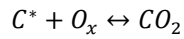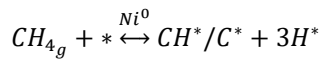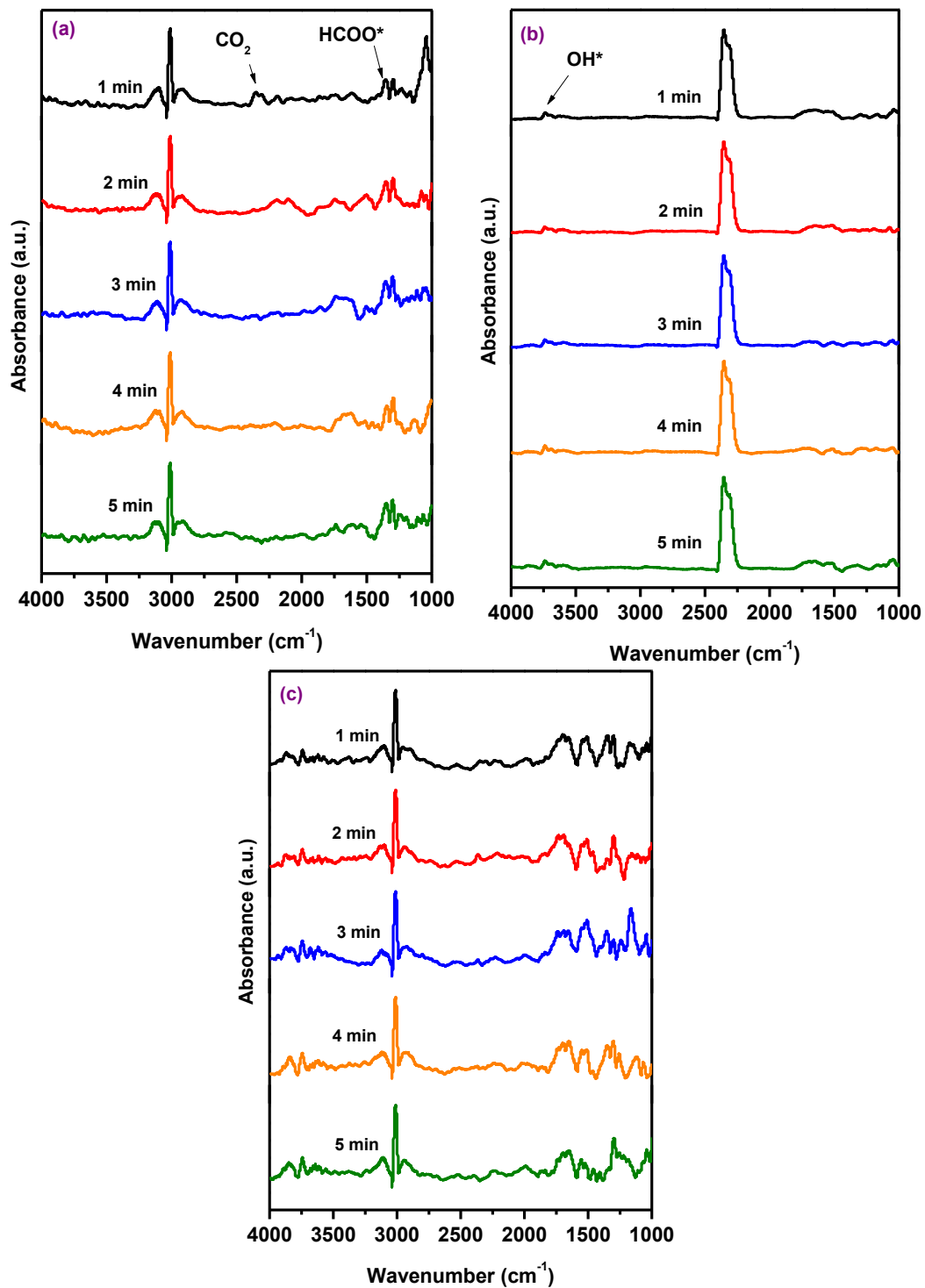
Fig. 3.11. *In-situ* DRIFTS spectra over Ni/TiO_2 catalyst synthesized by wet-impregnation route under alternate pulse at 550˚C. (a) 1st CH_4/He pulse, (b) CO_2/He pulse, (c) subsequent CH_4/He pulse.

The *in-situ* DRIFTS spectra over Ni₃Fe₁/TiO₂ catalyst is shown in Fig. 3.12. During 1ˢᵗ pulse of CH₄/He, peaks related to gas phase CO_2 and formate species (HCOO*) were observed at 2363 cm^{-1} and 1352 cm^{-1} respectively. Those peaks are attributed to oxidation of coke precursors by lattice oxygen from TiO_2 support. The hydroxyl species dominated transiently from t = 2 min to t = 4 min. We attribute the formation of hydroxyl species to reaction between H* and lattice oxygen of FeO_x. Consequently, a dominant peak related to formyl species (CHO*) was observed at t = 5 min with simultaneous disappearance of previously formed hydroxyl species (OH*). This resulted by the reaction between coke precursors with hydroxyl species and is shown in the following equations. CH₄/He pulse was followed by CO₂/He pulse. We observed formyl and carbonate species located at 1717 cm^{-1} and 1540 cm^{-1} respectively which are suggested to be formed by the reaction between carbonates and H*. 2ⁿᵈ pulse of CH₄/He showed transformation of formate to formyl species. Based upon the above discussion, following reaction mechanism is suggested.

$$CH_{4_g} + * \overset{Ni^0}{\longleftrightarrow} CH^*/C^* + 3H^*$$

$$C^* + O_x \leftrightarrow CO_2$$

$$CH^* + O_x \leftrightarrow HCOO^*$$

$$H^* \overset{FeO_x}{\longleftrightarrow} OH^*$$

$$OH^* + C^* \leftrightarrow CHO^*$$

$$HCOO^* \leftrightarrow CHO^* + O^*$$

$$CHO^* \rightarrow CO^* + H^*$$

$$CO^* \leftrightarrow CO_g$$

$$H^* + H^* \leftrightarrow H_{2_g}$$
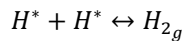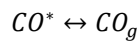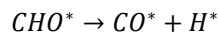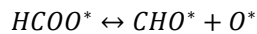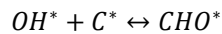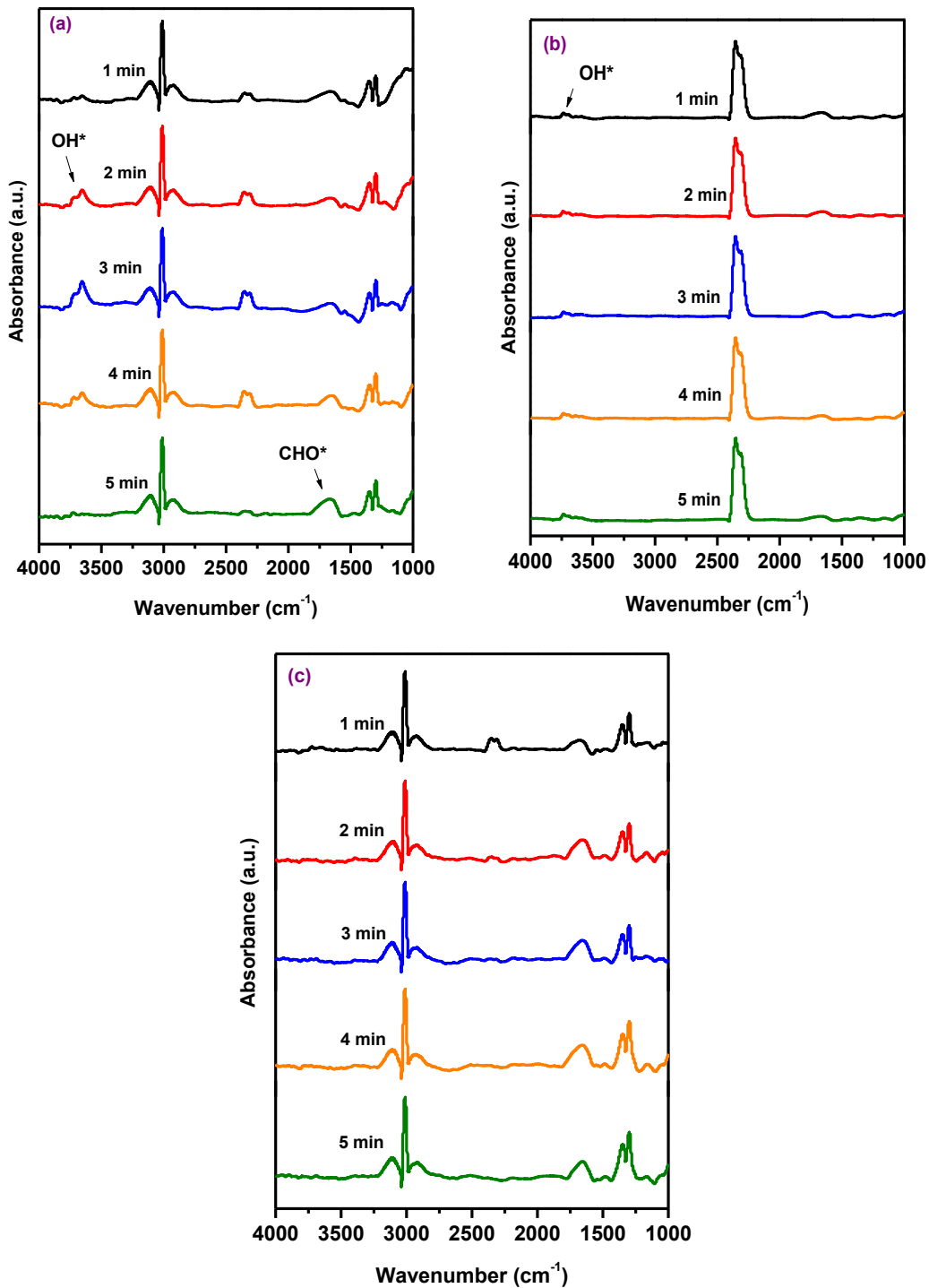
Fig. 3.12. *In-situ* DRIFTS spectra over Ni_3Fe_1/TiO_2 catalyst synthesized by wet-impregnation route under alternate pulse at 550°C. (a) 1st CH_4/He pulse, (b) CO_2/He pulse, (c) subsequent CH_4/He pulse.

3.4 References

[1]   S.M. Kim, P.M. Abdala, M. Broda, D. Hosseini, C. Copéret, C. Müller, ACS Catal. 8 (2018) 2815–2823.

[2]   R.A. Alvarez, D. Zavala-Araiza, D.R. Lyon, D.T. Allen, Z.R. Barkley, A.R. Brandt, K.J. Davis, S.C. Herndon, D.J. Jacob, A. Karion, E.A. Kort, B.K. 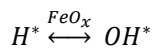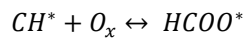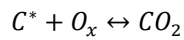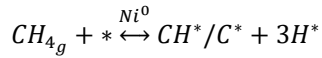Lamb, T. Lauvaux, J.D. Maasakkers, A.J. Marchese, M. Omara, S.W. Pacala, J. Peischl, A.L. Robinson, P.B. Shepson, C. Sweeney, A. Townsend-Small, S.C. Wofsy, S.P. Hamburg, Science 361 (2018) 186–188.

[3]   M.S. Fan, A.Z. Abdullah, S. Bhatia, ChemSusChem 4 (2011) 1643–1653.

[4]   D.L. Trimm, Catal. Today 49 (1999) 3–10.

[5]   H.O. Seo, Catalysts 8 (2018) 110.

[6]   D. Pakhare, J. Spivey, Chem. Soc. Rev. 43 (2014) 7813–7837.

[7]   M. Jafarbegloo, A. Tarlani, A.W. Mesbah, J. Muzart, S. Sahebdelfar, Catal. Lett. 146 (2016) 238–248.

[8]   X. Li, D. Li, H. Tian, L. Zeng, Z.J. Zhao, J. Gong, Appl. Catal. B 202 (2017) 683–694.

[9]   Z. Shang, S. Li, L. Li, G. Liu, X. Liang, Appl. Catal. B 201 (2017) 302–309.

[10]   J. Guo, H. Lou, H. Zhao, D. Chai, X. Zheng, Appl. Catal. A 273 (2004) 75–82.

[11]   T. V Sagar, D. Padmakar, N. Lingaiah, P.S. Sai Prasad, Catal. Lett. 149 (2019) 2597–2606.

[12]   M. Yu, Y.A. Zhu, Y. Lu, G. Tong, K. Zhu, X. Zhou, Appl. Catal. B 165 (2015) 43–56.

[13]   K. Takanabe, K. Nagaoka, K. Nariai, K.I. Aika, J. Catal. 232 (2005) 268–275.

[14]   Q.G. Yan, W.Z. Weng, H.L. Wan, H. Toghiani, R.K. Toghiani, C.U. Pittman, Appl. Catal. A 239 (2003) 43–58.

[15]   S.S. Kim, S.M. Lee, J.M. Won, H.J. Yang, S.C. Hong, Chem. Eng. J. 280 (2015) 433–440.

[16]   Z. Bian, S. Das, M.H. Wai, P. Hongmanorom, S. Kawi, ChemPhysChem 18 (2017) 3117–3134.

[17]   J. Zhang, H. Wang, A.K. Dalai, J. Catal. 249 (2007) 300–310.

[18]   S.M. Kim, P.M. Abdala, T. Margossian, D. Hosseini, L. Foppa, A. Armutlulu, W. Van Beek, A. Comas-Vives, C. Copéret, C. Müller, J. Am. Chem. Soc. 139 (2017) 1937–1949.

[19]   S.A. Theofanidis, V. V. Galvita, H. Poelman, G.B. Marin, ACS Catal. 5 (2015) 3028–3039.

[20]   T. Margossian, K. Larmier, S.M. Kim, F. Krumeich, C. Müller, C. Copéret, ACS Catal. 7 (2017) 6942–6948.

[21]   J. Van De Loosdrecht, A.M. Van Der Kraan, A.J. Van Dillen, J.W. Geus, J. Catal. 170 (1997) 217–226.

[22]   K. Ray, S. Sengupta, G. Deo, Fuel Process. Technol. 156 (2017) 195–203.

[23]   M. Chamoumi, N. Abatzoglou, Can. J. Chem. Eng. 94 (2016) 1801–1808.

[24]   J. Ashok, S. Kawi, Appl. Catal. A 490 (2015) 24–35.

[25]   D. Pandey, G. Deo, J. Ind. Eng. Chem. 33 (2016) 99–107.

[26] A. M. Amin, E. Croiset, W. Epling, Int. J. Hydrogen Energy 36 (2011) 2904-2935.

[27] J. Ashok, S. Kawi, ACS Catal. 4 (2014) 289-301.

[28] K. Song, M. Lu, S. Xu, C. Chen, Y. Zhan, D. Li, C. Au, L. Jiang, K. Tomishige, Appl. Catal. B 239 (2018) 324 – 333.

[29] M. Zhang, J. Zhang, Z. Zhou, S. Chen, T. Zhang, F. Song, Q. Zhang, N. Tsubaki, Y. Tan, Y. Han, Appl. Catal. B 264 (2020) 118522.

[30] S. Damyanova, I. Shtereva, B. Pawelec, L. Mihaylov, J.L.G. Fierro, Appl. Catal. B 278 (2020) 119335.

[31] M. Muhler, R. Schlögl, G. Ertl, J. Catal. 138 (1992) 413–444.

[32] L.R. Winter, E. Gomez, B. Yan, S. Yao, J.G. Chen, Appl. Catal. B 224 (2018) 442–450.

[33] R. Dębek, M. Motak, D. Duraczyska, F. Launay, M.E. Galvez, T. Grzybek, P. Da Costa, Catal. Sci. Technol. 6 (2016) 6705–6715.

[34] R. Dębek, M. Motak, M.E. Galvez, T. Grzybek, P. Da Costa, Appl. Catal. B 223 (2018) 36–46.

[35] S. Sengupta, A. Jha, P. Shende, R. Maskara, A.K. Das, J. Environ. Chem. Eng. 7 (2019) 102911.

[36] M.C.J. Bradford, M.A. Vannice, Catal. Rev. 41 (1999) 1–42.

[37] S. Das, J. Ashok, Z. Bian, N. Dewangan, M.H. Wai, Y. Du, A. Borgna, K. Hidajat, S. Kawi, Appl. Catal. B 230 (2018) 220-236.

[38] K. Sutthiumporn, T. Maneerung, Y. Kathiraser, S. Kawi, Int. J. Hydrogen Energy 37 (2012) 11195-11207.

[39] X. Song, X. Dong, S. Yin, M. Wang, M. Li, H. Wang, Appl. Catal. A 526 (2016) 132-138.

[40] M. Yu, K. Zhu, Z. Liu, H. Xiao, W. Deng, X. Zhou, Appl. Catal. B 148–149 (2014) 177–190.

[41] S.A. Theofanidis, R. Batchu, V. V Galvita, H. Poelman, G.B. Marin, Appl. Catal. B 185 (2016) 42–55.

[42] X. Li, B. Yan, S. Yao, S. Kattel, J.G. Chen, T. Wang, Appl. Catal. B 231 (2018) 213–223.

[43] R.K. Singha, A. Yadav, A. Agrawal, A. Shukla, S. Adak, T. Sasaki, R. Bal, Appl. Catal. B 191 (2016) 165–178.

[44] H. Wu, G. Pantaleo, V. La Parola, A.M. Venezia, X. Collard, C. Aprile, L.F. Liotta, Appl. Catal. B 156–157 (2014) 350–361.

[45] M. Shah, S. Das, A.K. Nayak, P. Mondal, A. Bordoloi, Appl. Catal. A 556 (2018) 137–154.

[46] L.L. Xu, H. Wen, X. Jin, Q.M. Bing, J.Y. Liu, Appl. Surf. Sci. 443 (2018) 515–524.

[47] K. Cao, M. Gong, J. Yang, J. Cai, S. Chu, Z. Chen, B. Shan, R. Chen, J. Catal. 373 (2019) 351–360.

[48] K. Bu, J. Deng, X. Zhang, S. Kuboon, T. Yan, H. Li, L. Shi, D. Zhang, Appl. Catal. B 267 (2020) 118692.

[49] A.L.A. Marinho, F.S. Toniolo, F.B. Noronha, F. Epron, D. Duprez, N. Bion, Appl. Catal. B 281 (2021) 119459.

[50] Y. Wang, L. Yao, Y. Wang, S. Wang, Q. Zhao, D. Mao, C. Hu, ACS Catal. 8 (2018) 6495-6506.

Chapter 4

Bimetallic Ni-Fe/TiO$_2$ catalysts derived from hydrotalcite type precursors for low temperature dry reforming of methane

4.1 Introduction

Dry (CO$_2$) reforming of methane (DRM), $CH_4 + CO_2 \rightarrow 2CO + 2H_2$, converts two major greenhouse gases in one single reaction to produce synthesis gas – a mixture of H$_2$ and CO [1-3]. DRM offers H$_2$/CO ratio close to unity at high temperature (>800˚C) and atmospheric pressure. Nearly equimolar mixture of H$_2$ and CO could be utilized in downstream processes such as F–T synthesis [4,5]. Precious metals including Pt, Ru, Rh, Pd and Ir [6-10] based catalysts have been extensively studied for dry reforming of methane. But the practical application is hurdled by the high cost related to precious metals. Meanwhile Ni based catalysts show comparable activity to precious metals in DRM [11]. Ni based catalysts are economically preferred over precious metals but are prone to deactivation caused by metal oxidation [12], metal sintering [13,14] and coke deposition [15,16]. Coke deposition has been considered as primary reason for catalyst deactivation [17]. Both methane decomposition, $CH_4 \rightarrow C + 2H_2$, and CO disproportionation, $2CO \rightarrow C + CO_2$, contribute to the formation of carbon.

Ni based bimetallic catalysts have been studied to reduce coke formation. The addition of transition metals such as Fe, Co or Cu to Ni based catalysts have been proved as one cost-effect approach to decrease the deactivation [18-20]. Bimetallic catalysts improve Ni dispersion and reducibility compared to monometallic catalysts [21]. Highly dispersed and small–sized Ni

particles have been shown to preferentially favor DRM over methane decomposition and CO disproportionation [22,23].

Fe is favored as potential promoter in Ni catalysts because of its abundance. Kim et al. [24,25] studied Ni-Fe/MgAl$_2$O$_4$ catalysts for DRM. They reported FeO formation upon CO$_2$ exposure during DRM. FeO facilitated oxidation of coke to CO. Theofanidis et. al [26] also investigated Ni-Fe/MgAl$_2$O$_4$ catalysts and suggested that lattice oxygen from FeO$_x$ oxidized coke to CO. The origin of FeO$_x$ resulted from in-situ reduction of Ni-Fe alloy during the reaction. Further, Theofanidis et. al [27] deduced that location of Fe in Ni catalysts played one important role in coke resistance. Specifically, incorporation of Fe into the support lattice of Ni/MgFe$_x$Al$_{2-x}$O$_4$ proved better than Fe deposited onto the support as Ni-Fe/MgAl$_2$O$_4$. Hydrogen spillover during reduction facilitated partial migration of Fe from MgFe$_x$Al$_{2-x}$O$_4$ spinel to form surface Ni-Fe alloy. Ni-Fe alloy together with MgFe$_x$Al$_{2-x}$O$_4$ showed no coke deposition under atmospheric DRM conditions. On the other hand, alloying Fe with Ni catalyst over ordered mesoporous Al$_2$O$_3$ support did not improve coke resistance [28]. The structure of catalysts is also important [29,30]. Ni–Fe perovskite catalysts were studied for DRM reaction [31,32]. Partial substitution of Ni by Fe in the LaNiO$_3$ perovskite resulted in enhancement of structure stability and coke resistance. LaNi$_{0.5}$Fe$_{0.5}$O$_3$ perovskite showed smaller particle size and better dispersion than LaNiO$_3$. However, catalytic activity was decreased in LaNi$_{0.5}$Fe$_{0.5}$O$_3$ [32]. Contrarily, La$_2$O$_3$ supported Ni–Fe catalysts obtained by the reduction of LaNi$_{0.8}$Fe$_{0.2}$O$_3$ – type perovskite did not show activity [33]. Ni and Fe dealloyed during reaction and Fe oxidized to FeO$_x$. FeO$_x$ was converted to LaFeO$_3$ perovskite – which encapsulated active Ni particles. The role of Fe in Ni-Fe/MgO catalyst was proposed to facilitate formation of small Ni ensembles and promote coke gasification [34].

It should be noted that DRM studies entailed above were performed at high temperatures ($\geq$ 650°C). Thermodynamically, coke formation dominates at low temperature (< 600°C) during DRM [35]. Thus, inexpensive Ni–Fe catalysts which are active and coke resistant at low temperature are also desirable. Hydrotalcites (HTLs) ($[M^{2+}_{1-x}M^{3+}_x(OH)_2]^{x+}(A^{n-}_{x/n}){\cdot}mH_2O$) are built by periodic stacking of two-dimensional brucite like sheets consisting of divalent and trivalent metal ions [36,37]. Mixed metal oxides (MMOs) formed upon calcination of HTLs are suggested as suitable precursors for synthesis of homogeneous Ni–Fe nanoparticles [38].

In this study, we study the role of Fe in the bimetallic Ni–Fe/TiO_2 catalysts synthesized from HTLs precursors in low temperature DRM (550°C). Reducibility and accessible metallic sites of Ni and Ni–Fe catalysts were investigated by H_2–TPR and CO-chemisorption respectively. Effect of Fe addition on transient activity of CH_4 and CO_2 was studied by CH_4–TPSR/DTG and CO_2–TPSR/H_2–TPR respectively. XPS analysis was used to determine oxidation state and concentration of surface species in reduced and spent catalysts. TGA–DTG, Raman spectroscopy and XPS were employed to characterize spent catalysts. Reaction mechanism and its intermediates were studied using *in-situ* DRIFTS analysis.

4.2. Results and Discussion

4.2.1 Hydrogen – Temperature programmed reduction (H₂-TPR)

Hydrogen–temperature programmed reduction (H_2-TPR) was employed to study the reducibility of supported Ni, Fe and Ni-Fe catalysts and metal-support interaction. We conducted peak deconvolution analysis to gain insights of reduction process. Fig.4.1 shows H_2-TPR profiles of Ni/TiO_2, Fe/TiO_2 and Ni-Fe/TiO_2 catalysts. For monometallic Ni/TiO_2, peaks occurring at 216°C and 243°C are assigned to the reduction of bulk NiO which does not interact with TiO_2

support. While peak located at 320˚C is identified to the reduction of well dispersed NiO species having significant interaction with the support (NiO-TiO$_2$) to Ni^0 [39]. Yan et. al reported the reduction of strongly interacting NiO species with TiO$_2$ support occurred at 390˚C. The Ni/TiO$_2$ catalysts in the study by Yan et. al [39] were synthesized by impregnation method. Comparison between our H$_2$-TPR results and those from Yan et. al [39] suggested better reducibility of Ni/TiO$_2$ catalysts synthesized by hydrotalcite route than impregnation approach. The argument of better reducibility of Ni/TiO$_2$ is attributed to low reduction temperature of NiO species. The H$_2$ consumption related to reduction of bulk NiO in Ni/TiO$_2$ is higher than NiO-TiO$_2$ interacting species. It suggested that bulk NiO dominates in Ni/TiO$_2$ catalyst. For Ni/ZrO$_2$ catalysts, it was mentioned that low temperature reduction peaks (< 400˚C) were assigned to bulk NiO. While, strongly interacting NiO species reduced at high temperature (> 500˚C) [40,41]. The difference in reduction temperature between Ni/TiO$_2$ reported here and Ni/ZrO$_2$ catalysts [40,41] is related to different metal-support interaction. H$_2$-TPR profile of Fe/TiO$_2$ catalyst showed 3 distinct reduction peaks. Peak occurring at 270˚C is attributed to reduction of Fe$_2$O$_3$ → Fe$_3$O$_4$. While peaks located at 365˚C and 560˚C are attributed to reduction of Fe$_3$O$_4$ → FeO → Fe^0 respectively. The three step reduction profile of Fe/TiO$_2$ catalyst is supported by with literature reports [42,43]. It should be noted that Fe/TiO$_2$ did not show presence of interacting Fe$_2$O$_3$ species with TiO$_2$ support, unlikely Ni/TiO$_2$. The argument is supported by Gao et. al [44] who also showed absence of interacting Fe$_2$O$_3$ species with TiO$_2$ support.

H$_2$-TPR profiles of bimetallic Ni–Fe/TiO$_2$ catalysts are distinctly different from their monometallic counterparts. For all Ni-Fe/TiO$_2$ catalysts, peak 1 located at 216˚C is assigned to reduction of non-interacting bulk NiO species. Whereas, peak 2 located around 265˚C is assigned to reduction of strongly interacting NiO-TiO$_2$ species in Ni$_3$Fe$_1$/TiO$_2$, Ni$_1$Fe$_1$/TiO$_2$ and

Ni_1Fe_3/TiO_2 catalysts. H_2 consumption corresponding to reduction of bulk NiO species decreased in Ni-Fe/TiO_2 catalysts compared to Ni/TiO_2 catalysts. The results imply introduction of Fe inhibited formation of bulk NiO species. Secondly, H_2 consumption corresponding to reduction of strongly interacting NiO-TiO_2 species increased from 0.63 mmol $H_2/g_{catalyst}$ to 1.6 mmol $H_2/g_{catalyst}$ in Ni/TiO_2 and Ni_3Fe_1/TiO_2 respectively. It indicated reduction of $Fe_2O_3 \rightarrow Fe_3O_4 \rightarrow FeO$ also occurred simultaneously with NiO-TiO_2 reduction around 265˚C. In other words, peak located around 265˚C also suggested bimetallic Ni – Fe interaction. The peak at 310˚C is assigned to reduction of $FeO \rightarrow Fe^0$ in Ni_3Fe_1/TiO_2 and Ni_1Fe_1/TiO_2. Furthermore, increasing Fe loading from 2.5 wt% to 5 wt% decreased H_2 consumption attributed to peak 2. The results indicated that reduction of $Fe_2O_3 \rightarrow Fe_3O_4 \rightarrow FeO$ is inhibited in Ni_1Fe_1/TiO_2. We attribute this behavior to decrease in amount of Ni^0 formed in peak 2. Ni^0 has been shown to promote H_2 spill over on catalyst surface [39]. Accordingly, unreduced FeO at 265˚C will be reduced at 310˚C. The explanation holds for increase in H_2 consumption in peak 3 in Ni_1Fe_1/TiO_2 compared to Ni_3Fe_1/TiO_2. In Ni_1Fe_3/TiO_2 catalyst, amount of Ni^0 is further decreased. Therefore, reduction of iron oxide is inhibited. A new peak occurred at 365˚C is assigned to reduction of $FeO \rightarrow Fe^0$. Therefore, reduction of $Fe_2O_3 \rightarrow Fe_3O_4$ occurred at 265˚C and $Fe_3O_4 \rightarrow FeO$ occurred at 310˚C in Ni_1Fe_3/TiO_2. In other words, reduction of Fe_2O_3 in Ni_1Fe_3/TiO_2 resembled a three step reduction process alike monometallic Fe/TiO_2. Similar TPR profile of bimetallic Ni–Fe/TiO_2 catalysts has been reported in the literature [45]. However, reduction temperature related to NiO and Fe_2O_3 in Ni/TiO_2, Fe/TiO_2 and Ni–Fe/TiO_2 catalysts differ from our results. This behavior is attributed to difference in catalyst preparation and calcination procedure which altered metal-support interactions.
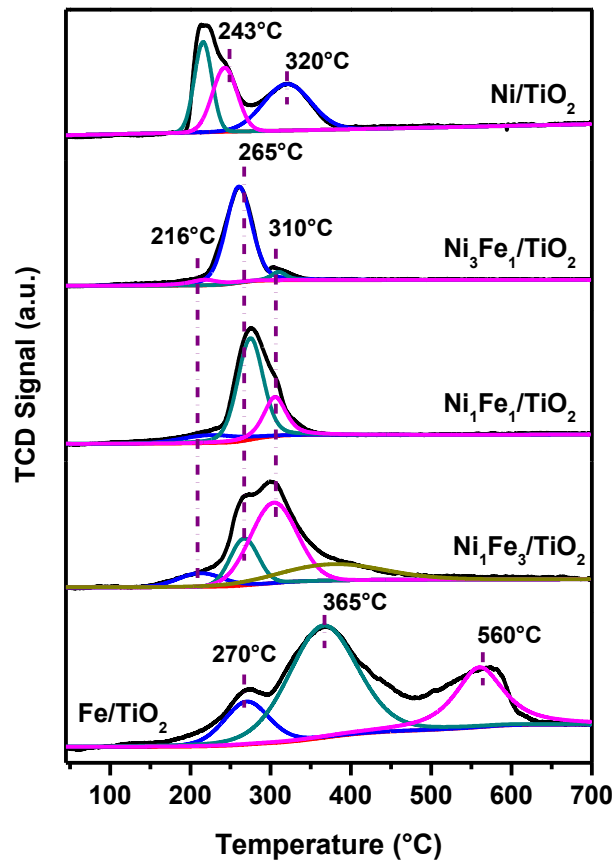
Fig.4.1. H₂-TPR profiles of Ni/TiO₂, Ni-Fe/TiO₂ and Fe/TiO₂ catalysts synthesized by hydrotalcite route.

Table 4.1. Analysis of H₂-TPR profiles of Ni/TiO₂, Ni–Fe/TiO₂ and Fe/TiO₂ catalysts synthesized by hydrotalcite route.

Catalyst	Peak Temperature (°C) and H₂–Consumption (mmol H₂/g_catalyst)				
	Peak 1	Peak 2	Peak 3	Peak 4	Total H₂ consumption
Ni/TiO₂	216 (0.46)	243 (0.46)	320 (0.63)	-	1.55
Ni₃Fe₁/TiO₂	216 (0.14)	265 (1.6)	310 (0.09)	-	1.83
Ni₁Fe₁/TiO₂	216 (0.14)	265 (1.22)	310 (0.54)	-	1.9
Ni₁Fe₃/TiO₂	216 (0.14)	265 (0.37)	310 (0.88)	365 (0.63)	2.02
Fe/TiO₂	270 (0.38)	365 (1.53)	560 (0.73)	-	2.64

4.2.2 Pulse CO-Chemisorption

Table 4.2 shows CO uptake values over reduced catalysts. Typically, CO uptake values are correlated with number of metallic sites on catalyst surface with the assumption that each CO molecule chemisorbs one metallic site. For monometallic Ni/TiO_2 catalyst, the CO uptake is 10.2 $\mu mol/g$. However, monometallic Fe/TiO_2 showed only 1.1 $\mu mol/g$ of chemisorbed CO. The chemisorption values indicated Ni/TiO_2 contains essentially higher metallic sites than Fe/TiO_2. Consequently, addition of Fe inhibited formation of metallic sites and results are reflected by decreased CO uptake values. The CO uptake values decreased from 9.0 to 4.9 $\mu mol/g$ in Ni_3Fe_1/TiO_2 and Ni_1Fe_3/TiO_2.

Table 4.2. CO uptake values over Ni/TiO_2, Ni-Fe/TiO_2 and Fe/TiO_2 catalysts synthesized by hydrotalcite route.

Catalyst	CO Adsorbed ($\mu mol/g$)
Ni/TiO_2	10.2
Ni_3Fe_1/TiO_2	9.0
Ni_1Fe_1/TiO_2	5.3
Ni_1Fe_3/TiO_2	4.9
Fe/TiO_2	1.1

4.2.3 Methane – Temperature programmed surface reaction/Differential thermogravimetry (CH_4-TPSR/DTG)

CH_4-TPSR/DTG could provide understanding on CH_4 activity towards catalyst surface and type of carbon species formed during CH_4 decomposition. Fig. 4.2a shows CH_4-TPSR profile over Ni/TiO_2 and Ni-Fe/TiO_2 and Fe/TiO_2 catalysts. For Ni/TiO_2, it is observed that CH_4 activates at

temperature as low as 350°C and its transient activity increases up to 495°C. However, monometallic Fe/TiO_2 did not show transient activity towards CH_4. The results indicated Fe/TiO_2 is inactive towards CH_4 and agrees with literature [26,27]. While bimetallic $Ni-Fe/TiO_2$ catalysts showed similar CH_4-TPSR profiles in comparison to Ni/TiO_2. CH_4 dissociation initiated around 350°C and peaked around 495°C. It is interesting to note that CH_4 dissociation over $Ni-Fe/TiO_2$ catalysts is much lower than monometallic Ni/TiO_2 albeit similar activation and peak temperatures. Accordingly, comparison of TCD signal intensity in CH_4-TPSR profiles suggest that introduction of Fe inhibits CH_4 dissociation activity. This behavior could be beneficial during DRM to avoid coke deposition resulting from CH_4 cracking. Similar CH_4-TPSR profiles as discussed in this study have been shown over $Ni/Mg(Al)O$, $Co/Mg(Al)O$ and $Ni-Cu/Mg(Al)O$ catalysts [46,47]. It was demonstrated that CH_4 decomposition could be initiated around 350°C over $Ni/Mg(Al)O$ and increased up to 534°C [47]. Whereas, CH_4 decomposition over $Co/Mg(Al)O$ initiated around 400°C and peaked up to 572°C [47]. However, for $Ni-Cu/Mg(Al)O$ catalyst, the CH_4 decomposition initiated around 412°C and increased up to 624°C [46]. The differences in our results compared to the reported data could emanate from differences in metal-support interaction, reducibility and/or metal dispersion.

DTG was performed in order to gain insights on type and reactivity of carbon formed during CH_4-TPSR tests. As shown in Fig. 4.2b, Ni/TiO_2 and $Ni-Fe/TiO_2$ catalysts showed DTG peak at 530°C suggesting formation of amorphous type of carbon during CH_4-TPSR [48]. Based upon similar DTG peak temperatures of Ni/TiO_2 and $Ni-Fe/TiO_2$ catalysts, it is inferred that introduction of Fe does not influence the type of carbon formed during CH_4 dissociation. Considering the DTG intensity of used catalysts after CH_4-TPSR tests, the amount of carbon species formed are greatly decreased in presence of Fe. The behavior is ascribed to inactivity of Fe towards CH_4 in Ni-Fe

catalysts which lowers CH_4 dissociation. On the other hand, addition of Cu in Ni/MgAlO catalyst did not affect the amount of carbon formed during CH_4-TPSR [46].
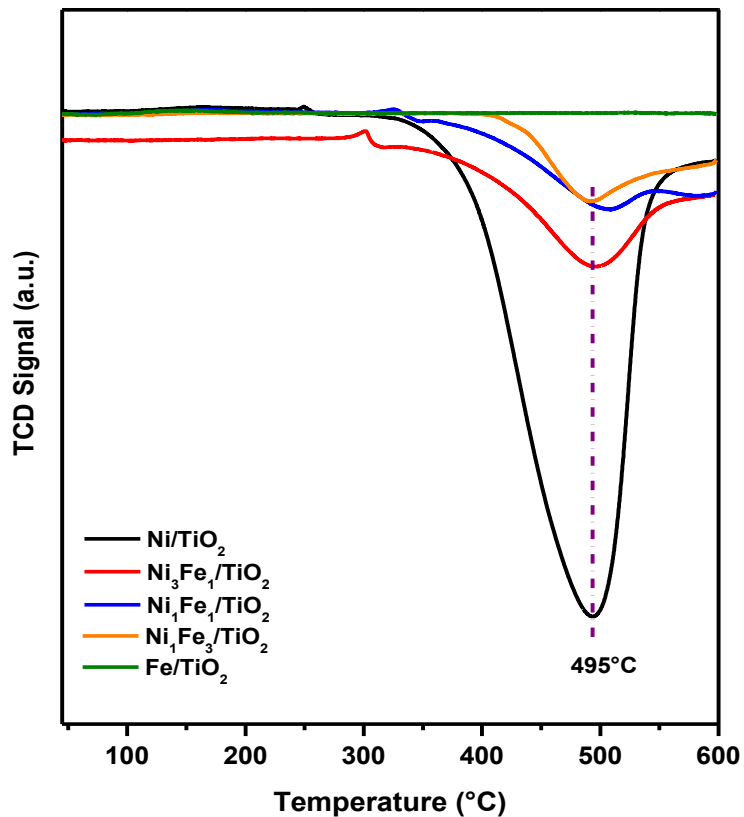

Fig. 4.2a. CH_4-TPSR profiles of Ni/TiO$_2$, Ni-Fe/TiO$_2$ and Fe/TiO$_2$ catalysts synthesized by hydrotalcite route.
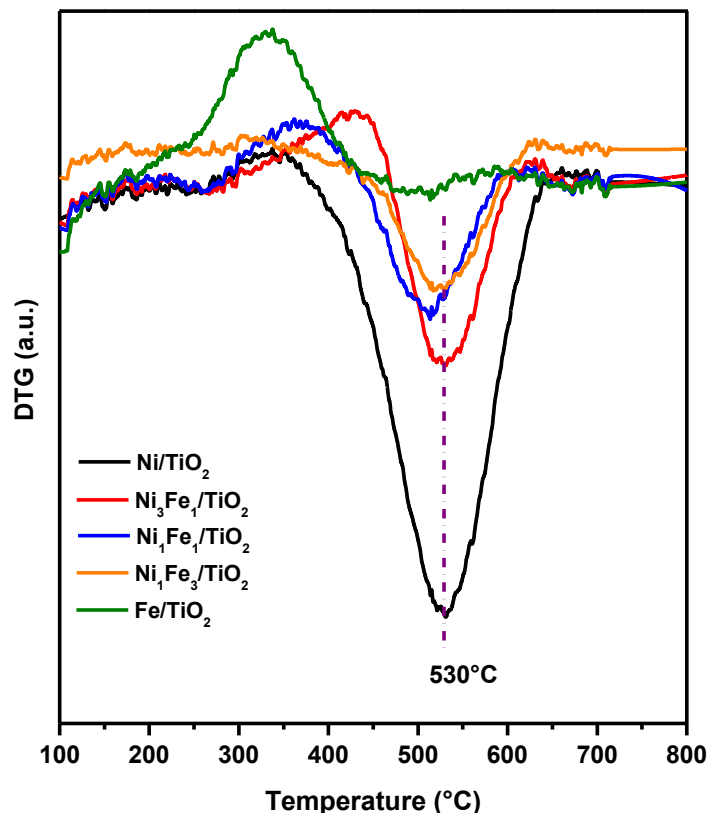
Fig. 4.2b. DTG profiles of Ni/TiO_2, $Ni-Fe/TiO_2$ and Fe/TiO_2 catalysts synthesized by hydrotalcite route after CH_4-TPSR tests.

4.2.4 Carbon dioxide – Temperature programmed surface reaction/Hydrogen – Temperature programmed reduction (CO_2-TPSR/H_2-TPR)

Activation and thereby dissociation CO_2 to CO^* and O^* is beneficial during DRM. The O^* species reacts with CH_x species derived from CH_4 decomposition to produce CO and H_2. Moreover, CO_2-TPSR/H_2-TPR could also provide understanding on the nature of active centers on catalyst surface to dissociate CO_2 to CO^* and O^* [49]. Thus, CO_2-TPSR/H_2-TPR is performed over reduced catalysts to gain insights on CO_2 dissociation. CO_2-TPSR/H_2-TPR over reduced catalysts could be described according to following equations.

$$CO_2 \rightarrow CO^* + O^* \quad (1)$$

$$O^* + H_2 \rightarrow H_2O \quad (2)$$
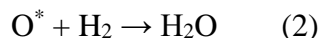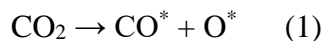
Dissociation of CO_2 on active metal or interface between active-metal and support forms CO^* and surface adsorbed oxygen species O^*. Formed O^* species are then characterized by H_2-TPR. The H_2 consumed in the TPR is directly correlated to O^* species formed during CO_2 dissociation according to equation 1 and 2. Fig. 4.3 shows H_2-TPR profiles of reduced Ni/TiO_2, Ni-Fe/TiO_2 and Fe/TiO_2 catalysts after performing CO_2-TPSR tests. Ni/TiO_2 catalyst showed three distinct H_2 consumption peaks. Reduction of O^* formed during CO_2-TPSR begins nearly at 90°C and peaks up to 495°C, together with a small shoulder appearing at 355°C. All three peaks are attributed to active Ni^0 centers in Ni/TiO_2 catalyst. For Fe/TiO_2 catalyst, there is no low temperature peak unlike Ni/TiO_2 catalyst. Interestingly, the H_2-TPR profile of Fe/TiO_2 after CO_2-TPSR showed a strong H_2 consumption peak above 700°C. This result indicated strong ability of Fe/TiO_2 to effectively dissociate CO_2 to CO^* and O^*. Accordingly, the O^* reduction peaks of Ni-Fe/TiO_2 catalysts after CO_2-TPSR shifted to higher temperature than Ni/TiO_2 catalyst. Ni_3Fe_1/TiO_2 showed a small peak at 115°C, a broad peak around 545°C and a shoulder peak at 435°C. For all the Ni-Fe/TiO_2 catalysts, peaks located below 600°C are assigned to Ni^0 centers. Whereas, peak appearing above 600°C is related to Fe^0 sites. Comparison between O^* reduction peak temperatures of Ni/TiO_2 and Ni-Fe/TiO_2 catalysts suggested that introduction of Fe enhanced the adsorption of O^* species formed from CO_2 dissociation. In other words, addition of Fe would promote gasification of coke formed from CH_4 decomposition during DRM. Similar CO_2-TPSR/H_2-TPR profile of $Ni/Mg(Al)O$ and Ni-$Cu/Mg(Al)O$ catalyst has been reported [46]. However, it was demonstrated that introduction of Cu in $Ni/Mg(Al)O$ catalyst would shift O^* reduction peak to lower temperature

than monometallic Ni/Mg(Al)O. Compared to our results, shifting of O^* desorption to low temperature could be related to difference in addition of promoting metal or metal-support interactions. To gain further information on O^* formation, H_2 consumption during H_2-TPR after CO_2-TPSR was calculated. As shown in Table 4.3, the amount of H_2 consumed increased upon Fe addition. This result suggested that introduction of Fe would promote CO_2 dissociation to CO^* and O^* at least under current experimental conditions.
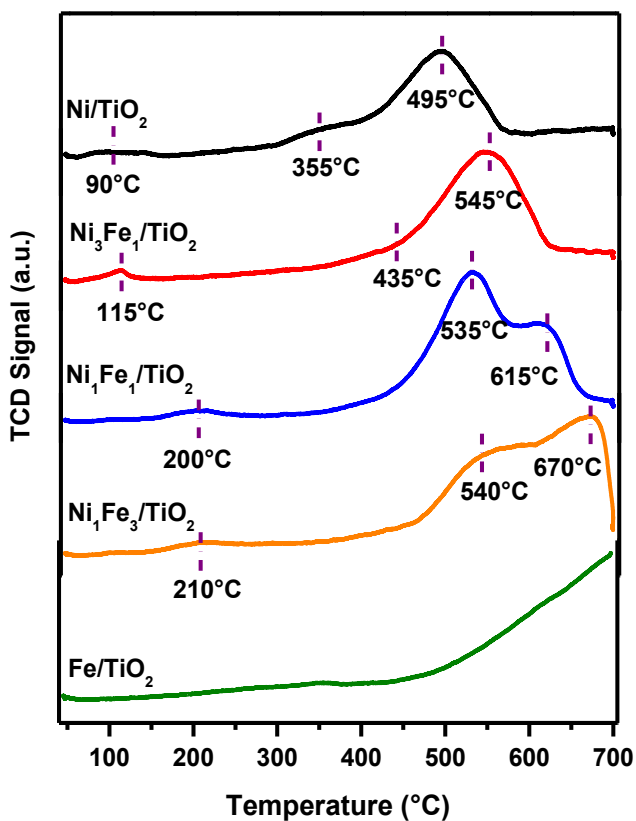

Fig. 4.3. H_2-TPR profiles of Ni/TiO$_2$, Ni-Fe/TiO$_2$ and Fe/TiO$_2$ catalysts synthesized by hydrotalcite route after CO_2-TPSR test.

Table 4.3. H_2 consumption during H_2-TPR after CO_2-TPSR tests over Ni/TiO$_2$, Ni-Fe/TiO$_2$ and Fe/TiO$_2$ catalysts synthesized by hydrotalcite route

Catalyst	H_2 Consumption (mmol $g_{(catalyst)}^{-1}$)
Ni/TiO$_2$	0.97
Ni$_3$Fe$_1$/TiO$_2$	1.65
Ni$_1$Fe$_1$/TiO$_2$	2.76
Ni$_1$Fe$_3$/TiO$_2$	3.05
Fe/TiO$_2$	-

4.2.5 XPS analysis of reduced catalysts

XPS analysis was performed to study the surface species in the reduced Ni/TiO$_2$ and Ni-Fe/TiO$_2$ catalysts. Peak deconvolution of Ni $2p_{3/2}$ XPS spectra is shown in Fig. 4.4a. For Ni/TiO$_2$ catalyst, the peak located at 852.7 eV is assigned to $2p_{3/2}$ orbital-split of Ni^0 [28]. The peak observed at 855.6 eV is attributed to Ni^{2+} $2p_{3/2}$ present as NiO while its satellite peak appears at 861.4 eV [50]. Generally, Ni^{2+} peak is located around 854.4 eV in Ni-based catalysts. However, a shift of +1.2 eV in NiO indicated decreased electron density of Ni^{2+}. Specifically, electron transfer from Ni^{2+} at metal-support interface would result due to interaction between NiO and TiO$_2$ [50,51]. The observation agrees with H_2-TPR analysis of Ni/TiO$_2$ which demonstrated metal-support interactions between NiO and TiO$_2$. For all Ni-Fe/TiO$_2$ catalysts, Ni^0 peak appears at 853.1 eV and exhibits a chemical shift of +0.4 eV compared to Ni^0 in Ni/TiO$_2$. The peak is assigned to the presence of Ni-Fe alloy in Ni-Fe/TiO$_2$ catalysts. Alternatively, addition of Fe in Ni/TiO$_2$ significantly enhanced Ni–Fe interactions. Similar Ni-Fe interactions are also affirmed by H_2-TPR analysis presented in Fig.4.1. Besides Ni^0, Ni^{2+} $2p_{3/2}$ peak in Ni$_3$Fe$_1$/TiO$_2$ is located at 856.1 eV which is +0.5 eV higher than Ni^{2+} in Ni/TiO$_2$. This shift to higher binding energy value indicate

that addition of Fe also enhanced metal-support interaction. However, moving from the profile of Ni_3Fe_1/TiO_2 to Ni_1Fe_1/TiO_2, binding energy of Ni^{2+} $2p_{3/2}$ is lowered. The results suggested weaker metal-support interaction upon further addition of Fe. Thus, optimum amount of Fe is essential to enhance bimetallic and metal-support interactions. Fig.4.4b shows peak deconvolution of Fe 2p XPS spectra of reduced $Ni-Fe/TiO_2$ catalysts. For all the Ni-Fe catalysts, three distinct Fe $2p_{3/2}$ peaks are observed due to multiple oxidation state of Fe. Peak located at 707.6 eV is assigned to Fe^0. Usually, Fe^0 peak is located at 706.8 eV in Fe-based catalysts [49]. However, Fe^0 in the present study exhibits a chemical shift of +0.8 eV. The phenomenon affirms the formation of Ni-Fe alloy in $Ni-Fe/TiO_2$. Fe^{2+} and Fe^{3+} appear at 709.6 eV and 711.2 eV respectively [52,53]. It should be noted that Fe^{2+} and Fe^{3+} peaks appear at same binding energies in all the reduced $Ni-Fe/TiO_2$ catalysts. The behavior affirms non-interacting nature of iron oxide with TiO_2 support [44] and agrees with H_2-TPR analysis. Deconvolution of Ti $2p_{3/2}$ spectra showed Ti^{3+} peak at 457.4 eV in the reduced catalysts. Existence of Ti^{3+} species suggested formation of oxygen vacancies in TiO_2 supported catalysts. Previous reports have demonstrated formation of TiO_x species by hydrogen spill-over process during reduction of Ni/TiO_2 catalysts [39]. The molar concentration of surface species in the reduced catalysts is presented in Table 4.4. It is evident that surface Ni/Fe ratio in the reduced catalyst are 1.0, 0.32 and 0.21 which is significantly lower than their bulk counterparts. While O/Ti ratio of all the reduced catalysts is lower than 2, indicating formation of oxygen vacancies during reduction.
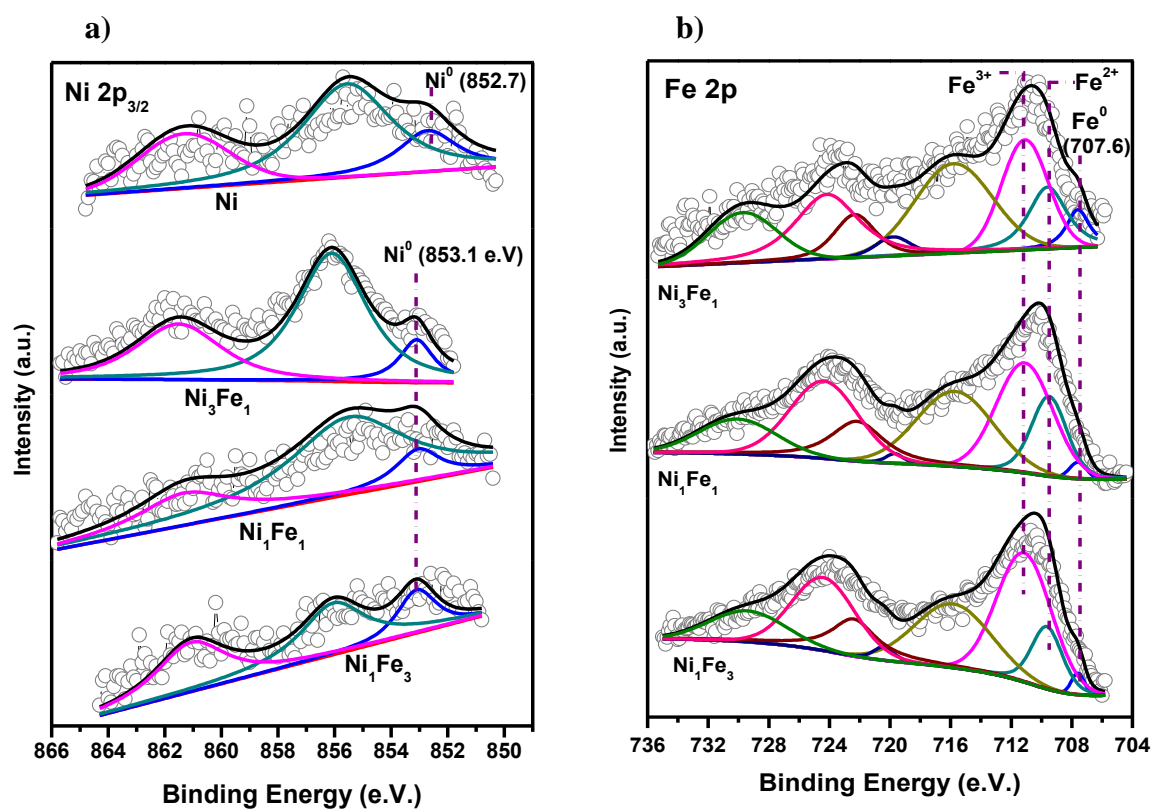
Fig. 4.4 XPS spectra of reduced catalysts synthesized by hydrotalcite route. a) Ni $2p_{3/2}$ b) Fe 2p

Table 4.4. Atomic concentration (%) of surface species in reduced catalysts synthesized by hydrotalcite route.

Catalysts	Ni^0	Ni^{2+}	Fe^0	Fe^{2+}	Fe^{3+}	Ni/Fe	O/Ti
Ni/TiO_2	0.61	2.27	-	-	-	-	1.00
Ni_3Fe_1/TiO_2	0.57	3.29	0.48	1.25	2.05	1.00	0.74
Ni_1Fe_1/TiO_2	0.32	2.21	0.21	1.76	3.55	0.46	1.07
Ni_1Fe_3/TiO_2	0.29	1.07	0.19	1.84	4.49	0.21	1.12

4.2.6 Catalytic activity in DRM and CH₄-decomposition

Dry reforming of methane was investigated at 550˚C for 6 h. Fig. 4.5 shows CH_4/CO_2 consumption and H_2/CO ratio as a function of reaction time. For Ni/TiO_2 catalysts, CH_4 consumption after 1 h TOS was 80 $\mu mol/m^2_{Ni+Fe}$ h and increased to 89 $\mu mol/m^2_{Ni+Fe}$ h after 6 h TOS. However, CO_2 consumption dropped from 78 $\mu mol/m^2_{Ni+Fe}$ h to 67 $\mu mol/m^2_{Ni+Fe}$ h within 6 h of reaction time. The H_2/CO ratio increased from 0.89 to 0.94 during the course of reaction. Carbon balance over Ni/TiO_2 dropped from 86% to 83% within TOS. The increase of CH_4 consumption, H_2/CO ratio and decrease in carbon balance with TOS suggested occurrence of CH_4 decomposition as side-reaction. Similar behavior in catalytic performance of Ni-based catalysts supported on Mg(Al)O derived from hydrotalcite-type precursors has been demonstrated [46,54,55]. Decrease in CO_2 consumption could be related to CO disproportionation reaction. Side reactions including CH_4 decomposition and CO disproportionation cause coke deposition. Coking ultimately covers Ni^0 sites in the long run DRM, thereby deactivating the catalyst. Introduction of Fe in Ni/TiO_2 catalysts showed comparatively less catalytic activity than monometallic Ni/TiO_2. The CH_4 consumption over Ni_3Fe_1/TiO_2 dropped from 82 $\mu mol/m^2_{Ni+Fe}$ h to 72 $\mu mol/m^2_{Ni+Fe}$ h from 1 h to 6 h TOS respectively. While CO_2 consumption decreased from 95 $\mu mol/m^2_{Ni+Fe}$ h to 83 $\mu mol/m^2_{Ni+Fe}$ h with TOS. Nonetheless, H_2/CO ratio was ~ 0.8 and carbon balance was ~ 92%, both of which remained almost similar during the course of reaction. Decrease in H_2/CO ratio in Ni_3Fe_1/TiO_2 compared to Ni/TiO_2 suggests introduction of Fe inhibited CH_4 dissociation. Secondly, accelerated reverse water-gas shift reaction in presence of iron oxide may lead to decrease in H_2/CO ratio [56]. Iron oxide has been demonstrated to be catalytically active for RWGS reaction [56]. Carbon balance over Ni_3Fe_1/TiO_2 catalyst remains ~ 92%, which is higher than Ni/TiO_2 catalyst. Our results suggest that introduction of Fe aided carbon removal along-with

inhibiting CH_4 dissociation during DRM. Further increase in Fe loading decreased the catalytic activity drastically. CH_4 consumption dropped from 16 $\mu mol/m^2_{Ni+Fe}$ h to 10 $\mu mol/m^2_{Ni+Fe}$ h while CO_2 consumption decreased from 21 $\mu mol/m^2_{Ni+Fe}$ h to 9 $\mu mol/m^2_{Ni+Fe}$ h with TOS over Ni_1Fe_1/TiO_2 catalyst. The drop in CH_4/CO_2 consumption with TOS is attributed to decrease in the surface concentration of Ni^0 atoms. H_2/CO ratio decreased from 0.4 to 0.26 from 1 h to 6 h TOS. However, carbon balance increased from 97% to 98%. Increase in carbon balance is related to oxidation of coke during reaction. In case of Ni_1Fe_3/TiO_2 catalyst, the CH_4/CO_2 consumption remained nearly same. Similar behavior in H_2/CO ratio and carbon balance as Ni_1Fe_1/TiO_2 was observed. Overall, ratio between Ni and Fe in the bimetallic catalysts would essentially control the extent of side reactions. An optimum ratio would exist that might favor DRM predominantly.

TPSR experiments indicated Ni is active towards CH_4 while Fe promotes CO_2 reduction. Ideally, this should enhance CO_2 conversion with increase in Fe loading. However, CO_2 conversion decreased in Ni_1Fe_1/TiO_2 and Ni_1Fe_3/TiO_2 catalysts. The explanation is as follows: Upon CO_2 exposure, Fe present in Ni-Fe catalysts is readily oxidized to FeO_x according to following equation 3. For further reaction of CO_2 with Fe, FeO_x must undergo reduction according to equation 4 or 5. However, for Ni_1Fe_1/TiO_2 and Ni_1Fe_3/TiO_2 catalysts, the amount of coke and H_2 produced from CH_4 decomposition is much lower than Ni_3Fe_1/TiO_2. Therefore, due to abundance of lattice oxygen in Fe, CO_2 could not further react with FeO_x. In Ni_3Fe_1/TiO_2, upon CO_2 exposure, Fe is readly oxidized to FeO_x. Then, H_2 and coke produced from CH_4 decomposition will react with FeO_x according to equation 4 and 5 respectively. Reaction of FeO_x by coke or H_2 will reduce FeO_x to Fe. Thus, Fe sites are again available for CO_2 activation.

$$Fe + xCO_2 \rightarrow FeO_x + xCO \qquad \ldots\ldots\ldots\ldots\ldots\ldots\ldots. \text{ (3)}$$

$$FeO_x + H_2 \rightarrow Fe + H_2O \qquad \ldots\ldots\ldots\ldots\ldots\ldots\ldots.. \text{ (4)}$$

$$FeO_x + C \rightarrow FeO_{x-1} + CO \qquad \ldots\ldots\ldots\ldots\ldots\ldots.. \text{ (5)}$$
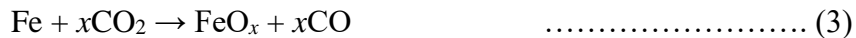
Steady-state CH_4 decomposition reaction was evaluated at 550˚C. The activity results are shown in Fig. 4.6. Ni/TiO_2 showed maximum CH_4 conversion of 47% while $Ni\text{-}Fe/TiO_2$ demonstrated lower CH_4 conversion. The behavior is in alignment with CH_4-TPSR results which implied inactivity of Fe towards CH_4. It is interesting to note that besides H_2 formation, CO formation also takes place during steady-state CH_4 decomposition. CO generation is attributed to oxidation of carbon formed during CH_4 dissociation by the lattice oxygen of FeO_x. Albeit, maximum CO formation was evidenced by Ni_1Fe_3/TiO_2 which showed minimal CH_4 conversion. Nonetheless, CO formation over monometallic Ni/TiO_2 suggested participation of lattice oxygen from TiO_2 support in coke oxidation. Thus, lattice oxygen of TiO_2 support and FeO_x would promote coke gasification during DRM.
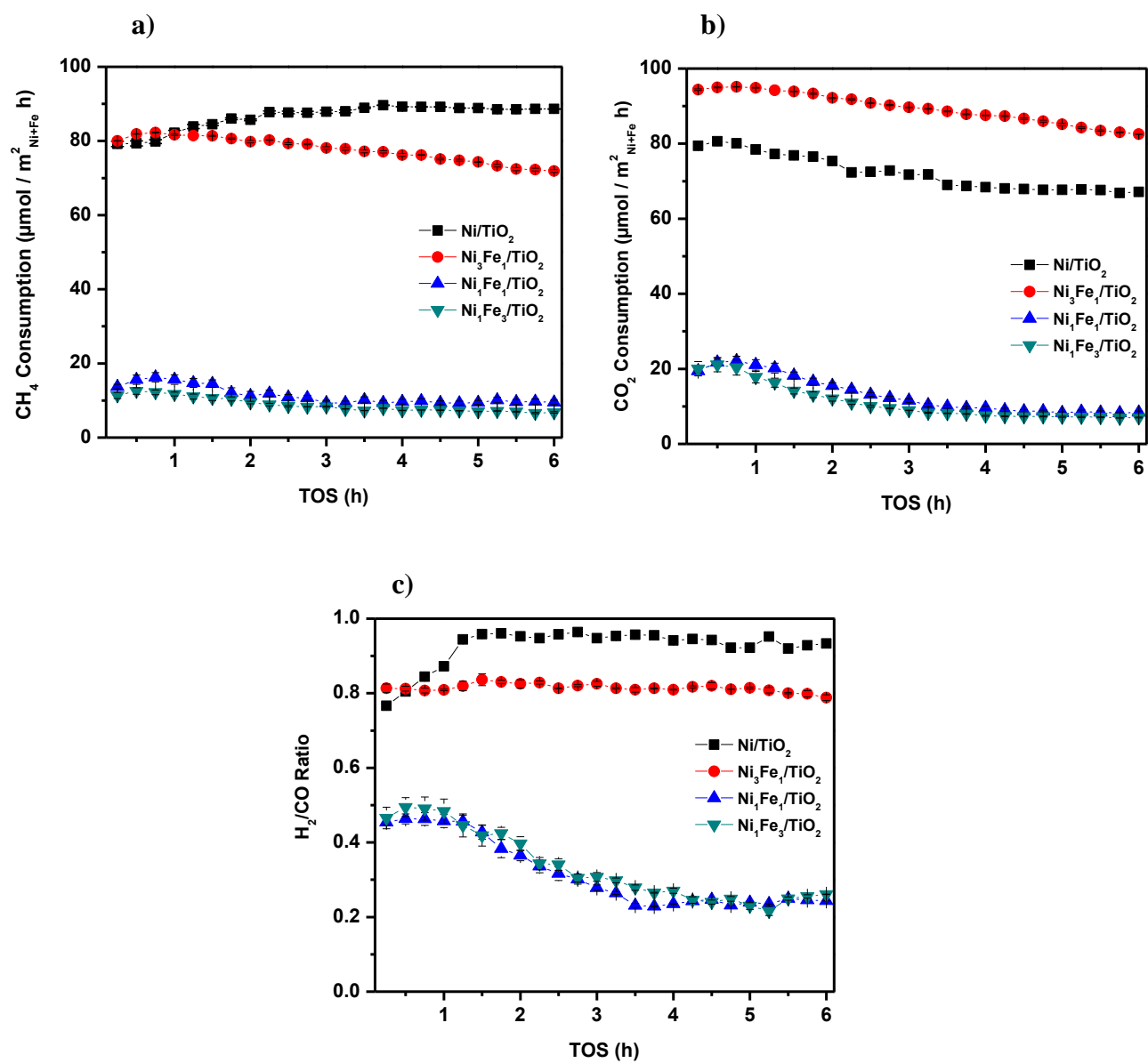
Fig. 4.5. Catalytic activity in DRM as function of reaction time over Ni/TiO_2 and Ni-Fe/TiO_2 catalysts synthesized by hydrotalcite route, a) CH_4 conversion, b) CO_2 conversion c) H_2/CO ratio.
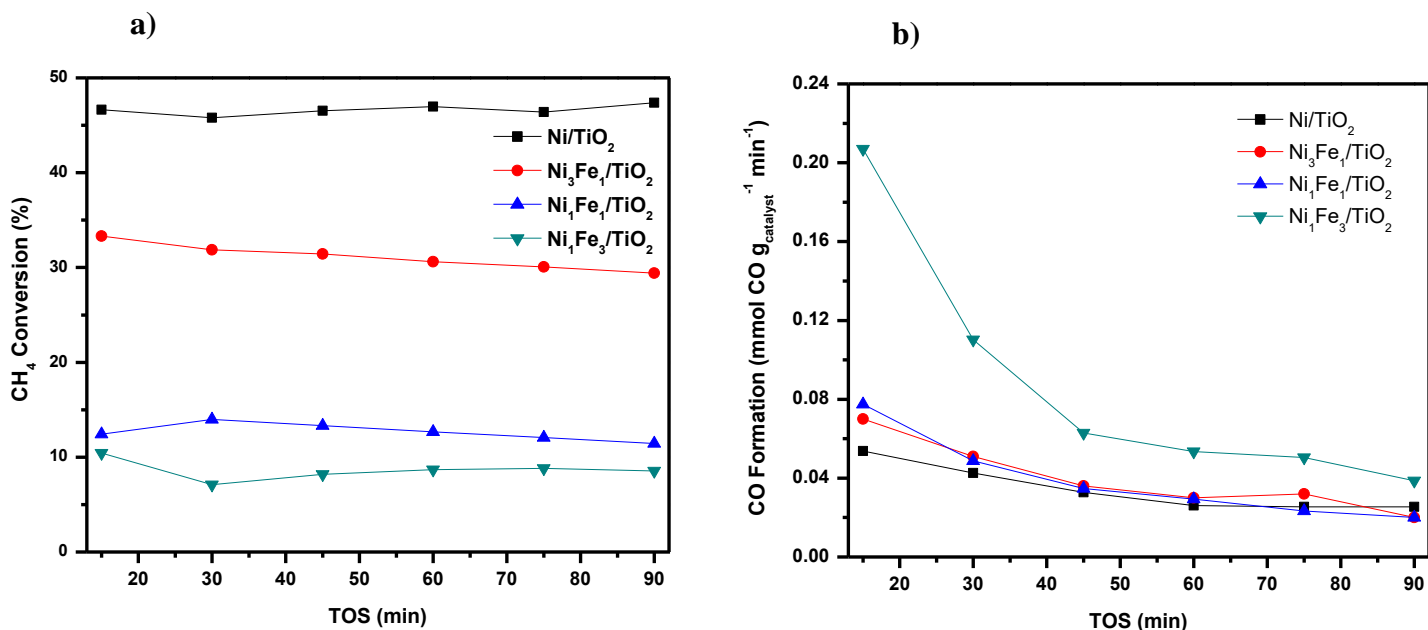
Fig. 4.6. Catalytic activity in steady-state CH_4-decompsoition over Ni/TiO_2 and Ni-Fe/TiO_2 catalysts, a) CH_4 conversion, and b) CO formation rate (mmol CO $g_{catalyst}$ min^{-1})

4.2.7 Characterization of spent catalysts

4.2.7.1 Thermogravimetric analysis-Differential thermogravimetry of spent catalysts after DRM and steady-state CH_4-decompsoition (TGA-DTG)

TGA-DTG was employed to study the amount and type of carbon deposited during dry reforming reaction. It has been shown in the literature that CH_4 decomposition is major source of carbon deposition while CO disproportionation contributes to only a minor extent [57]. Generally, dissociation of CH_4 leads to formation of two type of coke such as C_α (amorphous) and C_β (graphite) [48]. The oxidation temperature of deposited coke might be directly associated with its reactivity [24]. Therefore, C_α – which oxidizes below 600˚C [48] has been suggested to be more

112

reactive than C_β. C_α could be oxidized by oxygen derived from CO_2 dissociation or lattice oxygen from reducible supports such as TiO_2 [57]. However, if excess amount of C_α is present on catalyst surface, then it nucleates to C_β type of coke. C_β might eventually encapsulate the active nickel sites by its buildup thereby leading to catalyst deactivation [58]. Thus, a proper balance between coke formation and its gasification is essential for coke-resistance property of catalysts. Table 4.5 highlights weight loss during TGA test over Ni/TiO_2 and $Ni-Fe/TiO_2$ catalysts after DRM tests. Monometallic Ni/TiO_2 shows weight loss about 31.3 wt% which is equivalent to 51.9 mg_{coke} h^{-1} $g_{catalyst}^{-1}$. Analysis of 1st derivative of TGA curve is shown in Fig. 4.7. Asymmetric DTG curve of $Ni/TiO2$ indicated different carbon species formation. Firstly, the peak centered at 550°C is attributed to amorphous type of coke [48] and its rate of formation is evaluated to be 24.9 mg_{coke} h^{-1} $g_{catalyst}^{-1}$. Secondly, the peak centered around 615°C is assigned to graphitic type of carbon. The rate of formation of graphitic type of coke is estimated to be 27 mg_{coke} h^{-1} $g_{catalyst}^{-1}$. Interestingly, introduction of Fe significantly inhibited coke deposition. For Ni_3Fe_1/TiO_2, the amount of coke formation was 0.48 wt% equivalent to 2.5 mg_{coke} h^{-1} $g_{catalyst}^{-1}$ after 6 h DRM. It should be noted that total amount of coke deposition is suppressed by approximately 21 times with addition of 2.5 wt% Fe. The behavior suggested effectiveness of Fe in coke inhibition during DRM. Analyzing DTG curve of Ni_3Fe_1/TiO_2 shows presence of both – amorphous and graphitic carbon which indicates that presence of Fe does not alter the type of coke deposit over $Ni-Fe/TiO_2$. Further increment in the amount of Fe did not show coke formation. From previous CH_4-TPSR results, it was suggested that introduction of Fe restricted CH_4 decomposition activity. While, CO_2-TPSR/H_2-TPR experiments showed that introduction of Fe promoted formation of reactive O^* species derived from CO_2. It is envisaged that coke deposited by CH_4 decomposition is oxidized by reactive O^* species in the vicinity of active Ni^0 sites. Therefore, coke inhibition property of Ni-

113

Fe/TiO$_2$ catalysts is ascribed to dual functionality of Fe: a) Inhibit CH$_4$ decomposition b) promote formation of active O* species derived from CO$_2$. Thus, tuning the amount of Fe is essential for coke inhibition property over Ni-Fe/TiO$_2$ catalysts.

TGA-DTG test was employed to estimate the amount and type of deposited coke on Ni/TiO$_2$ and Ni-Fe/TiO$_2$ after CH$_4$ decomposition test. As shown in table 4.6, the amount of coke decreased upon introduction of Fe which agrees with CH$_4$-TPSR results, highlighting ineffectiveness of Fe towards CH$_4$ dissociation. DTG curve of spent catalysts after CH$_4$ decomposition test is shown in Fig. 4.8. The oxidation temperature of carbon is gradually lowered by 30°C suggesting easier removal of carbon upon addition of Fe. The growth of carbon filaments over Ni-based catalysts has been recognized as a three step deposition–diffusion–precipitation process [47,58]. Upon dissociation of hydrocarbon on Ni surface, hydrogen is released and carbon dissolves in Ni forming a uniform layer. With increase in rate of hydrocarbon decomposition, carbon formed diffuses through Ni particle to the support side and precipitates at metal-support interface. When rate of hydrocarbon dissociation exceeds rate of diffusion and precipitation, formation of carbon filaments begins and gradually occupies the active Ni sites [58]. Herein, it is envisaged that rate of CH$_4$ dissociation is lowered upon Fe addition. While, presence of Fe also prevented diffusion and precipitation of coke thereby lowering its oxidation temperature.
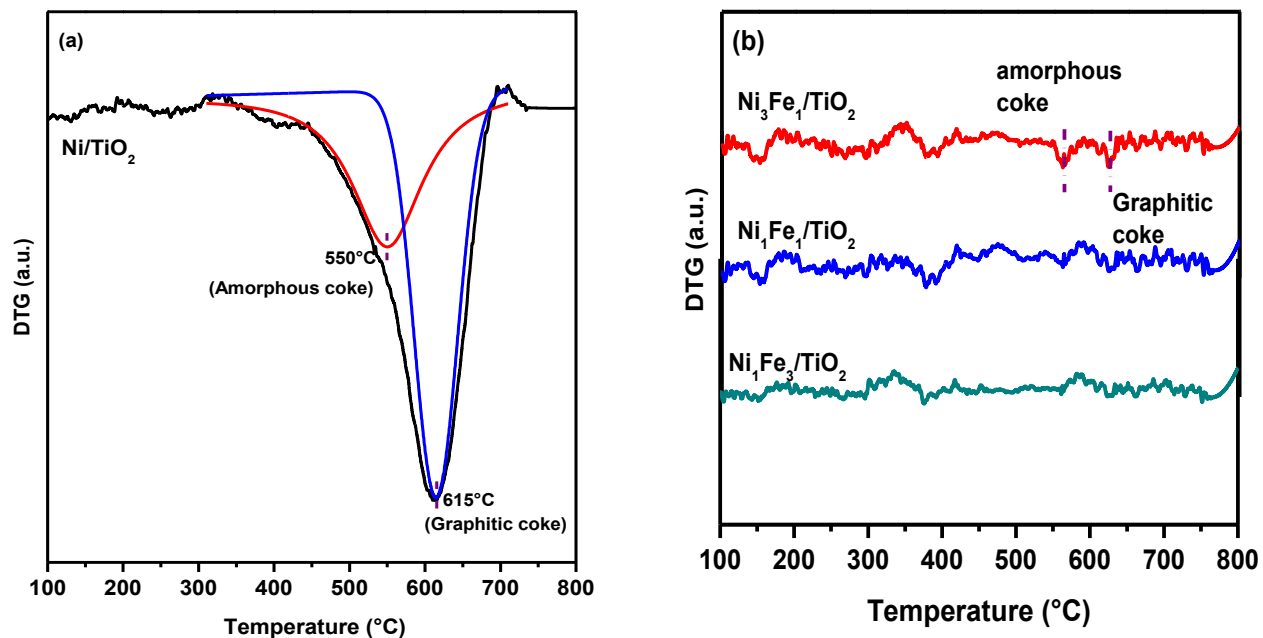
Fig. 4.7. DTG profiles of used catalysts synthesized by hydrotalcite route after DRM tests, a) Ni/TiO$_2$ and b) Ni-Fe/TiO$_2$.

Table 4.5. Analysis of TGA data of used Ni/TiO$_2$ and Ni-Fe/TiO$_2$ catalysts after DRM.

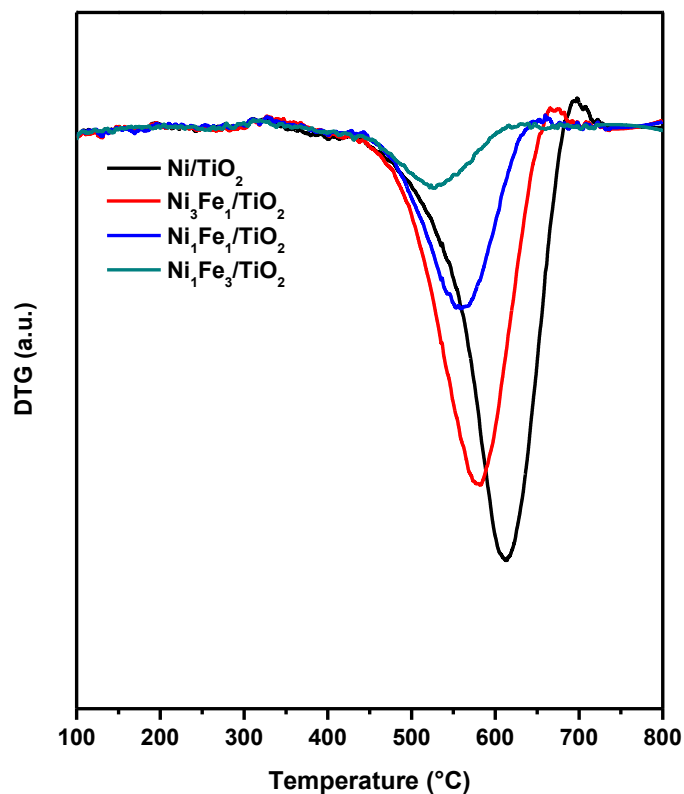| Catalyst	Amount of coke deposited (wt%)
Ni/TiO$_2$	31.3
Ni$_3$Fe$_1$/TiO$_2$	0.48

Fig. 4.8. DTG profiles of used catalysts synthesized by hydrotalcite route after steady-state CH_4-decomposition test.

Table 4.6. Analysis of TGA data of used Ni/TiO_2 and $Ni-Fe/TiO_2$ catalysts synthesized by hydrotalcite route after steady-state CH_4 decomposition tests.

Catalyst	Amount of coke deposited (wt%)
Ni/TiO_2	40
Ni_3Fe_1/TiO_2	27.2
Ni_1Fe_1/TiO_2	13.6
Ni_1Fe_3/TiO_2	5.3

4.2.7.2 X-ray Photoelectron Spectroscopy (XPS)

XPS analysis of spent catalysts was performed to estimate oxidation state and concentration of surface species. Ni $2p_{3/2}$ spectra of spent catalysts is shown in Fig. 4.9a. For Ni/TiO_2, Ni^0 peak is located at 852.7 eV. While Ni^{2+} peak is located at 856.5 eV and exhibits a chemical shift of +0.7 eV compared to its reduced counterpart. This binding energy shift is attributed to enhanced metal-support interaction during reforming reaction. Due to high oxygen mobility in reducible supports such as TiO_2, the oxygen species diffuse from the bulk towards metal-support interface to oxidize coke [59]. Next, Ni^0 peak in all $Ni-Fe/TiO_2$ spent catalyst is located at 852.7 eV. It is interesting to note that binding energy of Ni^0 in all the spent $Ni-Fe/TiO_2$ catalysts is shifted to lower value compared to their reduced counterparts. The phenomenon is related to dealloying of Ni-Fe alloy during reforming reaction. In other words, interaction between Ni and Fe were essentially lowered during the course of reaction. This dealloying of Ni-Fe alloy during DRM is consistent with previous reports [24,26]. Secondly, Ni^{2+} $2p_{3/2}$ of spent $Ni-Fe/TiO_2$ appeared at 855.5 eV which is lower than their reduced ones. The phenomenon is attributed to lowered metal-support interaction with the support during DRM. Fe 2p spectra of spent catalysts is shown in Fig. 4.9b. For all the spent $Ni-Fe/TiO_2$ catalysts, Fe^0 is located at 706.8 eV which is -0.8 eV lower than reduced catalysts. The results suggested lowered Ni-Fe interaction and thus, dealloying of Ni-Fe alloy during DRM. Fe^{2+} and Fe^{3+} appeared at 709.6 eV and 711.2 eV respectively. Further, O 1s spectra of spent catalysts were analyzed to gain insights on surface adsorbed oxygen species (SAOS). It was observed that O 1s spectra of Ni/TiO_2 and $Ni-Fe/TiO_2$ catalysts showed 3 distinct peaks upon deconvolution in Fig. 4.9c. Peak occurring at 529.7 eV was assigned to O^{2-} lattice oxygen in metal oxide [50]. It is noteworthy that lattice oxygen peak in Ni/TiO_2 was shifted by +1 eV to 530.7 eV after reforming reaction. The shift is attributed to involvement of lattice oxygen during DRM.

Specifically, oxygen from the TiO_2 support migrated from bulk to metal-support interface to oxidize carbon. Migration of lattice oxygen enhanced metal-support interaction. Peaks located at 531.5 eV and 533.1 eV are assigned to C=O (carbonates) and O–H (hydroxyl) type surface adsorbed oxygen species (SAOS) respectively [50,51]. These SAOS participated in coke removal during DRM and are further discussed in *in-situ* DRIFTS analysis. Next, C 1s XPS spectra of spent catalysts is shown in Fig. 4.9d. The major peak located at 284.8 eV originates due to the adventitious carbon or C–C graphitic type of carbon species. This peak is usually employed for calibration of XPS spectra. Peak around 288.2 eV in $Ni-Fe/TiO_2$ catalyst is attributed to CO_3^{2-} interacting with the support [51]. The C 1s spectra of used Ni/TiO_2 catalyst shows an additional peak at ~ 290.9 eV binding energy. Such feature has been attributed to graphite or graphitic type carbon species due to $\pi \rightarrow \pi^*$ transitions [60]. Contrarily, C 1s peak due to $\pi \rightarrow \pi^*$ transition was not observed in $Ni-Fe/TiO_2$ catalysts.

The molar composition of surface species after DRM tests is shown in Table 4.7. For Ni/TiO_2 catalyst, the surface concentration of Ni^0 increased from 0.7% to 0.78% during reforming. Increased Ni^0 concentration is related to evolution of bulk Ni species towards the surface during reforming which ultimately enhanced CH_4 conversion. However, O/Ti ratio decreased from 1.0 to 0.94. The decrease in O/Ti ratio is attributed to the consumption of lattice oxygen from TiO_2 support to oxidize carbon formed during DRM. For Ni_3Fe_1/TiO_2 catalyst, the surface Ni^0 concentration remained almost similar compared to its reduced one. The result indicate resistance of Ni^0 to oxidation during DRM and affirms with previous literature [24,26]. However, Fe^0 concentration decreased to 0.42% suggesting its oxidation during reaction owing to its high oxophilicity [24,26]. Accordingly, molar composition of Fe^{2+} and Fe^{3+} increased compared to the reduced Ni_3Fe_1/TiO_2 catalyst. Similarly, O/Ti ratio increased suggesting oxygen rich surface

during DRM in Ni_3Fe_1/TiO_2 catalyst. While, Ni_1Fe_1/TiO_2 and Ni_1Fe_3/TiO_2 also showed Fe^0 oxidation to Fe^{2+} and Fe^{3+} during DRM.
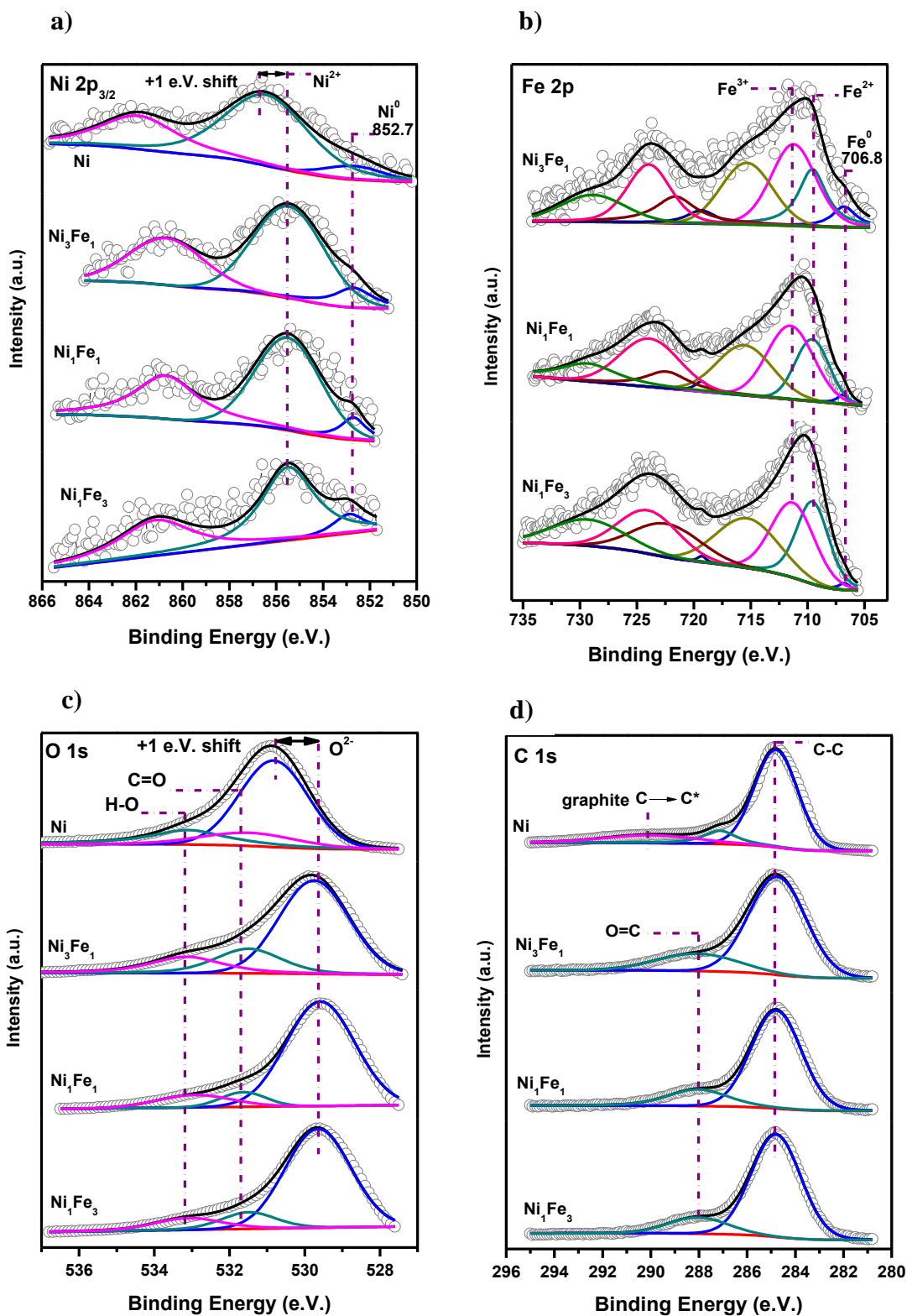
Fig. 4.9. XPS spectra of spent catalysts synthesized by hydrotalcite route. a) Ni 2p3/2 b) Fe 2p c) O 1s d) C 1s.

Table 4.7. Atomic concentration (%) of surface species in spent catalysts synthesized by hydrotalcite route.

Catalysts	Ni^0	Ni^{2+}	Fe^0	Fe^{2+}	Fe^{3+}	Ni/Fe	O/Ti
Ni/TiO_2	0.78	6.7	-	-	-	-	0.94
Ni_3Fe_1/TiO_2	0.55	3.14	0.42	1.83	3.10	0.69	0.85
Ni_1Fe_1/TiO_2	0.29	2.04	0.14	2.53	4.12	0.34	1.14
Ni_1Fe_3/TiO_2	0.24	1.57	0.12	3.18	3.65	0.25	1.21

4.2.7.3 Raman spectroscopy of used catalysts after DRM

Raman Spectroscopy of used catalysts was performed to estimate graphitic degree of coke on used catalysts. Typically, Raman spectra of used catalysts after dry reforming tests show D and G band of carbon around 1345 cm^{-1} and 1570 cm^{-1} respectively. The D-band is characteristic of amorphous carbon or hydrogen – containing carbon species (CH_x) whereas G-band refers to ordered sp^2 C = C bond in graphite [24,61]. The ratio between D-band intensity and G-band intensity (I_D/I_G) represents degree of crystallinity of deposited coke on catalyst surface. Moreover, degree of crystallinity of coke is associated with its oxidation temperature [24]. Relatively high degree of crystallinity between monometallic Ni and bimetallic Ni-Fe catalysts would suggest high temperature is required to oxidize carbon during dry reforming [24]. Fig. 4.10 shows Raman spectra of used catalysts after DRM test. Ni/TiO_2 and Ni_3Fe_1/TiO_2 catalyst demonstrated presence

of amorphous and graphitic carbon. The calculated I_D/I_G ratio was 1.00 over both Ni/TiO_2 and Ni_3Fe_1/TiO_2 catalysts. However, the intensity of D and G bands was drastically decreased in Ni_3Fe_1/TiO_2 compared to Ni/TiO_2. While Ni_1Fe_1/TiO_2 and Ni_1Fe_3/TiO_2 did not show Raman bands corresponding to deposited coke. The result indicated introduction of Fe is beneficial to inhibit coke deposition. Nevertheless, similar I_D/I_G ratio over Ni/TiO_2 and Ni_3Fe_1/TiO_2 suggested Fe does not influence degree of crystallinity of coke during DRM. In other words, introduction of Fe does not alter the type of deposited carbon over TiO_2 supported Ni-Fe catalysts. For $Ni-Fe/MgAl_2O_4$ catalysts, Fe was beneficial to decrease the crystallinity of coke [24]. While Fe was shown to change the type of coke from refractory carbon to soft-amorphous type carbon in DRM [34].
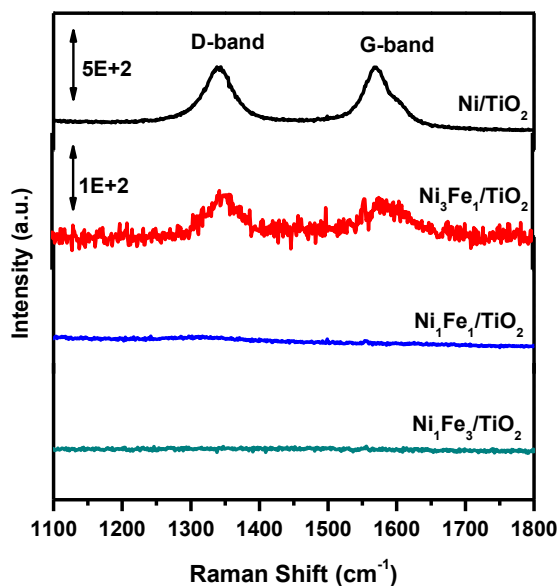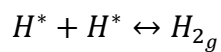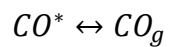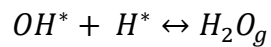

Fig. 4.10. Raman spectra of used catalysts synthesized by hydrotalcite route after DRM tests.

4.3. *In-situ* DRIFTS analysis over Ni/TiO_2 and Ni_3Fe_1/TiO_2 catalysts

In order to understand reaction mechanism and its intermediates, *in-situ* DRIFTS analysis was performed over *ex-situ* reduced Ni/TiO_2 and Ni_3Fe_1/TiO_2 catalysts. The catalysts were first

pretreated with helium at 550˚C for 1 h. A pulse of CH_4/He was then introduced into the reaction cell and transient spectra was recorded. Fig. 4.11a shows IR spectra during the first pulse of CH_4/He over Ni/TiO$_2$ catalyst. Peaks appearing at 1304 cm^{-1} and 3015 cm^{-1} are attributed to gas phase CH_4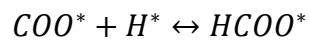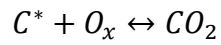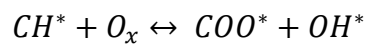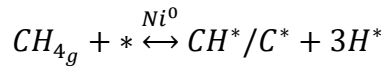 [59]. The transient spectra recorded after t =1 min and t = 2 min of 1st CH_4/He pulse show dominant peaks at 2363 cm^{-1} and 1540 cm^{-1} corresponding to gas phase CO_2 and carbonates (COO*) respectively [62]. Peak located at 3735 cm^{-1} corresponds to hydroxyl species (OH*). Since CH_4 is only present in the feed during pulse, evolution of gas phase CO_2 and carbonate species suggested that lattice oxygen of TiO$_2$ oxidized carbon produced from CH_4 decomposition. Similar observations have been made over Ni/TiO$_2$ and Ni/CeO$_2$ catalysts [39,59]. However, after t = 2 min of CH_4/He pulse, carbonate species diminished slowly and a peak at 1352 cm^{-1} gradually develops which is attributed to formate (HCOO*) species [59]. The results indicated that carbonate species react with H* from CH_4 decomposition to produce formate species.

CH$_4$/He pulse is followed by CO$_2$/He pulse and transient spectra is recorded as shown in Fig. 4.11b. Gas phase CO_2 peaks appear as doublet at 2340 cm^{-1} and 2363 cm^{-1}. While weak carbonate peaks are observed at 1540 cm^{-1} during CO$_2$/He pulse. Absence of gas phase CO peaks during CO$_2$/He pulse suggest that CO_2 does not dissociate on Ni^0 sites unlike CH_4 over Ni/TiO$_2$ catalyst. During 2nd pulse of CH_4/He shown in Fig. 4.11c, a major peak appeared at 1717 cm^{-1} which is assigned to formyl species (CHO*) [63]. Gradually from t = 1 min to t = 5 min, the population of carbonate species decreased and that of formyl species increased. It is anticipated that formyl species are derived from reaction between carbonates and H* species and decomposition of formate species. Based on the above discussion, following reaction mechanistic steps could be derived for Ni/TiO$_2$ catalyst.

$$CH_{4_g} + * \overset{Ni^0}{\longleftrightarrow} CH^*/C^* + 3H^*$$

$$CH^* + O_x \leftrightarrow COO^* + OH^*$$

$$C^* + O_x \leftrightarrow CO_2$$

$$COO^* + H^* \leftrightarrow HCOO^*$$

$$HCOO^* \leftrightarrow CHO^* + O^*$$

$$COO^* + H^* \leftrightarrow CHO^* + O^*$$

$$O^* + H^* \leftrightarrow OH^*$$

$$CHO^* \rightarrow CO^* + H^*$$

$$OH^* + H^* \leftrightarrow H_2O_g$$

$$CO^* \leftrightarrow CO_g$$

$$H^* + H^* \leftrightarrow H_{2_g}$$
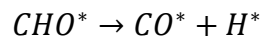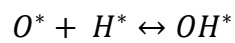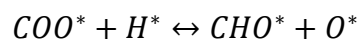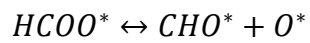
CH_4 dissociates on Ni^0 to form CH^*/C^* and H^* species. Subsequently, CH^*/C^* is oxidized by lattice oxygen of TiO_2 support to produce COO^*, OH^* and CO_2. H^* species derived from CH_4 dissociation react with COO^* to produce $HCOO^*$ or CHO^* species. Ultimately, decomposition of CHO^* will produce CO^* and H^*.
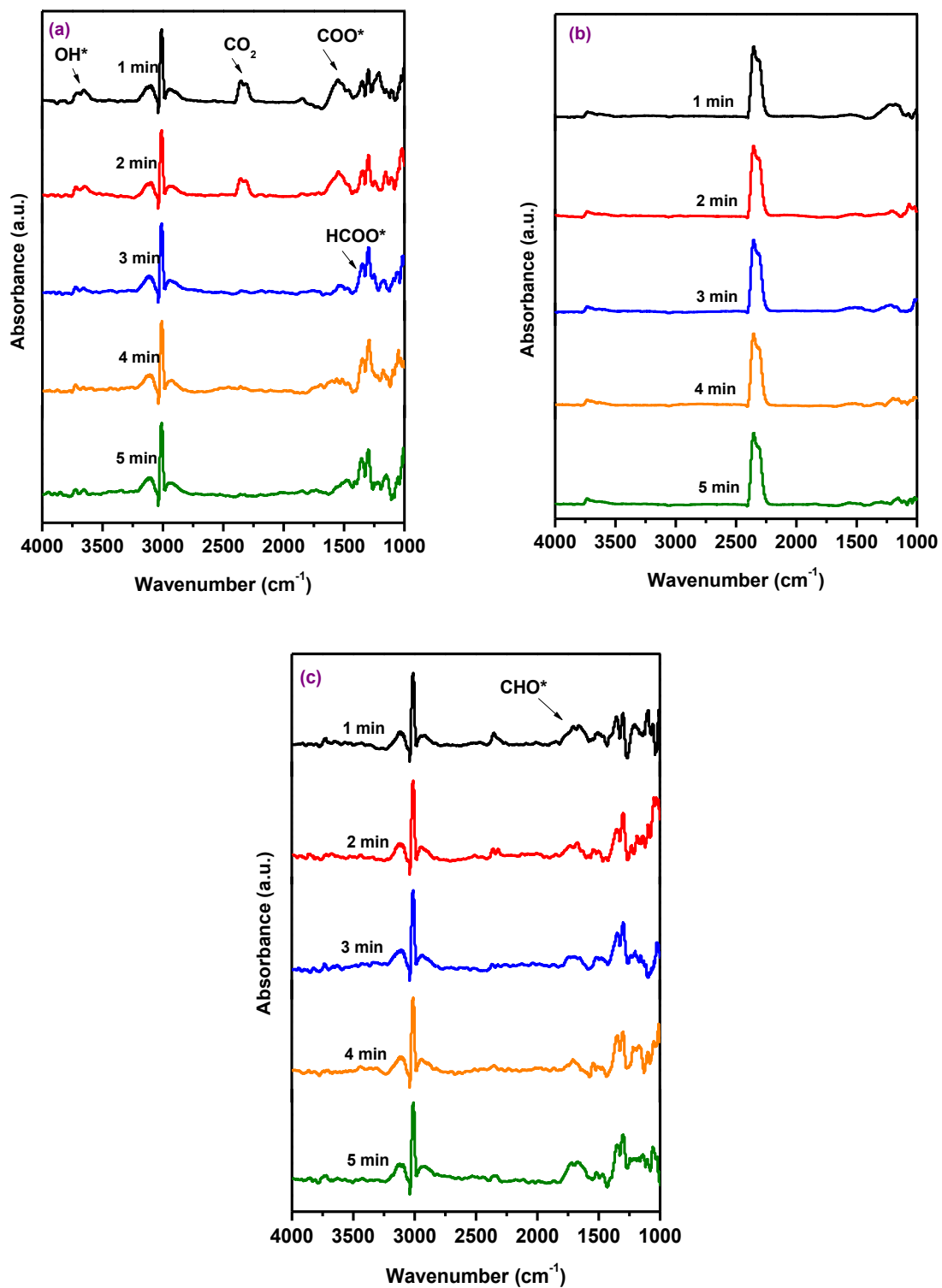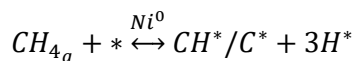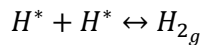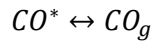
Fig. 4.11. *In-situ* DRIFTS spectra over Ni/TiO₂ catalyst synthesized by hydrotalcite route under alternate pulse at 550°C. (a) 1st CH₄/He pulse, (b) CO₂/He pulse, (c) subsequent CH₄/He pulse.

The *in-situ* DRIFTS spectra over Ni_3Fe_1/TiO_2 catalyst is shown in Fig. 4.12. During 1st pulse of CH_4/He, peaks associated with gas phase CO_2, formyl species and formate species are observed at 2363 cm^{-1}, 1717 cm^{-1} and 1352 cm^{-1} respectively after t = 1 min [59,63]. The behavior suggested that lattice oxygen from TiO_2 oxidized carbon formed by CH_4 dissociation. However, after t =2 min of CH_4/He pulse, formate species gradually decrease. On the other hand, intensity of formyl species, carbonate species and hydroxyl species (3735 cm^{-1}) gets stronger with time. Unlike Ni/TiO_2, Ni_3Fe_1/TiO_2 shows formation of formyl and carbonate species during 1st CH_4/He pulse. The results indicated that lattice oxygen from Fe also play important role along with TiO_2 support to oxidize carbonaceous species formed by CH_4 dissociation [26].

CH$_4$/He pulse is followed by CO_2/He pulse and IR spectra is recorded with time. It is observed that carbonate peaks in Ni_3Fe_1/TiO_2 during CO_2/He pulse are stronger than Ni/TiO_2 catalyst. Interestingly, weak peaks corresponding to bridged CO and multicentered CO appeared at 1910 cm^{-1} and 1800 cm^{-1} respectively [59,64]. While any such CO peaks are absent in Ni/TiO_2 catalyst. Hence it is inferred that addition of Fe facilitated CO_2 reduction [26]. Simultaneously, formation of hydroxyl species is also observed. Hydroxyl species are suggested as a result of reaction between carbonate and H* species present on catalyst surface. During 2nd CH_4/He pulse, intensity of formates and carbonates gradually decrease to produce formyl and hydroxyl species. In contrast to Ni/TiO_2, 2nd pulse of CH_4/He over Ni_3Fe_1/TiO_2 showed peaks corresponding to bridged and multicentered CO at 1910 cm^{-1} and 1800 cm^{-1} respectively. Formation of adsorb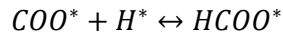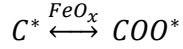ed CO during 2nd CH_4/He pulse over Ni_3Fe_1/TiO_2 is attributed to oxidation of CH^*/C^* by carbonate species. Following reaction mechanistic steps could be derived for Ni_3Fe_1/TiO_2 catalyst.

$$CH_{4_g} + * \overset{Ni^0}{\longleftrightarrow} CH^*/C^* + 3H^*$$

$$CH^* + O_x \leftrightarrow CO_2 + OH^*$$

$$CH^* \overset{FeO_x}{\longleftrightarrow} CHO^*$$

$$C^* \overset{FeO_x}{\longleftrightarrow} COO^*$$

$$COO^* + H^* \leftrightarrow HCOO^*$$

$$CO_{2_g} \overset{Fe^0}{\longleftrightarrow} COO^*$$

$$COO^* + C^*/CH^* \leftrightarrow CHO^* + CO^*$$

$$COO^* + H^* \leftrightarrow CO^* + OH^*$$

$$HCOO^* \leftrightarrow CHO^* + O^*$$

$$CHO^* \rightarrow CO^* + H^*$$

$$OH^* + H^* \leftrightarrow H_2O_g$$

$$CO^* \leftrightarrow CO_g$$

$$H^* + H^* \leftrightarrow H_{2_g}$$
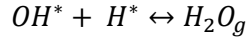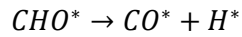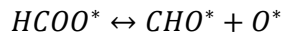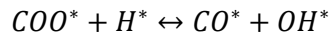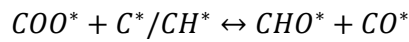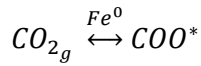
CH_4 is readily dissociated over Ni^0 to produce CH^* and H^*. Carbonaceous species including CH^* and C^* are oxidized by lattice oxygen of FeO_x and TiO_2 support to produce CHO^*/COO^* and CO_2 respectively. H^* species react with COO^* to produce $HCOO^*$ which decomposes to CHO^* and O^*. Addition of Fe will facilitate COO^* formation during CO_2 pulse. COO^* reacts with CH^*/C^* and H^* during 2nd CH_4/He pulse to produce CO^*, CHO^* and OH^* species. Thus, introduction of Fe alters the reaction mechanism in which carbonate species play important role to oxidize coke precursors to CO. Therefore, Fe is beneficial for coke removal in which lattice oxygen of both – FeO_x and TiO_2 support play important role in Ni-Fe/TiO_2 catalysts.
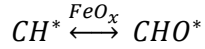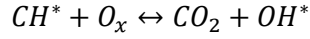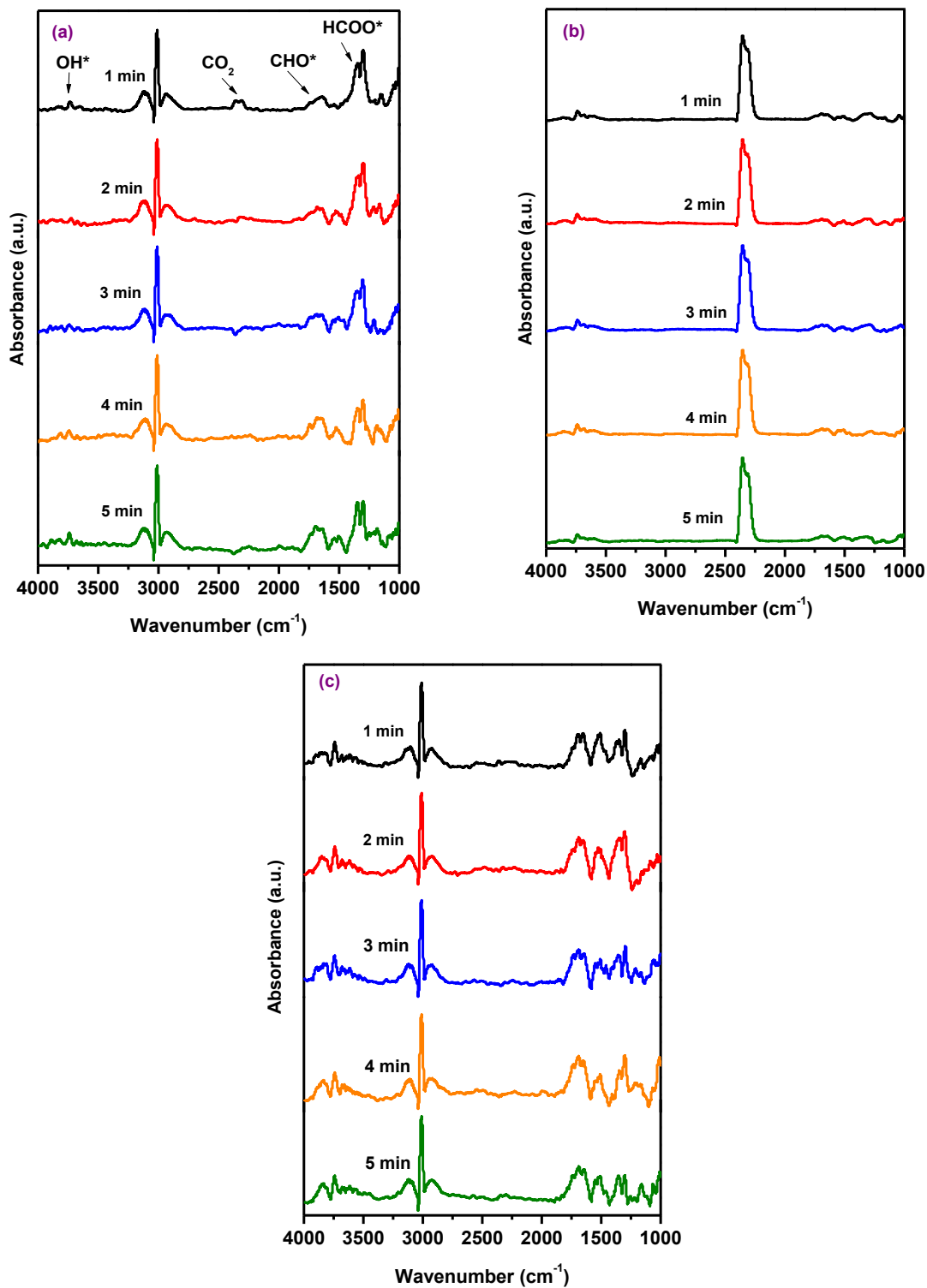
Fig. 4.12. *In-situ* DRIFTS spectra over Ni_3Fe_1/TiO_2 catalyst synthesized by hydrotalcite route under alternate pulse at 550˚C. (a) 1st CH_4/He pulse, (b) CO_2/He pulse, (c) subsequent CH_4/He pulse.

4.4 References

[1] L. A. Arkatova, N. G. Kasatsky, Y. M. Maximov, O. V. Pakhnutov, A. N. Shmakov, Catal. Today 299 (2018) 303-316.

[2] S. Sengupta, K. Ray, G. Deo, Int. J. Hydrogen Energy 39 (2014) 11462-11472.

[3] J. Kim, D. J. Suh, T. Park, K. Kim, Appl. Catal. A 197 (2000) 191-200.

[4] D. Pakhare, C. Shaw, D. Haynes, D. Shekhawat, J. Spivey, J. CO_2 Util. 1 (2013) 37–42.

[5] C. Tanios, S. Bsaibes, C. Gennequin, M. Labaki, F. Cazier, S. Billet, H. L. Tidahy, B. Nsouli, A. Aboukais, E. Abi-Aad, Int. J. Hydrogen Energy 42 (2017) 12818-12828.

[6] S. Damyanova, B. Pawelec, K. Arishtirova, M. V. M. Huerta, J. L. G. Fierro, Appl. Catal. B 89 (2009) 149-159.

[7] Z. Liu, F. Zhang, N. Rui, X. Li, L. Lin, L. E. Betancourt, D. Su, W. Xu, J. Cen, K. Attenkofer, H. Idriss, J. A. Rodriguez, S. D. Senanayake, ACS Catal. 9 (2019) 3349-3359.

[8] I. V. Yentekakis, G. Goula, M. Hatzisymeon, I. B. Argyropoulou, G. Botzolaki, K. Kousi, D. I. Kondarides, M. J. Taylor, C. M. A. Parlett, A. Osatiashtiani, G. Kyriakou, J. P. Holgado, R. M. Lambert, Appl. Catal. B 243 (2019) 490-501.

[9] L. Yue, J. Li, C. Chen, X. Fu, Y. Gong, X. Xia, J. Hou, C. Xiao, X. Chen, L. Zhao, G. Ran, H. Wang, Fuel 218 (2018) 335-341.

[10] S. C. P. Maina, A. D. Ballarini, J. I. Vilella, S. R. Miguel, Catal. Today 344 (2020) 129-142.

[11] M. C. J. Bradford, M. A. Vannice, Catal. Rev. 41 (1999) 1-42.

[12] S. Das, M. Sengupta, J. Patel, A. Bordoloi, Appl. Catal. A 545 (2017) 113-126.

[13] V. G. de la Cruz-Flores, A. Martinez-Hernandez, M. A. Gracia-Pinilla, Appl. Catal. A 594 (2020) 117455.

[14] P. Littlewood, E. Weitz, T. J. Marks, P. C. Stair, Ind. Eng. Chem. Res. 58 (2019) 2481-2491.

[15] C. Wang, N. Sun, N. Zhao, W. Wei, Y. Sun, C. Sun, H. Liu, C. E. Snape, Fuel 143 (2015) 527-535.

[16] Z. Wang, X. M. Cao, J. Zhu, P. Hu, J. Catal. 311 (2014) 469-480.

[17] H. Ay, D. Uner, Appl. Catal. B 179 (2015) 128-138.

[18] K. Jabbour, A. Saad, L. Inaty, A. Davidson, P. Massiani, N. E. Hassan, Int. J. Hydrogen Energy 44 (2019) 14889-14907.

[19] Z. Wu, B. Yang, S. Miao, W. Liu, J. Xie, S. Lee, M. J. Pellin, D. Xiao, D. Su, D. Ma, ACS Catal. 9 (2019) 2693-2700.

[20] T. V. Sagar, D. Padmakar, N. Lingaiah, P. S. S. Prasad, Catal. Lett. 149 (2019) 2597-2606.

[21] Z. Bian, S. Das, M. H. Wai, P. Hongmanorom, S. Kawi, ChemPhysChem 18 (2017) 3117–3134.

[22] Q. Zhang, T. Tang, J. Wang, M. Sun, H. Wang, H. Sun, P. Ning, Catal. Commun. 131 (2019) 105782.

[23] J. W. Han, J. S. Park, M. S. Choi, H. Lee, Appl. Catal. B 203 (2017) 625-632.

[24] S.M. Kim, P.M. Abdala, T. Margossian, D. Hosseini, L. Foppa, A. Armutlulu, W. Van Beek, A. Comas-Vives, C. Copéret, C. Müller, J. Am. Chem. Soc. 139 (2017) 1937–1949.

[25] T. Margossian, K. Larmier, S.M. Kim, F. Krumeich, C. Müller, C. Copéret, ACS Catal. 7 (2017) 6942–6948.

[26] S.A. Theofanidis, V. V. Galvita, H. Poelman, G.B. Marin, ACS Catal. 5 (2015) 3028–3039.

[27] S. A. Theofanidis, V. V. Galvita, H. Poelman, N. V. R. A. Dharanipragada, A. Longo, M. Meledina, G. V. Tendeloo, C. Detavernier, G. B. Marin, ACS Catal. 8 (2018) 5983-5995.

[28] B. Li, Y. Luo, B. Li, X. Yuan, X. Wang, Fuel Process. Technol. 193 (2019) 348-360.

[29] N. Bonmassar, M. F. Bekheet, L. Schlicker, A. Gili, A. Gurlo, A. Doran, Y. Gao, M. Heggen, J. Bernardi, B. Klötzer, Simon Penner, ACS Catal. 10 (2020) 1102-1112.

[30] M. Wang, T. Zhao, X. Dong, M. Li, H. Wang, Appl. Catal. B 224 (2018) 214-221.

[31] S. M. Lima, J. M. Assaf, Catal. Lett. 108 (2006) 63-70.

[32] X. Song, X. Dong, S. Yin, M. Wang, M. Li, H. Wang, Appl. Catal. A 526 (2016) 132-138.

[33] A. Tsoukalou, Q. Imtiaz, S. M. Kim, P. M. Abdala, S. Yoon, C. R. Müller, J. Catal. 343 (2016) 208–214.

[34] T. Zhang, Z. Liu, Y. Zhu, Z. Liu, Z. Sui, K. Zhu, X. Zhou, Appl. Catal. B 264 (2020) 118497.

[35] M.K. Nikoo, N. A. S. Amin, Fuel Process. Technol. 92 (2011) 678-691.

[36] J. Feng, Y. He, Y. Liu, Y. Du, D. Li, Chem. Soc. Rev. 44 (2015) 5291-5319.

[37] P. Li, F. Yu, N. Altaf, M. Zhu, J. Li, B. Dai, Materials 11 (2018) 221.

[38] K. Tomishige, D. Li, M. Tamura, Y. Nakagawa, Catal. Sci. Technol. 7 (2017) 3952-3979.

[39] Q.G. Yan, W.Z. Weng, H.L. Wan, H. Toghiani, R.K. Toghiani, C.U. Pittman, Appl. Catal. A 239 (2003) 43–58.

[40] A. Peters, F. Nouroozi, D. Richter, M. Lutecki, Roger Glaser, ChemCatChem 3 (2011) 598-606.

[41] S. Li, M. Li, C. Zhang, S. Wang, X. Ma, J. Gong, Int. J. Hydrogen Energy 37 (2012) 2940-2949.

[42] K. Ray, S. Sengupta, G. Deo, Fuel Process. Technol. 156 (2017) 195–203.

[43] J. Ashok, S. Kawi, Appl. Catal. A 490 (2015) 24–35.

[44] X. Gao, J Shen, Y. Hsia, Y. Chen, J. Chem. Soc. Faraday Trans. 89 (1993) 1079-1084.

[45] D. Pandey, G. Deo, J. Ind. Eng. Chem. 33 (2016) 99–107.

[46] K. Song, M. Lu, S. Xu, C. Chen, Y. Zhan, D. Li, C. Au, L. Jiang, K. Tomishige, Appl. Catal. B 239 (2018) 324 – 333.

[47] D. Li, S. Xu, K. Song, C. Chen, Y. Zhan, L. Jiang, Appl. Catal. A 552 (2018) 21–29.

[48] M. Shah, S. Das, A.K. Nayak, P. Mondal, A. Bordoloi, Appl. Catal. A 556 (2018) 137–154.

[49] J. Ashok, S. Kawi, ACS Catal. 4 (2014) 289-301.

[50] M. Zhang, J. Zhang, Z. Zhou, S. Chen, T. Zhang, F. Song, Q. Zhang, N. Tsubaki, Y. Tan, Y. Han, Appl. Catal. B 264 (2020) 118522.

[51] S. Damyanova, I. Shtereva, B. Pawelec, L. Mihaylov, J.L.G. Fierro, Appl. Catal. B 278 (2020) 119335.

[52] T. Yamashita, P. Hayes, Appl. Surf. Sci. 254 (2008) 2441–2449.

[53] M. Muhler, R. Schlögl, G. Ertl, J. Catal. 138 (1992) 413–444.

[54] R. Dębek, M. Motak, D. Duraczyska, F. Launay, M.E. Galvez, T. Grzybek, P. Da Costa, Catal. Sci. Technol. 6 (2016) 6705–6715.

[55] R. Dębek, M. Motak, M.E. Galvez, T. Grzybek, P. Da Costa, Appl. Catal. B 223 (2018) 36–46.

[56] S. Sengupta, A. Jha, P. Shende, R. Maskara, A.K. Das, J. Environ. Chem. Eng. 7 (2019) 102911.

[57] C. M. Damaskinos, M. A. Vasiliades, A. M. Efsthathiou, Appl. Catal. A 579 (2019) 116-129.

[58] A. M. Amin, E. Croiset, W. Epling, Int. J. Hydrogen Energy 36 (2011) 2904-2935.

[59] S. Das, J. Ashok, Z. Bian, N. Dewangan, M.H. Wai, Y. Du, A. Borgna, K. Hidajat, S. Kawi, Appl. Catal. B 230 (2018) 220-236.

[60] S.A. Theofanidis, R. Batchu, V.V. Galvita, H. Poelman, G.B. Marin, Appl. Catal. B 185 (2016) 42-55.

[61] K. Cao, M. Gong, J. Yang, J. Cai, S. Chu, Z. Chen, B. Shan, R. Chen, J. Catal. 373 (2019) 351–360.

[62] A.L.A. Marinho, F.S. Toniolo, F.B. Noronha, F. Epron, D. Duprez, N. Bion, Appl. Catal. B 281 (2021) 119459.

[63] K. Bu, J. Deng, X. Zhang, S. Kuboon, T. Yan, H. Li, L. Shi, D. Zhang, Appl. Catal. B 267 (2020) 118692.

[64] Y. Wang, L. Yao, Y. Wang, S. Wang, Q. Zhao, D. Mao, C. Hu, ACS Catal. 8 (2018) 6495-6506.

Chapter 5

Coke resistant Ni-Fe catalyst over reducible TiO₂-CeO₂ support for low temperature dry reforming of methane

5.1 Introduction

Dry reforming of methane (DRM) $CH_4 + CO_2 \rightarrow 2CO + 2H_2$, offers conversion of two anthropogenic green-house gases in a single reaction [1,2]. Syngas produced with nearly equimolar mixtures of CO and H_2 is a versatile feedstock for F-T synthesis [3,4]. Precious metal catalysts including Pt, Rh, Ru and Pd are widely investigated for DRM [5]. However, owing to high cost and low availability, precious metals are undesirable from economic point of view. Alternatively, inexpensive Ni based catalysts show comparable activity to precious metals [6]. Nonetheless, Ni catalysts are deactivated during DRM due to coke formation which is caused by side reactions such as methane decomposition, $CH_4 \rightarrow C + 2H_2$, and CO disproportionation, $2CO \rightarrow C + CO_2$. [5,6] To mitigate coke formation during DRM, various strategies have been studied in the literature. These include – addition of a promoter metal such as Co, Fe or Cu [7]. Among aforementioned promoter metals, Fe is chosen due to its low cost and wide availability. Bimetallic Ni-Fe catalysts have been demonstrated to reduce coke formation owing to the redox properties of Fe [8-11]. Fe^0 was shown to oxidize to FeO_x during DRM under CO_2 exposure [8,9]. While coke formed during reforming was gasified to CO by FeO_x.

Besides promoting Ni with Fe, choice of support could also play vital role in coke removal during DRM. Recently, it was shown that reducible supports including CeO_2, TiO_2 and mixed oxide TiO_2-CeO_2 could be beneficial to oxidize coke precursors [12-14]. Ni/TiO_2 showed stable

activity performance and coke resistance in DRM. TiO_x species formed during reduction at 700°C facilitated decoration of large Ni^0 ensembles. The phenomenon was attributed to reduction in surface free energy thereby inducing strong metal-support interaction (SMSI) effect [12]. Similarly, SMSI effect altered metal electronic properties via charge transfer between metal and support in Ni/CeO_2. When reduced above 600°C, Ni^0 atoms were partially encapsulated by CeO_{2-x} species and thereby enhanced coke gasification at metal-support interface [13]. A mixture of TiO_2-CeO_2 as support for Ni catalysts were recently investigated in DRM [15,16]. It was shown that active and labile oxygen from the mixed oxide support oxidized coke to CO and significantly increased coke resistance. Secondly, oxygen vacancies created during reduction also served as active site for CO_2 activation [16]. Thus, reducible mixed oxide support TiO_2-CeO_2 could be one potential support for Ni catalysts in DRM.

Based on our previous results, it is demonstrated that Ni_3Fe_1/TiO_2 catalyst synthesized by hydrotalcite precursors showed optimum activity performance. However, complete elimination of coke was not achieved. This study is motivated to obtain enhanced coke resistance in Ni-Fe catalysts for low temperature DRM. Thus, reducible TiO_2-CeO_2 support is employed to enhance the coke resistance of Ni-Fe catalyst.

5.2 Results and Discussion

5.2.1 Catalytic Activity performance in DRM and CH_4 decomposition

Catalytic activity results over Ni_3Fe_1/TiO_2-CeO_2 are shown in Fig. 5.1. We compare activity results of Ni_3Fe_1/TiO_2-CeO_2 with Ni_3Fe_1/TiO_2 catalyst as discussed in chapter 4. Introduction of 20 wt% CeO_2 in the support dropped catalytic activity in DRM. The CH_4 consumption decreased to 25 $\mu mol/m^2_{Ni+Fe}$ h while CO_2 consumption declined to 35 $\mu mol/m^2_{Ni+Fe}$ h after 6 h TOS when

compared with Ni_3Fe_1/TiO_2 catalyst. It is well known that catalytic activity in DRM is controlled by presence of Ni^0 species. So, decrease in CH_4 and CO_2 conversion is attributed to the loss of active Ni^0 sites during reforming and is explained as follows: Strong metal support interaction (SMSI) effect upon reduction of $Ni-CeO_2$ based catalysts is well documented in the literature [13,17]. SMSI effect would ultimately encapsulate active Ni^0 sites [13]. Secondly, SMSI effect would lead high oxygen mobility in the presence of redox CeO_2 support [18]. Specifically, the oxygen from the bulk CeO_2 is readily diffused towards metal-support interface to oxidize coke formed during DRM [18]. In the meantime, strong interaction of Ni species with CeO_2 support could possibly form Ni-O-Ce solid solution thereby attenuating the active Ni^0 sites. Formation of Ni-O-Ce solid solution in the spent catalysts is further evidenced by Raman spectroscopy discussed below. However, SMSI effect and oxygen mobility also imparts high coke resistance to the catalyst. The H_2/CO ratio achieved over CeO_2 modified catalyst also dropped compared to Ni_3Fe_1/TiO_2. H_2/CO ratio dropped to 0.55 from 0.81 in Ni_3Fe_1/TiO_2-CeO_2 and Ni_3Fe_1/TiO_2 respectively. The decrease in H_2/CO ratio is attributed to presence of CeO_2 which is suggested to be active catalyst support for RWGS reaction over Ni catalysts [18]. During reduction, surface capping oxygen associated with CeO_2 is easily transformed to Ce^{3+} [19]. This process generates oxygen vacancies which further acts as active sites for CO_2 activation [19,20]. Thus, presence of CeO_2 would accelerate RWGS as side reaction thereby decreasing H_2/CO ratio. Catalytic activity in CH_4 decomposition is presented in Fig. 5.2a. CH_4 decomposition commenced after 15 min of TOS, while dropping during the course of reaction. The induction period observed here is also reported over some Ni-based catalysts with low basicity in the literature [20]. However, drop in CH_4 conversion after 15 min is attributed to loss of Ni^0 sites. The behavior is suggested to the formation of Ni-O-Ce solid solution and follows above mentioned explanation. It should be noted

that Ni_3Fe_1/TiO_2-CeO_2 showed CO formation during CH_4 decomposition. The results suggested oxidation of coke by lattice oxygen from reducible support and FeO_x species.
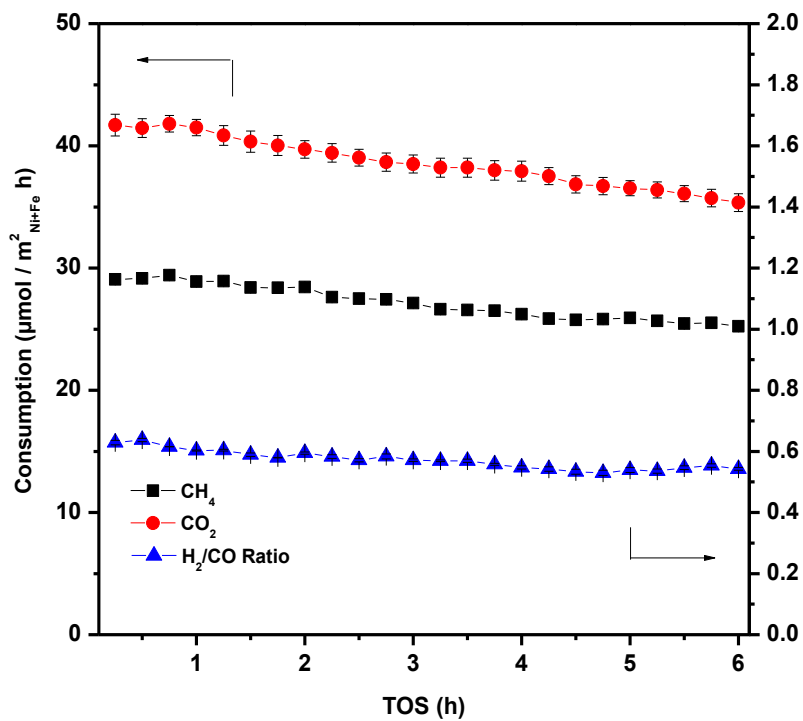

Fig. 5.1. CH_4, CO_2 consumption (%) and H_2/CO ratio as function of reaction time over Ni_3Fe_1/TiO_2-CeO_2 catalyst in DRM.
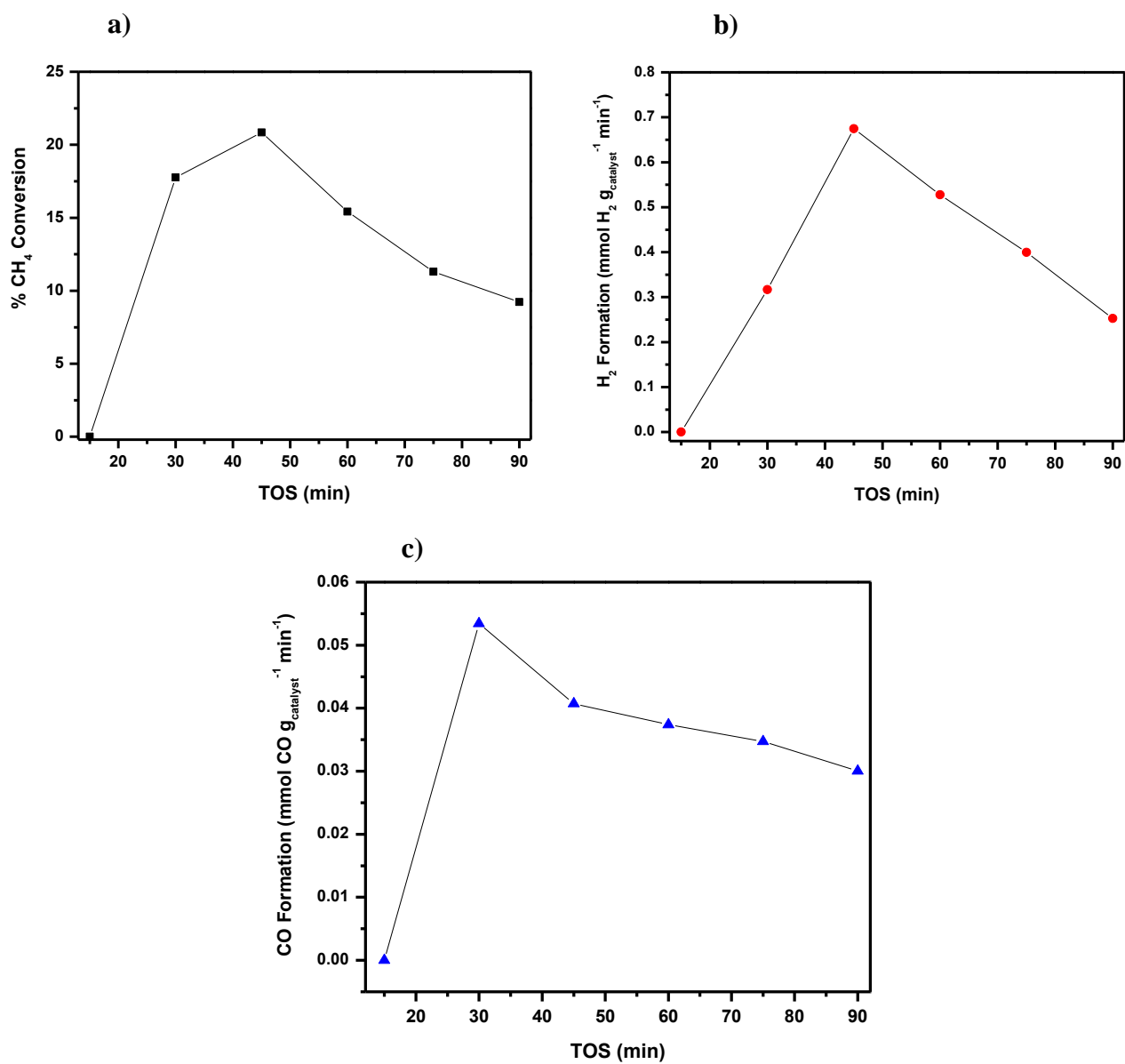
Fig. 5.2. Catalytic activity over Ni_3Fe_1/TiO_2-CeO_2 catalyst in CH_4 Decomposition. a) % CH_4 conversion b) H_2 formation (mmol min^{-1} $g_{catalyst}^{-1}$) c) CO formation (mmol min^{-1} $g_{catalyst}^{-1}$).

5.2.2 Hydrogen–temperature programmed reduction (H₂-TPR)

Hydrogen–temperature programmed reduction (H$_2$-TPR) was employed to study the reducibility of mixed oxide TiO$_2$-CeO$_2$ support, Ni$_3$Fe$_1$/TiO$_2$-CeO$_2$ catalyst and metal-support interaction. Fig. 5.3 shows H$_2$-TPR profile of TiO$_2$-CeO$_2$ support and Ni$_3$Fe$_1$/TiO$_2$-CeO$_2$ catalyst. The TPR profile of TiO$_2$-CeO$_2$ support showed three peaks located at 120°C, 287°C and 490°C. Peaks located at 120°C and 287°C are attributed to the reduction of surface oxygen species adsorbed on oxygen vacancies of mixed oxide support [21]. It is reported that ionic radius of Ti^{4+} ions (0.065 nm) is smaller than Ce^{4+} (0.097 nm) ions. Thus, introduction of CeO$_2$ in TiO$_2$ would cause changes in lattice parameter of TiO$_2$, thereby forming oxygen vacancies [22]. Adsorption of oxygen species on those vacancies would lead its reduction at 120°C and 287°C [21]. Secondly, the peak observed at 490°C is attributed to the reduction of easily reducible surface capping oxygen in CeO$_2$, which is followed by the formation of Ce^{3+} ions [19,23]. Considering H$_2$-TPR profile of bimetallic Ni$_3$Fe$_1$/TiO$_2$-CeO$_2$ catalyst, three reduction peaks are observed. Peak located at 217°C is attributed to the reduction of bulk or non-interacting NiO species. While peak located at 270°C is assigned to the reduction of strongly interacting NiO-TiO$_2$ species with the support. As such, only 3 peaks are observed for the reduction of Ni$_3$Fe$_1$/TiO$_2$-CeO$_2$ catalyst, it is envisaged that reduction of Fe$_2$O$_3$ would also have occurred simultaneously with the reduction of NiO. This behavior suggested that Fe$_2$O$_3 \rightarrow$ Fe$_3$O$_4 \rightarrow$ FeO step reduction also occurred simultaneously with NiO-TiO$_2$ at 270°C. In other words, peak located around 270°C also suggested bimetallic Ni – Fe interaction. The peak at 330°C is assigned to reduction of FeO $\rightarrow$ Fe^0. It should be noted that reduction temperatures of peak 2 and 3 in Ni$_3$Fe$_1$/TiO$_2$-CeO$_2$ were shifted to higher values compared to Ni$_3$Fe$_1$/TiO$_2$ in chapter 4. The phenomenon is explained by strong metal-support interaction (SMSI) effect upon addition of CeO$_2$. Meanwhile, addition of CeO$_2$ also enhanced

overall H_2 consumption to 1.95 mmolH$_2$/g$_{catalyst}$ in comparison to 1.83 mmolH$_2$/g$_{catalyst}$ observed over Ni$_3$Fe$_1$/TiO$_2$. Such findings suggested introduction of CeO$_2$ also promoted reducibility of Ni-Fe catalyst besides inducing SMSI effect.
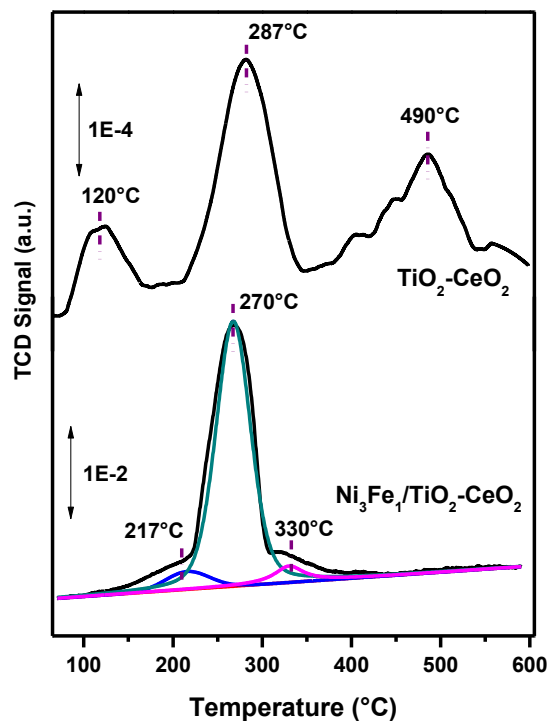
Fig. 5.3. H$_2$-TPR profile of TiO$_2$-CeO$_2$ support and Ni$_3$Fe$_1$/TiO$_2$-CeO$_2$ catalyst.

5.2.3 CO-Chemisorption

CO chemisorption was performed to estimate number of metallic sites over reduced catalyst. Typically, CO uptake values are correlated with number of metallic sites on catalyst surface with the assumption that each CO molecule chemisorbs one metallic site. CO-chemisorption analysis showed 16 μmol/g$_{catalyst}$ of CO adsorbed on Ni$_3$Fe$_1$/TiO$_2$-CeO$_2$ which is approximately 2 times higher than Ni$_3$Fe$_1$/TiO$_2$. The results suggested addition of CeO$_2$ in TiO$_2$ support would promote

formation of metallic Ni^0 on surface which is attributed to enhanced reducibility as evidenced by H_2-TPR analysis.

Table 5.1. Comparison of amount of CO adsorbed on reduced Ni_3Fe_1/TiO_2-CeO_2 and Ni_3Fe_1/TiO_2 catalyst

Catalyst	CO Adsorbed ($\mu mol/g_{catalyst}$)
Ni_3Fe_1/TiO_2-CeO_2	16.0
Ni_3Fe_1/TiO_2	9.0

5.2.4 Methane – Temperature programmed surface reaction/Differential thermogravimetry (CH$_4$-TPSR/DTG)

Transient activity of CH_4 over CeO_2 modified Ni-Fe catalyst was studied by methane – temperature programmed surface reaction (CH$_4$-TPSR). Fig. 5.4a shows CH$_4$-TPSR profile over reduced Ni_3Fe_1/TiO_2-CeO_2 catalyst. It is observed that transient activity of CH_4 begins nearly around 350°C and reaches maximum at 495°C. Comparing with Ni_3Fe_1/TiO_2 catalyst, addition of CeO_2 did not influenced surface reaction of CH_4. The behavior is suggested to similar bimetallic Ni-Fe interactions observed over TiO_2 and TiO_2-CeO_2 supported catalysts by H_2-TPR analysis. In other words, surface reaction of CH_4 with Ni-Fe/TiO_2-CeO_2 catalyst is independent of support modification. CH$_4$-TPSR profile of Ni/MgAlO catalyst showed peak temperature of 534°C [24]. The differences in peak temperature in CH$_4$-TPSR profile between our results and those reported in literature could be explained by different metal-support interactions. The type of carbon species formed during surface reaction were investigated by differential thermogravimetry (DTG). Fig.

5.4b shows a dominant peak at 530˚C attributed to oxidation of amorphous or CH_x type of carbon [25]. Comparing DTG curve of CeO_2 modified Ni-Fe catalyst with Ni_3Fe_1/TiO_2, it is inferred that introduction of CeO_2 would not influence the type of carbon species formed during CH_4 dissociation.
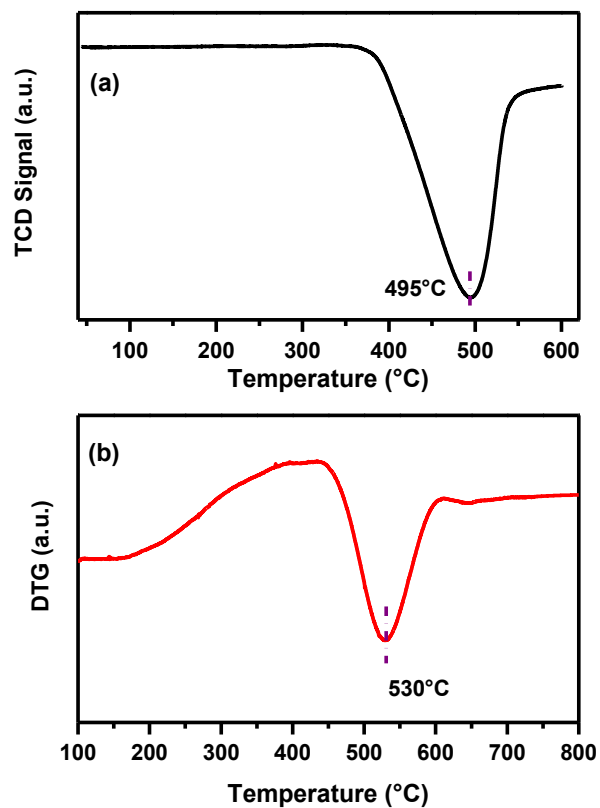
Fig. 5.4. CH_4-TPSR/DTG over reduced Ni_3Fe_1/TiO_2-CeO_2 catalyst, (a) CH_4-TPSR (b) DTG of used catalyst after CH_4-TPSR.

5.2.5 Carbon dioxide – Temperature programmed surface reaction/Hydrogen – Temperature programmed reduction (CO_2-TPSR/H_2-TPR)

Influence of CeO_2 addition to Ni_3Fe_1/TiO_2 catalyst on CO_2 transient activity was further studied by CO_2-TPSR experiment. CO_2-TPSR/H_2-TPR over reduced catalysts could be described according to following equations.

$$CO_2 \rightarrow CO^* + O^* \qquad (1)$$

$$O^* + H_2 \rightarrow H_2O \qquad (2)$$
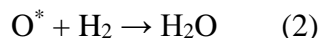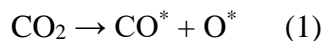
Dissociation of CO_2 on active metal or interface between active-metal and support forms CO^* and surface adsorbed oxygen species O^*. Formed O^* species are then characterized by H_2-TPR. The H_2 consumed in the TPR is directly correlated to O^* species formed during CO_2 dissociation according to equation 1 and 2. Thus, H_2-TPR profile after performing CO_2-TPSR test is shown in Fig.5. Peaks observed below 600˚C are assigned to active Ni^0 centers while peak located at 618˚C is attributed to active Fe^0 centers in Ni-Fe catalyst [26]. However, this peak located at 618˚C was not observed over Ni_3Fe_1/TiO_2 catalyst. The results suggested incorporation of CeO_2 would influence population of surface metallic species which would ultimately affect the catalytic activity. The H_2 consumption during H_2-TPR after CO_2-TPSR over CeO_2 modified Ni-Fe catalyst was calculated to be 1.44 $mmolH_2/g_{catalyst}$ which is slightly lower than Ni_3Fe_1/TiO_2. Such findings could be related to increased concentration of surface Ni^0 species in Ni_3Fe_1/TiO_2-CeO_2 as shown by CO-chemisorption and XPS analysis. Surface Ni^0 species have been shown to resist CO_2 dissociation [24].

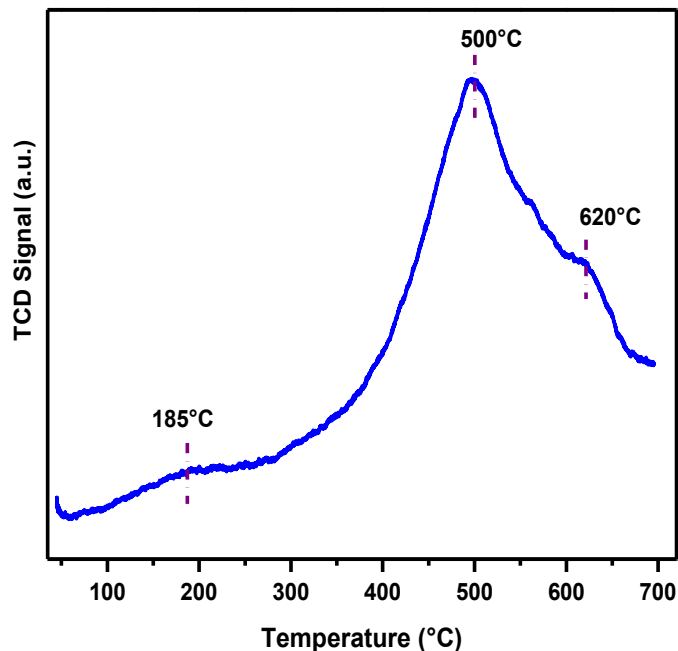Fig. 5.5. H$_2$-TPR profile over Ni$_3$Fe$_1$/TiO$_2$-CeO$_2$ catalyst after CO$_2$-TPSR test.

5.2.6 X-ray photoelectron spectroscopy (XPS)

XPS analysis was conducted to get insights on metal oxidation state and surface concentration. For CeO$_2$ modified Ni$_3$Fe$_1$/TiO$_2$-CeO$_2$ catalyst, Ni 2p$_{3/2}$ spectrum presented in Fig. 5.6a showed peaks corresponding to Ni^0 and Ni^{2+} after reduction. The presence of Ni^{2+} suggested incomplete reduction which is related to SMSI effect between Ni and TiO$_2$-CeO$_2$ support. Generally, metallic Ni species show B.E. of 852.7 eV [18]. It is interesting to note that deconvolution of Ni 2p$_{3/2}$ spectra showed two peaks corresponding to Ni^0, indicating differences in electron densities on metallic Ni species after reduction. Ni^0 peak with B.E. of 851.9 eV labelled as Ni^0 (I) is attributed to Ni species rich in electron density. Similar observations for Ni^0 are shown in the literature for Ce modified Ni catalysts [19]. Secondly, a peak observed at 853.1 eV exhibiting a chemical shift of +0.4 eV compared to standard Ni^0 B.E. suggested electron deficient Ni^0 on surface. In other words, those Ni species interacted with Fe to form Ni-Fe alloy. Similar observations on Ni-Fe

alloy formation over Ni_3Fe_1/TiO_2 are presented in chapter 4. Ni^0 at 853.1 eV are labelled as Ni^0 (II). The B.E. of Ni^{2+} was observed at 855.1 eV, exhibiting a chemical shift of +1.1 eV compared to bulk or non-interacting NiO [27,28]. Such a chemical shift suggested interaction of Ni^{2+} with the support. Ni^{2+} B.E. values are in alignment with previous results of Ni $2p_{3/2}$ spectra of reduced Ni_3Fe_1/TiO_2 catalyst. Considering Fe 2p spectra in Fig. 5.7a, three distinct Fe $2p_{3/2}$ peaks are observed due to multiple oxidation state of Fe after reduction at 550˚C. Peak located at 707.5 eV is attributed to Fe^0 which exhibits a chemical shift of +0.7 eV compared to monometallic Fe-based catalysts [26]. This observation again affirms formation of Ni-Fe alloy. Next, Fe^{2+} and Fe^{3+} are observed at 709.6 eV and 711.2 eV respectively [26]. Ce 3d spectra were deconvoluted into ten peaks due to Ce $3d_{5/2}$ and Ce $3d_{3/2}$ orbital split shown in Fig. 5.8. Ce $3d_{5/2}$ and Ce $3d_{3/2}$ peaks are labelled as V and U respectively. For Ce $3d_{5/2}$, peak located at 880.5 eV is attributed to Ce^{3+} while peak corresponding to 882.4 eV is assigned to Ce^{4+} [18,19]. Presence of Ce^{3+} in CeO_2 supported catalysts is associated with formation of oxygen vacancies as discussed in section 2.2.
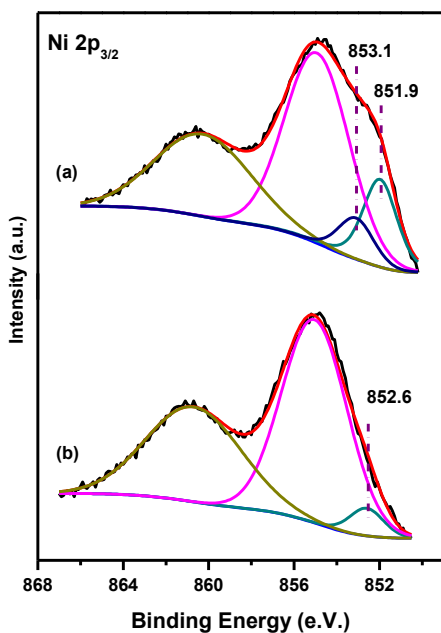

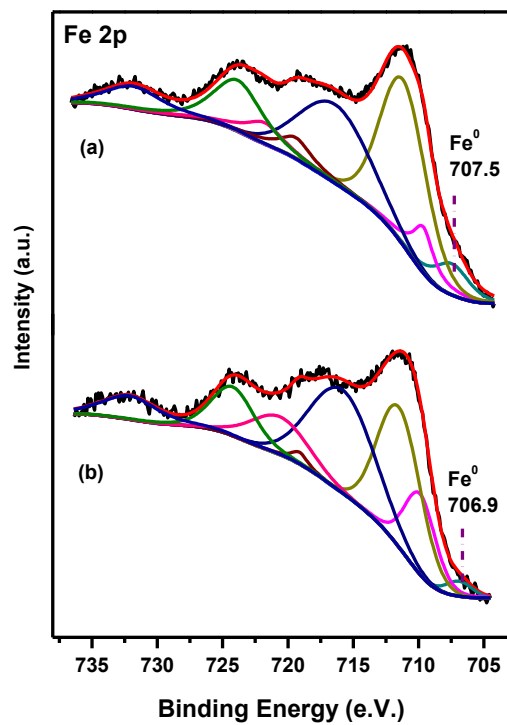Fig. 5.6. Ni $2p_{3/2}$ spectra of Ni_3Fe_1/TiO_2-CeO_2 catalyst, (a) reduced and (b) spent.

Fig. 5.7. Fe 2p spectra of Ni$_3$Fe$_1$/TiO$_2$-CeO$_2$ catalyst, (a) reduced and (b) spent.
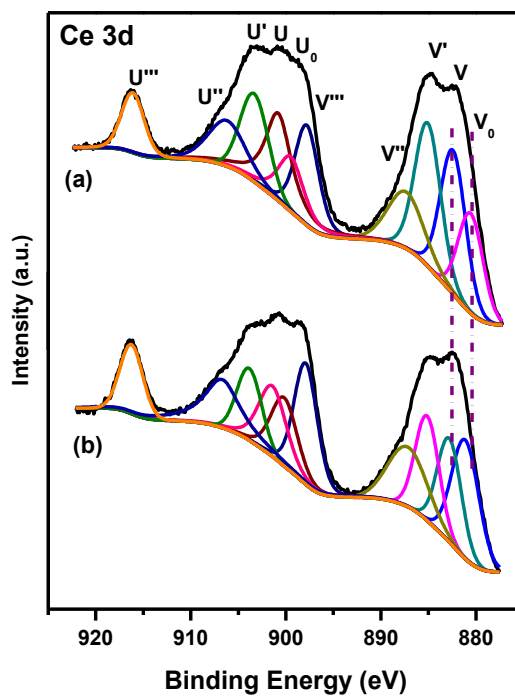
Fig. 5.8. Ce 3d spectra of Ni$_3$Fe$_1$/TiO$_2$-CeO$_2$ catalyst, (a) reduced and (b) spent.
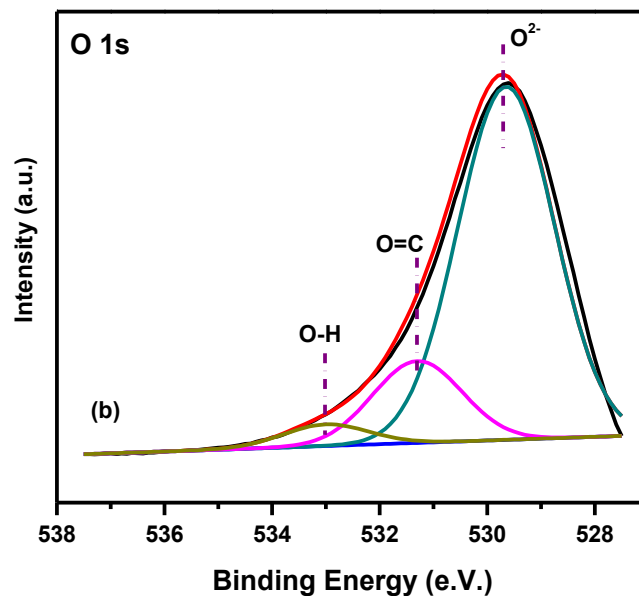
Fig. 5.9. O 1s spectra of Ni_3Fe_1/TiO_2-CeO_2 spent catalyst.

Table 5.2. Surface atomic concentration (%) of different species in reduced and spent Ni_3Fe_1/TiO_2-CeO_2 catalyst

Ni_3Fe_1/TiO_2-	Ni^0		Ni^{2+}	Fe^0	Fe^{2+}	Fe^{3+}	$Ce^{3+}/Ce^{3+}+Ce^{4+}$
CeO_2	(I)	(II)					
Reduced	1.8	0.82	6.61	0.79	0.9	4.86	0.52
Spent	-	0.53	7.28	0.19	1.31	2.9	0.54

XPS analysis of spent Ni_3Fe_1/TiO_2-CeO_2 catalyst was performed to study changes in metal oxidation state, metal-support interaction, and surface concentration after DRM. Deconvolution of Ni $2p_{3/2}$ spectra showed existence of only one type of Ni^0 species at 852.6 eV compared to Ni $2p_{3/2}$ in the reduced catalyst. This behavior suggested changes in electron density of Ni^0 atoms during reforming reaction. While B.E. of Fe^0 $2p_{3/2}$ in spent catalyst was observed at 706.9 eV and exhibited a chemical shift of -0.6 eV compared to its reduced counterparts as presented in Fig. 5.7b. The results affirm dealloying of Ni-Fe alloy during DRM reaction and is consistent with XPS

analysis of Ni-Fe/TiO$_2$ catalysts presented in chapter 4. It is interesting to note that Ce^{3+} 3d$_{5/2}$ in spent catalyst was observed at 881.2 eV, exhibiting a chemical shift of +0.7 eV compared to its reduced counterpart. While Ce^{4+} 3d$_{5/2}$ in the spent catalyst was located at 882.8 eV showing a chemical shift of +0.4 eV. The behavior indicated significant interaction of surface metallic species with the mixed oxide support during DRM. Information on surface adsorbed oxygen species (SAOS) in spent catalysts was obtained by O 1s spectra and is shown in Fig. 5.9. It was revealed that besides lattice oxide O^{2-} peak at 529.7 eV, peaks appeared at 531.2 eV and 533.0 eV. Such peaks are attributed to existence of carbonate and hydroxyl type SAOS in spent catalysts respectively which are also suggested to participate in coke gasification during DRM [27].

The surface concentration of atomic species in reduced and spent catalysts is presented in Table 5.2. As mentioned above, Ni^0 corresponding to 851.9 eV consists 1.8 % while Ni^0 in the form of Ni-Fe alloy located at 853.1 eV comprises 0.82 % surface concentration. Further, Ni^0 concentration in spent catalyst dropped to 0.53%. It is envisaged that Ni^0 (I) in close interaction with CeO$_2$ might have formed Ni-O-Ce solid solution during DRM thereby decreasing Ni^0 concentration. Formation of Ni-O-Ce solid solution is further evidenced by Raman analysis of spent catalysts discussed in section 2.6. While concentration of Fe^0 decreased in the spent catalysts compared to their reduced counterparts. Such findings indicated oxidation of Fe^0 to Fe^{2+}/Fe^{3+} during DRM and agrees with previous reports [8,9]. The relative concentration of Ce^{3+} in the reduced catalyst is evaluated as Ce^{3+}/(Ce^{3+}+Ce^{4+}) due to overlapping of Ce 3d spectra with Ni 2p spectra. It is observed that relative concentration of Ce^{3+} increases from 0.52 to 0.54 after DRM. The phenomenon is related to the consumption of labile oxygen in coke gasification from reducible TiO$_2$-CeO$_2$ support during DRM.

5.2.7 Raman Spectroscopy of TiO₂-CeO₂ support and Ni-Fe/TiO₂-CeO₂ catalyst

Raman spectroscopy of mixed oxide support TiO_2-CeO_2 and Ni_3Fe_1/TiO_2-CeO_2 catalysts is shown in Fig. 5.10. For all the samples, the Raman absorption bands at 396, 513 and 634 cm^{-1} are attributed to E_g, A_{1g} + B_{1g} and B_{1g} vibration mode in TiO_2 [29]. While absorption band at 461 cm^{-1} is assigned to F_{2g} symmetrical vibration mode in CeO_2 [30]. The F_{2g} absorption band corresponds to oxygen atoms surrounding Ce^{4+} ions in the symmetric mode [31]. Nonetheless, peak corresponding to oxygen vacancies in CeO_2 modified samples at 600 cm^{-1} could be observed which coincides with B_{1g} vibration mode of TiO_2 [21]. For calcined Ni_3Fe_1/TiO_2-CeO_2 catalyst, it is observed that peak related to F_{2g} vibrational mode of Ce-O in CeO_2 becomes broader and exhibits a red shift to lower wavenumber at 458 cm^{-1}. Such behavior indicated formation of Ni-O-Ce solid solution [30-32]. However, this F_{2g} peak back shifted to 461 cm^{-1} in the reduced Ni_3Fe_1/TiO_2-CeO_2. The results suggested rearrangement of oxygen atoms surrounding Ce^{4+} ions and thereby dissociation of Ni-O-Ce solid solution upon reduction. Nevertheless, the F_{2g} peak became broader and was shifted to 458 cm^{-1} in the spent catalyst. This phenomenon indicated that strong interaction of Ni species with mixed oxide support formed Ni-O-Ce solid solution, thereby decreasing the population of Ni species on catalyst surface. Overall, introduction of CeO_2 in Ni_3Fe_1/TiO_2 declined the activity due to formation of Ni-O-Ce solid solution.
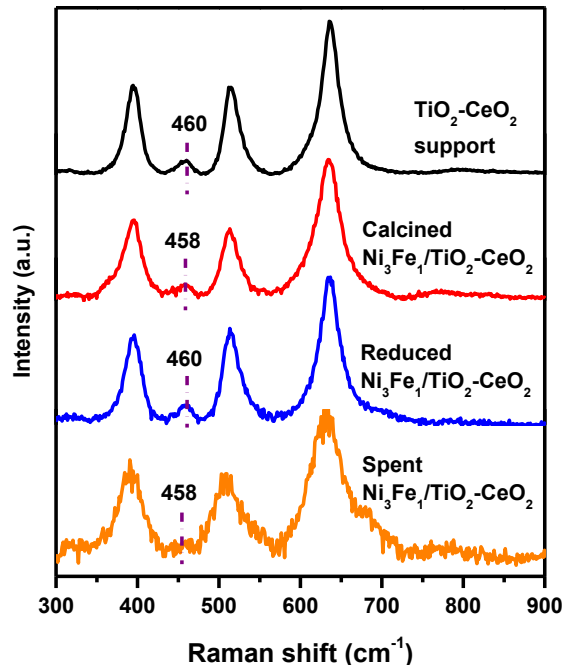
Fig. 5.10. Raman spectra of TiO_2-CeO_2 support, calcined, reduced and spent Ni_3Fe_1/TiO_2-CeO_2 catalyst.

5.2.8 Thermogravimetric analysis-Differential thermogravimetry (DTG)

Thermogravimetric analysis/Differential thermogravimetry (TGA-DTG) of spent catalysts after DRM was performed to gain insights on amount and type of coke deposition. Surprisingly, Ni_3Fe_1/TiO_2-CeO_2 catalyst did not reveal coke deposition during DRM. The results suggested promotional effect of CeO_2 addition to resist carbon formation. It has been reported that during DRM over Ni/TiO_2-CeO_2 catalysts, active and labile oxygen from the reducible support participates in gasification of coke to CO [16]. Secondly, lattice oxygen from FeO_x species also enhanced carbon oxidation during DRM [8,9]. Thus, coke resistance of Ni-Fe/TiO_2-CeO_2 is suggested to dual oxygen resources to promote carbon oxidation. TGA experiment over spent Ni_3Fe_1/TiO_2-CeO_2 catalyst after CH_4 decomposition showed only 9.8 wt% coke deposits compared to 27.2 wt% observed over Ni_3Fe_1/TiO_2. Similar explanation holds for carbon gasification in the

149

presence of reducible TiO_2-CeO_2 supports. DTG analysis of spent Ni_3Fe_1/TiO_2-CeO_2 demonstrated amorphous type of carbon deposition during CH_4 decomposition which is shown to be to be inactive for catalyst deactivation [33]. Thus, addition of CeO_2 is beneficial to resist coke deposition.
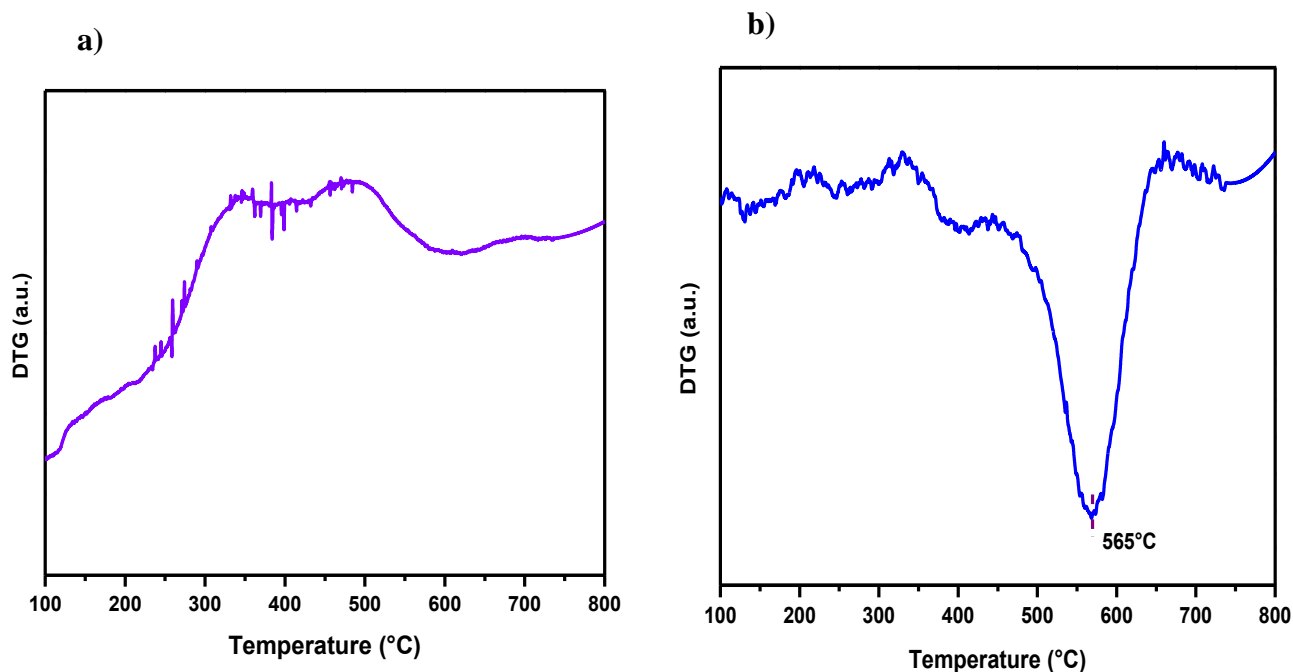
Fig. 5.11. Differential Thermogravimetry (DTG) of used Ni_3Fe_1/TiO_2-CeO_2 catalysts after, a) DRM, b) CH_4 – Decomposition

5.3 References

[1] X. Song, X. Dong, S. Yin, M. Wang, M. Li, H. Wang, Appl. Catal. A 526 (2016) 132-138.

[2] K. Cao, M. Gong, J. Yang, J. Cai, S. Chu, Z. Chen, B. Shan, R. Chen, J. Catal. 373 (2019) 351-360.

[3] Y. Xu, D. Liu, X. Liu, Appl. Catal. A 552 (2018) 168-183.

[4] E. Baktash, P. Littlewood, R. Schomacker, A. Thomas, P.C. Stair, Appl. Catal. B 179 (2015) 122-127.

[5] D. Pakhare, J. J. Spivey, Chem. Soc. Rev. 7 (2014) 7813-7837.

[6] H.O. Seo, Catalysts 8 (2018) 110.

[7] Z. Bian, S. Das, M. H. Wai, P. Hongmanorom, S. Kawi, ChemPhysChem 18 (2017) 3117 – 3134.

[8] S.M. Kim, P.M. Abdala, T. Margossian, D. Hosseini, L. Foppa, A. Armutlulu, W. Van Beek, A. Comas-Vives, C. Copéret, C. Müller, J. Am. Chem. Soc. 139 (2017) 1937–1949.

[9] S.A. Theofanidis, V. V. Galvita, H. Poelman, G.B. Marin, ACS Catal. 5 (2015) 3028–3039.

[10] T. Margossian, K. Larmier, S.M. Kim, F. Krumeich, C. Müller, C. Copéret, ACS Catal. 7 (2017) 6942–6948.

[11] B. Li, Y. Luo, B. Li, X. Yuan, X. Wang, Fuel Process. Technol. 193 (2019) 348-360.

[12] Q. G. Yan, W. Z. Weng, H. L. Wan, H. Toghiani, R. K. Toghiani, C. U. Pittman, Appl. Catal. A 239 (2003) 43–58.

[13] M. Li, A. C. Veen, Appl. Catal. B 237 (2018) 641-648.

[14] K. Takanabe, K. Nagaoka, K. Nariai, K. Aika, J. Catal. 230 (2005) 75-85.

[15] S.S. Kim, S.M. Lee, J.M. Won, H.J. Yang, S.C. Hong, Chem. Eng. J. 280 (2015) 433–440.

[16] C.M. Damaskinos, M.A. Vasiliades, A.M. Efstathiou, Appl. Catal. A 579 (2019) 116-129.

[17] H. Ay, D. Uner, Appl. Catal. B 179 (2015) 128–138.

[18] S. Das, J. Ashok, Z. Bian, N. Dewangan, M. H. Wai, Y. Du, A. Borgna, K. Hidajat, S. Kawi, Appl. Catal. B 230 (2018) 220-236.

[19] S. Damyanova, B. Pawelec, R. Palcheva, Y. Karakirova, M.C.C Sanchez, G. Tyuliev, E. Gaigneaux, J.L.G. Fierro, Appl. Catal. B 225 (2018) 340-353.

[20] A.L.A. Marinho, F.S. Toniolo, F.B. Noronha, F. Epron, D. Duprez, N. Bion, Appl. Catal. B 281 (2021) 119459.

[21] C. Tang, J. Li, X. Yao, J. Sun, Y. Cao, L. Zhang, F. Gao, Y. Deng, L. Dong, Appl. Catal. A 494 (2015) 77-86.

[22] L. Tan, T. Li, J. Zhou, H. Chen, F. Jiang, Colloids Surf. A 558 (2018) 211-218.

[23] S.P. Padi, L. Shelly, E. P. Komarala, D. Schweke, S. Hayun, B.A. Rosen, Catal. Commun. 138 (2020) 105951.

[24] K. Song, M. Lu, S. Xu, C. Chen, Y. Zhan, D. Li, C. Au, L. Jiang, K. Tomishige, Appl. Catal. B 239 (2018) 324–333.

[25] M. Shah, S. Das, A.K. Nayak, P. Mondal, A. Bordoloi, Appl. Catal. A 556 (2018) 137–154.

[26] J. Ashok, S. Kawi, ACS Catal. 4 (2014) 289-301.

[27] M. Zhang, J. Zhang, Z. Zhou, S. Chen, T. Zhang, F. Song, Q. Zhang, N. Tsubaki, Y. Tan, Y. Han, Appl. Catal. B 264 (2020) 118522.

[28] S. Damyanova, I. Shtereva, B. Pawelec, L. Mihaylov, J.L.G. Fierro, Appl. Catal. B 278 (2020) 119335.

[29] X. Zhang, Z. Pei, X. Ning, H. Lu, H. Huang, RSC Adv. 5 (2015) 79192-79199.

[30] P. Zhao, F. Qin, Z. Huang, C. Sun, W. Shen, H. Xu, Chem. Eng. J. 349 (2018) 72-81.

[31] T. V Sagar, D. Padmakar, N. Lingaiah, P.S. Sai Prasad, Catal. Lett. 149 (2019) 2597–2606.

[32] K. Tang, W. Liu, J. Li, J. Guo, J. Zhang, S. Wang, S. Nu, Y. Yang, ACS Appl. Mater. Interfaces 7 (2015) 26839-26849.

[33] A. M. Amin, E. Croiset, W. Epling, Int. J. Hydrogen Energy 36 (2011) 2904-2935.

Chapter 6

Conclusions and Future Work

6.1 Conclusions

In this study, inexpensive Ni-based catalysts were explored for low temperature dry reforming of methane. Usually, monometallic Ni catalysts are prone to deactivation by coke formation during DRM. Thus, Fe is employed as a promoter to Ni catalysts while avoiding the addition of precious metals. The study emphasizes preparation of bimetallic Ni-Fe catalysts over a reducible TiO_2 support by different synthesis approaches. 1st project of the research focused on preparation of Ni-Fe/TiO_2 catalysts by conventional wet impregnation route. Different ratios of Ni/Fe are studied and applied in low temperature DRM, while total nominal metal loading maintained to 10 wt%. 2nd project aimed in achieving better catalytic activity performance in DRM, by employing co-precipitation method for preparation of Ni-Fe/TiO_2 catalysts. The results of 1st and 2nd project showed Ni_3Fe_1/TiO_2 synthesized by co-precipitation method is optimum catalyst. In order to achieve enhanced coke resistance, 20 wt% of TiO_2 was replaced by the addition of reducible CeO_2 in support matrix. The 3rd project discussed the application of Ni-Fe catalyst prepared by co-precipitation procedure supported over a mixed oxide TiO_2-CeO_2. Following paragraphs discuss detailed conclusions from Ni-Fe catalysts.

6.1.1 Ni-Fe/TiO₂ catalysts synthesized by wet impregnation route

Ni–Fe/TiO_2 catalysts synthesized by incipient wetness impregnation method for low temperature DRM lead to the following conclusions: 1) Ni/TiO_2 showed maximum catalytic activity. The increasing of CH_4 consumption during time-on-stream over Ni/TiO_2 was attributed

to CH_4 decomposition as side reaction. Introduction of Fe inhibited catalytic activity. Increasing the amount of Fe from 2.5 wt% to 7.5 wt% dropped H_2/CO ratio and simultaneously increased the carbon balance. Catalytic activity performance results in CH_4 decomposition were in accordance with DRM. Ni/TiO_2 revealed maximum activity while activity dropped significantly over Ni_1Fe_3/TiO_2. However, CO formation during CH_4 decomposition suggested ability of lattice oxygen from TiO_2 or FeO_x to oxidize coke precursors. 2) H_2–TPR suggested increased reducibility of NiO up to 2.5 wt% substitution by Fe. While, addition of Fe did not reveal interaction between Ni and Fe on the surface. CH_4–TPSR results showed that CH_4 activated around 400˚C and that introduction of Fe in Ni/TiO_2 inhibited CH_4 activity. While, DTG results after CH_4-TPSR suggested addition of Fe altered the type of carbon deposited from graphitic to amorphous. CO_2–TPSR/H_2-TPR results showed that addition of Fe promoted activity of CO_2. XPS analysis of reduced catalysts showed metal-support interactions. However, interaction between Ni and Fe were not revealed by XPS analysis, which agreed with H_2-TPR experiments. Besides, metal and support interactions, oxidation state of surface species in the reduced catalysts showed presence of Ni^0/Ni^{2+} and mixture of Fe^{2+}/Fe^{3+}. Metallic Fe was not revealed in $Ni-Fe/TiO_2$ catalysts. The O/Ti ratio was lower than 2, suggested presence of oxygen vacancies in reduced catalysts. CO-chemisorption results showed number of metallic sites decreased significantly upon Fe addition. 3) TGA analysis of used catalysts showed 23.4 wt% coke deposits on Ni/TiO_2 which dropped drastically to 0.1 wt% over Ni_3Fe_1/TiO_2. No carbon deposition was observed over Ni_1Fe_1/TiO_2 and Ni_1Fe_3/TiO_2 catalysts. While XPS analysis of spent catalysts suggested participation of lattice oxygen from TiO_2 support in coke gasification over monometallic Ni/TiO_2. However, lattice oxygen of Fe played dominant role in coke removal over $Ni-Fe/TiO_2$ catalysts. Raman spectroscopy showed presence of graphitic and amorphous carbon after DRM over Ni/TiO_2. On

the other hand, Ni-Fe/TiO$_2$ spent catalysts did not reveal carbon formation. 4) *In-situ* DRIFTS analysis over Ni/TiO$_2$ showed involvement of lattice oxygen from TiO$_2$ support in coke gasification. However, addition of Fe altered the reaction mechanism in which surface hydroxyl species played dominant role to oxidize coke precursors. 5) The optimal catalyst was suggested to be Ni$_3$Fe$_1$/TiO$_2$ that exhibited activity comparable to Ni/TiO$_2$ and showed only 0.1 wt% coke deposits.

6.1.2 Ni-Fe/TiO$_2$ catalysts synthesized by hydrotalcite route

Ni–Fe/TiO$_2$ catalysts synthesized by co-precipitation method studied for low temperature DRM lead to the following conclusions: 1) Ni/TiO$_2$ showed maximum catalytic activity towards CH$_4$ while addition of Fe declined activity performance. While, addition of 2.5 wt% Fe to Ni/TiO$_2$ increased CO$_2$ activity. The H$_2$/CO ratio in Ni/TiO$_2$ increased with time-on-stream which suggested occurrence of CH$_4$ decomposition as side reaction besides DRM. However, Ni$_3$Fe$_1$/TiO$_2$ exhibited consistent H$_2$/CO ratio of 0.8 during DRM, indicating inhibition of CH$_4$ decomposition as side reaction during DRM. Catalytic activity performance results in CH$_4$ decomposition were in accordance with DRM. Ni/TiO$_2$ revealed maximum activity while activity dropped significantly over Ni$_1$Fe$_3$/TiO$_2$. However, CO formation during CH$_4$ decomposition suggested ability of lattice oxygen from TiO$_2$ or FeO$_x$ to oxidize coke precursors. 2) H$_2$-TPR experiments showed presence of bulk NiO and strongly interacting NiO-TiO$_2$ species in monometallic Ni/TiO$_2$. Addition of Fe significantly improved bimetallic Ni-Fe and metal-support interactions. Similarly, reducibility of NiO was promoted in Ni-Fe catalysts. CH$_4$-TPSR results showed CH$_4$ activated around 350°C. Owing to inactivity of Fe towards CH$_4$, transient activity was lowered in Ni-Fe/TiO$_2$ catalysts. DTG results performed after CH$_4$-TPSR showed presence of amorphous carbon only over monometallic and bimetallic Ni-Fe/TiO$_2$ catalysts. CO$_2$-TPSR/H$_2$-TPR experiments indicated that

addition of Fe promoted CO_2 activity. XPS analysis of reduced catalysts showed formation of Ni-Fe alloy and metal-support interactions. Those results were consistent with H_2-TPR analysis. Besides, oxidation state of surface species in reduced catalysts revealed presence of Ni^0/Ni^{2+} and $Fe^0/F^{2+}/Fe^{3+}$. The O/Ti ratio was below 2, indicated presence of oxygen vacancies in the reduced catalysts. CO-chemisorption results revealed reduction in the number of metallic sites upon addition of Fe. 3) TGA/DTG analysis of spent catalysts after DRM showed 31.0 wt% coke deposits over Ni/TiO_2. While addition of only 2.5 wt% Fe (Ni_3Fe_1/TiO_2) significantly dropped coke formation to 0.48 wt%. Ni_1Fe_1/TiO_2 and Ni_1Fe_3/TiO_2 did not reveal coke deposits. Raman spectroscopy of spent catalysts revealed presence of amorphous and graphitic carbon over Ni/TiO_2 and Ni_3Fe_1/TiO_2 after DRM. Raman spectroscopy results concluded that addition of Fe did not alter the type of carbon formed during DRM. XPS analysis of spent catalysts revealed participation of lattice oxygen from TiO_2 support in coke gasification over Ni/TiO_2. However, lattice oxygen from FeO_x species were suggested for coke removal in $Ni-Fe/TiO_2$ catalysts. Secondly, Ni-Fe alloy was dealloyed and Fe^0 was oxidized to Fe^{2+}/Fe^{3+} in the spent catalysts. 4) *In-situ* DRIFTS analysis concluded that coke precursors were oxidized by lattice oxygen of support in Ni/TiO_2. Addition of Fe favored the formation of carbonate species as intermediates which were shown to react with coke precursors. 5) Ni_3Fe_1/TiO_2 was suggested to be optimal catalyst which showed comparable activity to monometallic Ni/TiO_2 and decreased coke deposits to 0.48 wt% only.

When comparing the results of catalysts synthesized by co-precipitation method with catalysts synthesized by impregnation route, it was concluded that catalysts prepared by co-precipitation method showed better metal reducibility, metal-support, and bimetallic interactions. Overall influence of catalyst preparation approach was reflected by higher catalytic activity in catalysts synthesized by co-precipitation method. Besides, the role of Fe was attributed to oxidize coke

precursors during DRM thereby achieving enhanced coke resistance. In the view of achieving complete removal of coke deposition, CeO_2 was employed along with TiO_2 in the support matrix due to its oxygen storage capacity. Therefore, we explored the effect of CeO_2 addition over Ni_3Fe_1/TiO_2 catalyst synthesized by co-precipitation method.

6.1.3 Ni-Fe/TiO₂-CeO₂ catalyst synthesized by hydrotalcite route

Ni_3Fe_1/TiO_2-CeO_2 catalyst lead to following conclusions: 1) The catalytic activity decreased of Ni_3Fe_1/TiO_2-CeO_2 decreased compared to Ni_3Fe_1/TiO_2 catalysts prepared by co-precipitation route. The cause of decreased catalytic activity was suggested to the attenuation of Ni^0 sites due to SMSI effect. This phenomenon ultimately led to the formation of Ni-O-Ce solid solution during DRM. While Ni^0 was also shown to oxidize under DRM conditions thereby contributing to activity loss. Activity performance in CH_4 decomposition showed CO formation which suggested lattice oxygen from FeO_x and mixed oxide support played important role to oxidize coke precursors. 2) H_2-TPR experiments showed SMSI effect and enhanced reducibility upon modification of TiO_2 with CeO_2 in Ni_3Fe_1/TiO_2-CeO_2. CO-chemisorption experiment showed increase in number of metallic sites over Ni_3Fe_1/TiO_2-CeO_2 compared to Ni_3Fe_1/TiO_2. The results concluded promotional effect of CeO_2 to enhance metal reducibility. The results of CH_4-TPSR and CO_2-TPSR over Ni_3Fe_1/TiO_2-CeO_2 catalyst were similar to Ni_3Fe_1/TiO_2 which suggested that surface reaction of CH_4 and CO_2 with catalyst is independent of support modification. XPS analysis of reduced Ni_3Fe_1/TiO_2-CeO_2 catalyst showed formation of Ni-Fe alloy and metal-support interactions. While presence of Ce^{3+} besides Ti^{3+} species confirmed enhancement in the formation of oxygen vacancies. 3) TGA-DTG analysis of spent catalyst after DRM showed no coke deposition over Ni_3Fe_1/TiO_2-CeO_2. The results concluded that addition of CeO_2 promotes coke inhibition. Lattice oxygen from FeO_x and mixed oxide support are suggested as oxygen resources

for coke gasification. XPS analysis of spent Ni_3Fe_1/TiO_2-CeO_2 catalyst showed dealloying of Ni-Fe alloy and participation of CeO_2 in DRM. While Ni^0 was oxidized to N^{i2+}. Raman spectroscopy of spent catalyst showed formation of Ni-O-Ce solid solution. The results concluded attenuation of Ni^0 sites during DRM due to SMSI effect.

Thus, Ni_3Fe_1/TiO_2 catalyst prepared by co-precipitation method was proven to be optimum catalyst in this project which showed pronounced catalytic activity and minimal coke formation.

6.2 Future Work

The future work for dry reforming of methane should be focused on investigating the optimal Ni_3Fe_1/TiO_2 co-precipitation catalyst. Thermodynamically, equilibrium conversion of CH_4/CO_2 and high yield of syngas are achieved at 850˚C. Therefore, DRM should be tested at 850˚C to study Ni_3Fe_1/TiO_2 co-precipitation catalyst.

Besides, the reduction temperature employed to activate the catalyst should be elevated which would mainly serve two purposes: 1) Reduction of unreduced NiO and FeO_x species thereby generating active metallic sites for reforming. 2) Formation of Ni^0 upon reduction would favor hydrogen spill-over phenomenon which would promote the reduction of TiO_2 support. This process would generate more oxygen vacancies and ultimately enhance coke resistance of catalyst.

Addition of Co to Ni_3Fe_1/TiO_2 is suggested in which different ratios between Co and Ni_3-Fe_1 could be tuned to obtain optimal DRM performance. Addition of Co would serve two purposes: 1) provide active Co^0 sites for DRM besides Ni^0 2) Oxidation of carbon precursors would be significantly enhanced owing to oxophilicity of Co, thereby enhancing coke resistance of catalyst.

Appendix 1

Physical properties of reduced catalysts synthesized by wet impregnation

Catalyst	BET area (m^2/g)	Metal surface area (m^2/g)	Pore size (nm)	Pore volume (cc/g)
Ni/TiO_2	57.71	5.12	27.00	0.39
Ni_3Fe_1/TiO_2	51.50	4.58	24.26	0.31
Ni_1Fe_1/TiO_2	52.10	4.62	26.77	0.35
Ni_1Fe_3/TiO_2	50.83	4.51	26.74	0.34

Physical properties of reduced catalysts synthesized by co-precipitation

Catalyst	BET Area (m^2/g)	Metal surface area (m^2/g)	Pore size (nm)	Pore volume (cc/g)
Ni/TiO_2	59.04	4.74	33.84	0.49
Ni_3Fe_1/TiO_2	44.24	3.95	34.49	0.38
Ni_1Fe_1/TiO_2	41.96	3.72	30.08	0.31
Ni_1Fe_3/TiO_2	48.28	4.28	35.29	0.42
$Ni_3Fe_1/TiO_2\text{-}CeO_2$	55.22	4.89	22.09	0.31